Geological Survey of Israel
Ministry of Energy

The spatial and temporal development of the Bet Kerem Fault System, Northern Israel

Rawi Dawood

Report GSI/05/2023

April 2023

32 Yeshayahu Leibowitz St. Jerusalem 9692100, Israel

Cover pictures:

Zurim Escarpment, looking Northeast.

Back pictures:

^{36}Cl sampling of the Deir Al-Assad fault scarp.

Pictures were taken by Shalev Siman-Tov.

Geological Survey of Israel
Ministry of Energy

The spatial and temporal development of the Bet Kerem Fault System, Northern Israel

Rawi Dawood

Thesis submitted in partial fulfillment of the requirements for the Master of Sciences degree Department of Geology, Institute of Earth Sciences, Faculty of Mathematics and Natural Sciences, the Hebrew University of Jerusalem.

The study was carried out under the supervision of:

Prof. Ari Matmon, the Hebrew University of Jerusalem.

Dr. Shalev Siman-Tov, Geological Survey of Israel.

Report GSI/05/2023 April 2023

Abstract

Fault interaction is a common phenomenon in normal fault systems, in which short fault segments link to form a continuous long fault. A result of such linkage is an increase in slip rate, which affects the landscape. Furthermore, it has an impact on the seismic behavior of the segments. Here, I investigate the Bet-Kerem fault system, northern Israel, which provides an exceptional opportunity to understand the interplay between fault segment linkage and landscape evolution. Moreover, it also provides the opportunity to understand the seismic behavior of fault segments within a linked fault system.

The absolute stratigraphic and topographic throws and the difference between them (S-T value) were estimated for six segments of the Bet Kerem fault system. S-T values as well as stratigraphic and topographic throws are highest at the Sajur segment, located in the center of the system and they gradually decrease along the western segments. In the Bet Kerem fault system, it appears that all segments were formed simultaneously. However, the segments located at the center of the system linked first, their slip rate increased, causing escarpment initiation along them. With time the linkage of the segments propagated westward, increasing throw rates, and forming young escarpments to the west.

Using the cosmogonic ^{36}Cl dating method, I sampled and recovered the seismic exhumation history of two fault scarps, the Sajur and Deir Al-Assad segments. I also remodel the seismic history of the Nahf-East segment which was originally investigated roughly 20 years ago. ^{36}Cl results revealed that the three dated segments were active simultaneously during five distinct periods. The earlier period of activity (30.0-28.0 ky), the second (25.0 -24.0 ky), third (12 – 11), fourth (8.5 – 7.0), and the last period (5.0 – 4.0 ky). In each activity period at least 1.2 m of surface slip has occurred. This temporal framework of events indicates that during each activity period a cluster of at least two large earthquakes (Mw > 6) occurred, that caused in rupture of the three dated segments. Consequently, the Bet Kerem fault system seismically behaves like a single continuous fault.

Acknowledgments:

Whilst this thesis only has my name on the front, this work could not have been completed without the help and support of many others, who I will try and thank here. Sorry for any omissions!

My main supervisors are Prof. Ari Matmon and Dr. Shalu Siman-Tov. No one could ask for better supervisors. They always had time to chat and hear my latest problem. They understand when I made mistakes in the lab, are enthusiastic about my ideas, and have a well of optimism when it looked like I'd never finish this thesis.

I would like to thank Prof. Amotz Agnon, Prof. Einat Aharonov, Dr. Ezra Zilberman, Dr. Oded Katz, Prof. Ron Sha'ar, Dr. Uri Ryb, and Prof. Ze'ev Reches for fruitful discussions, inspiring ideas, and critical reviews.

I am grateful to the Academic members of the Institute of Earth Science who were there when I needed some advice. Among whom I would like to specially thank Prof. Ronit Kessel and Prof. Yehouda Enzel.

Many thanks to Ofir Tirosh for the ICP measurements and to Yona Geller and Dr.Yael Ebert for helping me with the sample preparation and analysis; and for the help of the ASTER team from the AMS facility at Cerege, France.

I am grateful to the administrative members of the Institute of Earth Science and Geological Survey of Israel. Among whom I would like to specially thank Bat Sheva Cohen, Galia Shneor, Helena Kirmayer, Magi Perken, and Yosi Sherer.

I'd like to thank my friends from the Institute of Earth Science who helped me in the field, in computer modeling, with long and fruitful discussions, encouragement, and friendship: Adar Glazer, Dalal Saed, Eldar Buzaglo, Ilya Kutuzov, Koko Armon, Noam Gazit, Naomi Moshe,
Shai King, and Yuval Shmilovitz.

Where would I be without my incredible family and friends? My sincere thanks go out to each of you for your incredible support during this time.

In a summary, I would say It's been quite a wild ride at times, and a good adventure, but being surrounded by nice people made it really fun.

This study was funded by The Israel Science Foundation grant #2470/21, The national steering committee for earthquake preparedness, and Scholarship for Arab students studying for a master's degree in science, the Faculty of Natural Sciences, The Hebrew University, of Jerusalem.

Table of Contents

1. Introduction

1.1. Earthquakes and surface rupturing

Destructive earthquakes have been and still are one of the most significant natural hazards for humanity (Ambraseys, 2015). One way to reduce their damage is to define the extent of seismically active regions. Regions along plate boundaries are characterized by high seismic activity (Migowski et al., 2004; Usami et al., 2018) i.e., seismically active regions. In contrast, inner regions that are located far away from plate boundaries are usually less active but may still experience destructive earthquakes (Benedetti et al., 2002). These intraplate earthquakes usually occur in fault systems. Which are series of short fault segments that maybe connected below the surface to form a long continuous fault. Consequently, earthquakes that occur in such systems can rupture multiple fault segments, resulting in earthquakes of greater magnitude, surface rupture slip amount, and length than if only one segment ruptured (Bruhn et al., 1987; Puliti et al., 2020; Soliva et al., 2008; Suter, 2015; Wells & Coppersmith, 1994). Therefore, determining whether the segments are linked at depth, in addition to paleoseismological data such as surface slip amount generated by past earthquakes and their recurrence interval is required in order to assess the seismic hazard that pose by such systems.

Several methods are used when assessing the recurrence interval and maximum magnitude of earthquakes that generated surface rupture and/or significant damage during the late Pleistocene - Holocene. These include written historical records (e.g., Guidobon & Stucchi, 1993; Zohar et al., 2017), analyses of damage to historical and archaeological sites (e.g., Marco, 2008) and investigations of seismic trenches (e.g., Reches & Hoexter, 1981; Rockwell & Ben-Zion, 2007; Amit et al., 2002). In mountainous terrains composed of carbonate rocks, surface rupture is manifested by carbonate bedrock fault scarps. By applying the cosmogenic isotopes exposure age method, one can reconstruct the exhumation history of a fault scarp and by that the recurrence interval and the maximum magnitude of earthquakes ruptured the Earth's surface (e.g., Benedetti et al., 2002; Mitchell et al., 2001; Schlagenhauf et al., 2010; Zreda & Noller, 1998; Benedetti et al., 2013; Mozafari et al., 2021). Paleoseismological data from many normal fault systems, commonly show relatively large surface slip amounts on short fault segments (Benedetti et al., 2002, 2013; Mitchell et al., 2001; Schlagenhauf et al.,

2011). These large amounts are not compatible with the surface slip/fault length ratio (e.g., Wells & Coppersmith, 1994). Such a disagreement should always raise the possibility that an investigated segment was part of a linked fault array.

1.2. Normal faults interaction

One way common to determine whether fault segments are linked is by using fault throw profiles, as well as fault trace maps. A single, isolated normal fault segment that grows with no interaction or disturbance from other fault segments, will grow in displacement and length by small increments, each correlated to a fault-slip (earthquake) event. The displacement profile of this isolated fault segment will be symmetric with a maximum value at its center and a zero value at its tips (Figure 1) (Cowie & Roberts, 2001; Cowie & Scholz, 1992b; I. Manighetti et al., 2001; Scholz, 2019). The isolated fault segment will grow until it starts interacting with the other fault segments to form one long continuous fault (Cowie, 1998; Cowie et al., 2006; Cowie & Scholz, 1992a; McLeod et al., 2000; Roberts & Michetti, 2004; Rotevatn et al., 2019; Taylor et al., 2004). It is well accepted that normal fault linkage starts as a soft-linkage, by which fault motion bends the rocks to form a relay ramp. With increasing deformation, the ramp may be breached. As a result, the two faults that overlap and formed the relay ramp are physically connected and form one continuous fault. At that time the connected segments become hard-linkage faults. As result, the throw profile of the two faults will change from symmetric throw profile (similar to that of an isolated fault) to asymmetric throw profile with maximum displacement located at the fault tip that is closest to the fault system center (Cowie & Roberts, 2001; I. Manighetti et al., 2001; Nicol et al., 1996; Peacock & Sanderson, 1991; Rotevatn et al., 2019; Walsh et al., 2003). Faults linkage also affects segment displacement rates, in which fault displacement rates are increased once the faults start to link. The slip rate increases as the length of the linked array increased, and the location of the fault within the array. Faults that are located at the center of the array will have the maximum slip rate, which will gradually decrease towards the array tips. (Cowie, 1998; Cowie & Roberts, 2001; McLeod et al., 2000; Roberts & Michetti, 2004) (Fig. 1). An explanation of why faults increases the slip rate once they are linked is provided by the linear empirical scaling relation, $D_{max} = \gamma * L$, between the fault length (L) and the fault maximum displacement (D_{max}) (Cowie & Scholz, 1992b; Scholz, 2019). Isolated normal faults typically show an average ratio of $\gamma = 0.03$ (Schlische et al., 1996; Scholz, 2019). The case of segment

linkage is somewhat complicated. During the initial stages of fault linkage, the displacement amounts were too small relative to the post-linkage length (small γ value). As a result, slip rates increase to achieve the typical γ value. Faults that are located at the center of the array will have the highest slip rate which will gradually decrease towards the array tips, by that acquiring eventually an overall symmetric throw profile, similar to that of an isolated fault (Fig .1) (Cowie et al., 2000; Cowie & Roberts, 2001; Roberts & Michetti, 2004; Rotevatn et al., 2019).

1.3. Normal fault slip rate and escapement

Fault slip rate and denudation rate are the two main factors that dictate the fault topographic throw as well as the exposed stratigraphic sequences on both sides of the fault (Matmon et al., 2000b, 2003). High slip rates accompanied by relatively slow denudation enable the formation of high escarpments and exposure of the same stratigraphic at both sides of the fault. Therefore, these faults commonly show topographic throw equal to the stratigraphic throw (Fig. 2) (Medina-Cascales et al., 2021; Strak et al., 2011). While normal faults with very low slip rates compared to the denudation-rate will show no topographic expression, because every slip event is removed by erosion. As a result, young stratigraphic units are preserved on the hanging wall and older stratigraphic units are exposed on the footwall. i.e., only stratigraphic throw is accumulated along these faults (Fig. 2) (Matmon et al., 2000b). Fault slip rate can also be changed over time, for example, the fault slip rate at the beginning, is lower than the denudation rate, with time the fault starts to interact with the other faults, and due to that, the fault slip rate increases to be higher than the denudation rate. In this case, the fault stratigraphic throw will be much larger than the topographic throw, which probably was the case in the Galilee, and especially in the Bet Kerem fault system (Fig. 2) (Matmon et al., 2000a, 2000b).

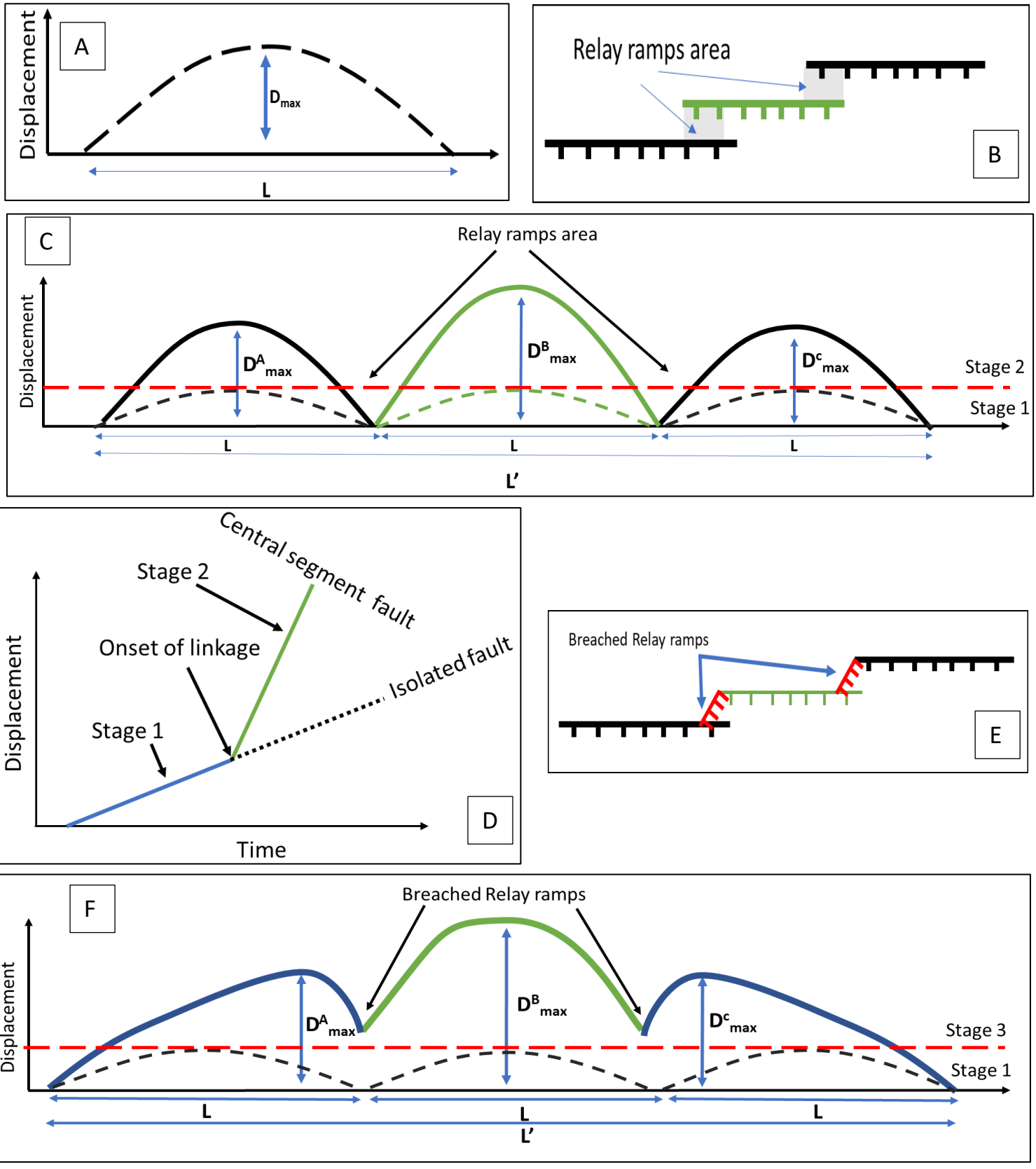

Figure 1. A conceptual model of normal fault growth and linkage (modified after Cowie and Roberts, 2001). (A) Qualitative diagram illustrating the displacement distribution of an isolated fault segment with length L, and maximum displacement D_{max}. (B) Map view of three normal faults dipping to the same direction and overlap to form two relay ramps, i.e., connected by soft linkage. (C) Displacement profiles of the faults illustrated in panel B prior (dashed lines, stage 1) and after the soft linkage (solid lines, stage 2). Note, that the central fault has the largest displacement (D) Qualitative graph of the displacement as function of time for the central fault during the first (blue) and second (green) stages of faulting. As the soft linkage initiates, the fault slip rate increases. (E) Map view of the three normal faults after breaching (breaching segments marked in red), i.e., connected by hard linkage (stage 3). (F) Displacement profile of the faults in map E. The fault displacement profiles are symmetric by the end of stage 1 (dashed) compare to those of stage 3 (green for the central fault and blue for the edge faults). Note, that while the central fault has a symmetric displacement profile, the side faults have asymmetric profiles, and that the overall profile approached a symmetric shape.

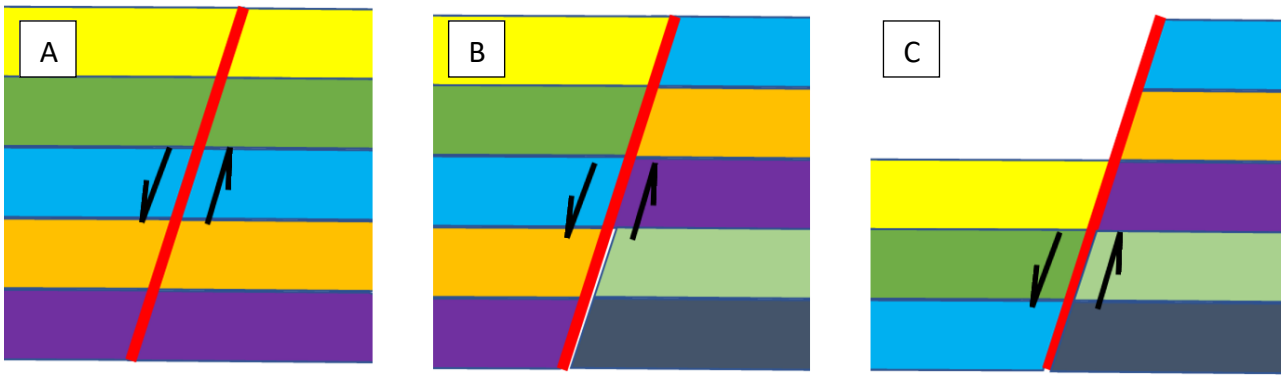

Figure 2. A cartoon illustrating the possible evolution of stratigraphic and topographic throws in the study area. (A) The initiation of faulting. A normal fault cuts through horizontal layers, from the lower, old unit (purple) to the top, youngest unit (yellow). (B) Faulting during the first stage, no topographic expression. This situation occurs when the rate of vertical displacement is lower or equal to the rate of denudation. This enables ongoing truncation of the uplifted block while preserving the young sequence on the downside block. (C) Stage two: fault slip rate increases and becomes faster than the denudation rate, causing the formation of an escarpment and exposed its stratigraphic sequence. The fault plane and its sense of slip are marked by red line and black arrows, respectively. Colored layers indicate the stratigraphic sequence (modified after Matmon et al., 2000).

1.4. Study area

The Galilee, Northern Israel, is a carbonate terrain (fig .3) (Bachmann & Hirsch, 2006; Sneh et al., 1998), where landscape evolution is controlled by erosion and tectonic activity (Matmon et al., 2000b, 2003). Since the middle Miocene, the Galilee has been undergoing N-S extension, accommodating strain by the rotation of conjugate systems of strike-slip faults and later by generally E-W trending normal faults (Freund, 1970; Matmon et al., 2003; Mitchell et al., 2001; Ron & Eyal, 1985). Since the early Pliocene, normal faulting started to be dominant in Galilee, and by that, the key role of Galilee landscape evolution, especially for the basin and range landscape in the lower Galilee (fig .3) (Freund, 1970; Matmon et al., 2003; Ron & Eyal, 1985).

The Bet-Kerem valley, the northernmost valley of the Lower Galilee, is bounded in the north by the Zurim Escarpment, which is about 30 km long and rises ~700 m above the valley (fig. 3 and 4). At the base of the Zurim Escarpment there are several, relatively short (3-7 km), normal fault segments, generally trending E-W and named here together “the Bet-Kerem fault system”. The eastern tip of the fault system is located at the Korazim Plateau, in close proximity to the Jordan rift valley. The western tip reaches the continental shelf in the Mediterranean Sea (fig. 3). At about the center of the Bet-Kerem fault system, the NNW – SSE

trending Peqi'in fault, divides the Zurim Escarpment into two major parts that differ by their exposed stratigraphic sequence and morphology. The Peqi'in fault originally formed as a strike-slip fault and was reactivated as a dip-slip fault during the second, normal faulting phase. As a result, the top of Zurim escarpment along the downfaulted block west to the Peqi'in fault, is composed of hard limestone and dolomites of the Cenomanian to Turonian ages. East of the Peqi'in fault, the escarpment is composed of Aptian to Cenomanian limestone, dolomite, and significant exposure of marl layers. Due to the exposure of marl in eastern steep slopes, the eastern part is subjected to repeated landslides. These landslides prevent the determination of geological structures and exposed stratigraphy (fig. 4) (Freund, 1959; Golani, 1961; Siman-Tov et al., 2019). Therefore, this study focuses only on the western of the fault system.

The Bet-Kerem valley (west to Peqi'in fault) is mostly underlain by chalk and marl of Senonian age. In contrast, the Senonian sequence is eroded from the top of the Zurim Escarpment. This situation indicates that the slip rate history at the Bet Kerem fault system consists of two main phases. In the first phase, the slip rate was not faster than the rate of denudation. Thus, relief did not exist, and only stratigraphic accumulated. While during the second phase, the slip rate increased and became faster than the denudation rate. This significantly decreased the denudation rate along the uplifted block and enabled the formation of the present relief (Matmon et al., 1999, 2000a, 2000b, 2003, 2008). Slope shape analysis of the Zurim escarpment, and analysis of the drainage systems that flow on the top of the Zurim escarpment, indicates that the escarpment initiation age decreases (gets younger) toward the west from the center of the Bet Kerem Fault system (Matmon et al., 1999, 2000b, 2008). i.e., fault segments located close to the center increased their rate first and over time it increased westward.

Fault segments located close to the Bet Kerem fault system center, display fault scarps, some of which reach 12 meters in height (fig.4, 12) (Matmon et al., 2000b; Mitchell et al., 2001; Siman-Tov et al., 2019). One of these fault scarps, the Nahef east fault (fig. 4), was investigated by Mitchell et al. (2001). In-Situ cosmogenic ^{36}Cl exposure dating was used to obtain the timing of major displacement caused by earthquakes that ruptured the surface along the Nahef east fault. Mitchell et al., (2001) found three distinct periods of intense fault activity with over 6 meters of displacement occurring over 3 ka during the middle Holocene. Smaller amounts (~1.5 m) of displacement occurred during the late Pleistocene (~12ka) and

late Holocene (~1.5ka). These large amounts of surface rupturing are not compatible with the displacement/length ratio (e.g., Wells & Coppersmith, 1994). There is therefore a possibility that the Nahf East segment is part of a linked fault array.

In order to determine whether fault linkage is responsible for the change in segment slip rates along the Zurim Escarpment and the large surface slip amount observed at the Nahf East segment. First, it is critical to determine whether the Bet Kerem fault segments are linked. Therefore, I reconstructed throw profiles of the investigated segments. The analysis of these profiles allowed for the determination of whether segments are linked, what type of link exists between segments, when they occur, and by that how it affects the escarpment initiation age. Second, I used the cosmogenic ^{36}Cl exposure dating method and recovered the last ~ 30 ka exhumation history of other two fault scarps adjacent to the Nahf East segment, the Sajur and the Deir Al-Assad segments, and remodel the Nahf east fault data (fig. 4). Combining this Data with the fault segments linkage data provides a solution to the disagreement between the large rupture amount observed at the relatively short Nahf East segment by Mitchell et al., (2001). Moreover, gain a better understanding of the earthquake behavior within the Bet-Kerem fault system as an example of a linked normal fault system. As a final step, I used all of these data and determine the seismic hazard posed by the Beit-Kerem fault.

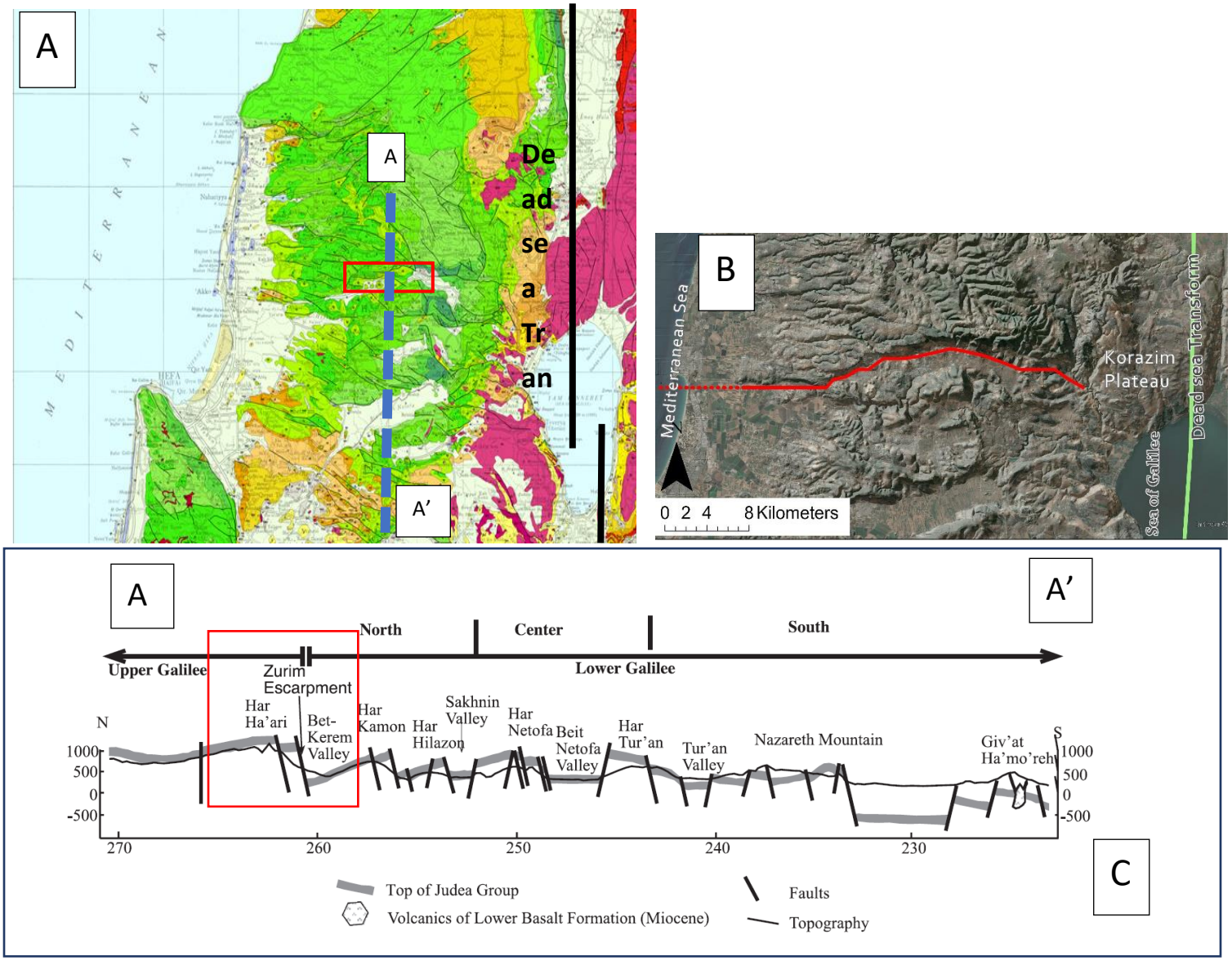

Figure 3. (A) Geological map of the Galilee. Green areas mark Cretaceous carbonate rocks. The red box outlines the location of the study area (fig. 4) (Modified from Sneh et al., (1998)). (B) The general trend of the Bet Kerem fault system (red line) on shaded relief map of the Galilee (Hall, 1993). (C) The shallow structure of the Galilee. The northern part of the Lower Galilee is composed of blocks tilted to the north while the southern blocks dipping south. The central part is dominated by horsts and grabens. The red box outlines the location of the Bet-Kerem Valley (Modified after Matmon et al., (2003)).

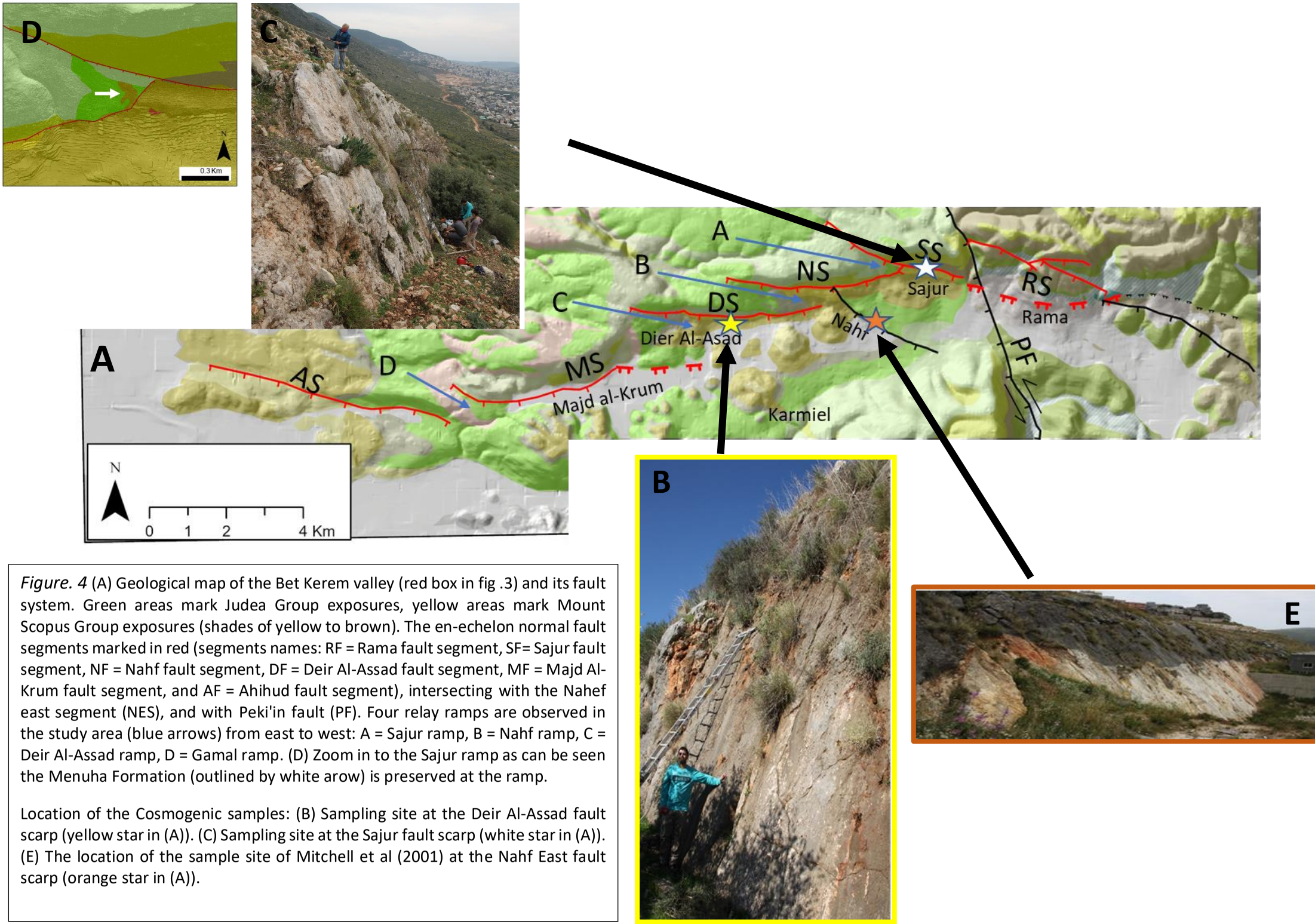

Figure. 4 (A) Geological map of the Bet Kerem valley (red box in fig .3) and its fault system. Green areas mark Judea Group exposures, yellow areas mark Mount Scopus Group exposures (shades of yellow to brown). The en-echelon normal fault segments marked in red (segments names: RF = Rama fault segment, SF= Sajur fault segment, NF = Nahf fault segment, DF = Deir Al-Assad fault segment, MF = Majd Al-Krum fault segment, and AF = Ahihud fault segment), intersecting with the Nahef east segment (NES), and with Peki'in fault (PF). Four relay ramps are observed in the study area (blue arrows) from east to west: A = Sajur ramp, B = Nahf ramp, C = Deir Al-Assad ramp, D = Gamal ramp. (D) Zoom in to the Sajur ramp as can be seen the Menuha Formation (outlined by white arow) is preserved at the ramp.

Location of the Cosmogenic samples: (B) Sampling site at the Deir Al-Assad fault scarp (yellow star in (A)). (C) Sampling site at the Sajur fault scarp (white star in (A)). (E) The location of the sample site of Mitchell et al (2001) at the Nahf East fault scarp (orange star in (A)).

1.5. cosmogenic isotope exposure age dating

Rocks exposed at the Earth's surface interact with secondary cosmic rays to produce in-situ terrestrial cosmogenic nuclides (TCN) such as ^{36}Cl, ^{10}Be and ^{26}Al (Gosse & Phillips, 2001). The probability of TCN production depends on the abundance of target nuclides and on the energy spectrum and type of the particles that collide with the targets (Gosse & Phillips, 2001; J. Stone et al., 1994). In this study, I will date the exposure history of carbonate bedrock fault scarps using the TCN ^{36}Cl, which is produced in calcium-rich rocks. However, minor amounts of ^{39}K, Ti, and Fe can also serve as targets for ^{36}Cl production (Gosse & Phillips, 2001; Stone et al., 1996). ^{36}Cl is produced through several pathways:

[1] Spallation reactions: these reactions occur when high-energy secondary neutrons collide with the target nuclei and spall them into nuclides with smaller atomic masses. The high energetic neutrons react strongly with matter, and as a result, this neutron flux decreases exponentially and rapidly with depth (Fig .5) (Eq. 1) and is most efficient in the upper two meters of the surface:

$$(1)\quad P_{t,f}(z) = P_{0,f} * e^{-\left(z*\frac{\rho}{\Lambda_f}\right)}$$

where $P_{t,f}(z)$ is the production rate by spallation at depth z, $P_{0,f}$ the production at the earth surface, ρ the rock density, Λ_f the attenuation length for fast neutron (160 g*cm^{-2}) (Bierman, 1994; Schimmelpfennig et al., 2009).

[2] Slow negative muons: muons are unstable energetic lepton particles with a very short lifetime (~10^{-6} s). The interactions between muons and atoms are weak (attenuation length of muons is 1500 g*cm^{-2}). Thus, muons penetrate to a greater depth of matter than the high energy neutrons (i.e., in a great depth under the earth's surface (>4 m) they are the main source of cosmogenic isotope production). In the case of ^{36}Cl, slow negative muons can be captured by ^{40}Ca and ^{39}K atoms resulting in the production of ^{36}Cl cosmogenic nuclide (Gosse & Phillips, 2001; Stone et al., 1998) (fig. 5)(Eq. 2):

$$(2)\quad P_{t,m}(z) = P_{0m} * e^{-\left(z*\frac{\rho}{\Lambda_m}\right)}$$

where $P_{t,m}(z)$ is the production at depth z by muons, P_{0m} the production at the earth surface, ρ the rock density, Λ_m the attenuation length of muons (1500 g*cm^{-2}) (Bierman, 1994; Schimmelpfennig et al., 2009).

[3] Low-energy thermal and epithermal neutrons (slow neutrons): Low-energy thermal and epithermal neutrons are formed when high-energy secondary cosmic-ray neutrons collide repeatedly with atoms in the atmosphere and rock, and consequently loose energy. These neutrons can then be captured by the target nuclei such as ^{35}Cl to form cosmogenic ^{36}Cl. The production profile of the thermal and epithermal neutrons increases with depth to about 15-30 cm under the surface (depending on density) and then decrease exponentially to ~0 at about two meters under the surface (fig. 5). In addition to the cosmogenic reactions described here, ^{36}Cl can also be radiogenically produced when ^{35}Cl captures some of the low-energy neutrons generated by radiogenic decay of U and Th or by fission of ^{238}U (Bierman, 1994; Gosse & Phillips, 2001) .

Overall, the total production of the ^{36}Cl at sea level and high geographic latitude (> 60^{o}) is the sum of all production pathways (Eq. 3.) It has a nearly exponential depth profile with a peak at ~15 cm which is dependent on the Cl concentration in the rock. Near the earth surface the Spallation reaction is the main source for ^{36}Cl production while at depths greater than >2m, the slow negative muons are the main source for ^{36}Cl production (fig .5).

$$(3)\quad P_t(z) = P_f(z) + P_m(z) + B(z)$$

where $P_f(z)$ is the production rate by fast neutron spallation (Eq. 1), $P_m(z)$ the production rate by muons (Eq. 2), and B(z) the production rate by slow neutrons, at depth z (Bierman, 1994; Schimmelpfennig et al., 2009).

The total production of the ^{36}Cl depends not only on depth, but also as a function of:

1) Geographic and topographic setting (latitude, longitude, elevation, depth of sample, topographic shielding) (Eq. 4) (Gosse & Phillips, 2001; Schimmelpfennig et al., 2009).

2) Chemistry of the exposed rock, which determines the target atoms and the competing atoms over slow neutron absorption (Eq. 4) (Gosse & Phillips, 2001; Schimmelpfennig et al., 2009):

$$(4)\quad P_t(z) = S_{el,s}F_sP_s(z) + S_{el,\mu}F_\mu P_\mu(z) + S_{el,s}F_n[P_{eth}(z) + P_{th}(z)] + P_{rad}$$

Where: $P_t(z)$ is the total production rate s = spallation, μ = capture of slow negative muons, eth = epithermal neutron capture, th = thermal neutron capture, and rad for radiogenic production. $S_{el,s}$ and $S_{el,\mu}$ are scaling factors to account for the effects of latitude and elevation for spallation and muons , F is a scaling factor to sum shielding corrections for the geometry, topography and cover shielding. Pi is the sample specific ^{36}Cl production rate at given depth. Equation from Schlagenhauf et al. (2010), Schimmelpfennig et al. (2009) and Gosse and Phillips (2001).

The ^{36}Cl is a radioactive, unstable element, which decays to ^{36}S and ^{36}Ar with a half-life of $3*10^5$ yr (Bartholomew et al., 1955). Therefore, the overall measured concentration of ^{36}Cl (in the absence of denudation), is the product of both production and decay, and it will increase until steady state is reached. The number of ^{36}Cl atoms per gram rock is described by eq (5).

$$(5) \quad N(t,z) = \frac{P_t(z)}{\lambda}(1 - e^{-\lambda t})$$

where $N(t,z)$ is the number of atoms per gram after time t from the exposure to cosmic ray, $P_t(z)$ the production rate at z (eq (4)), λ the decay constant of ^{36}Cl (Bierman, 1994).

Reorganizing Eq. 5 allows the calculation of the exposure age of a non-eroding surface from its measured ^{36}Cl concentration (Eq. 6):

$$(6) \quad t = \frac{-1}{\lambda} * (1 - \frac{N(t,z) * \lambda}{P_t(z)})$$

where $N(t,z)$ is the number of atoms per gram, $P_t(z)$ the production rate at z (Eq (3)), λ the decay constant of ^{36}Cl (Bierman, 1994).

In order to determine the erosion rates (for samples that are considered to be at steady state erosion) we use Eq. 7.

$$(7)\ \varepsilon = \frac{\Lambda}{\rho} * (\frac{P_t(0)}{N(t,z)} - \lambda)$$

where ε is the erosion rate [cm/year] for rock sample, $N(t,z)$ number of atoms per gram, $P_t(0)$ the production rate at z = 0 (Eq (3)), λ the decay constant of ^{36}Cl, ρ the rock density, Λ the attenuation length the attenuation length for fast neutron (160 g*cm^{-2})(Lal, 1991) .

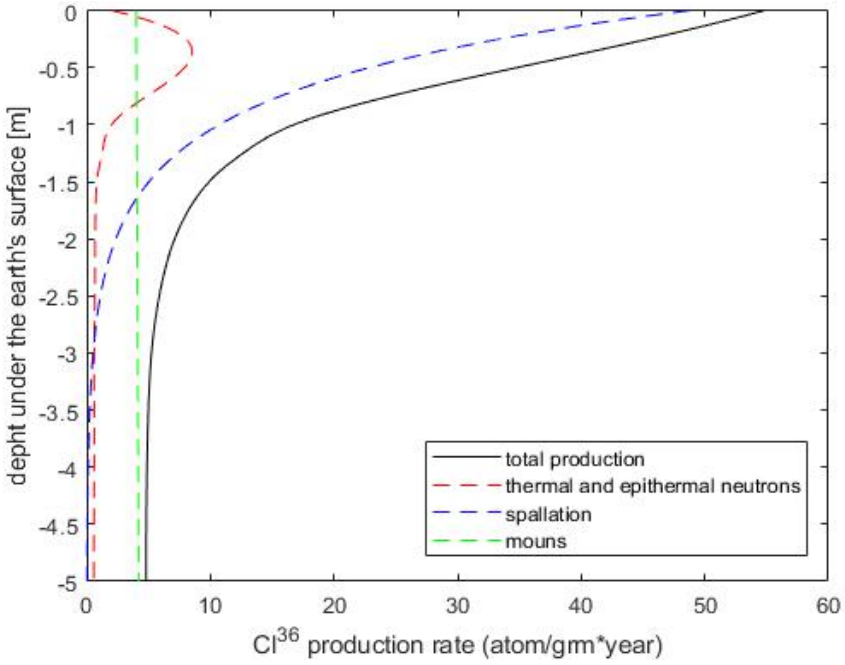

Figure. 5: Contribution of the various cosmogenic production pathways to the overall production rate [atoms/gram rock per year] of in situ ^{36}Cl in the upper 5 m of the earth's surface in rocks with low Cl concentration. As can be seen, the total production profile gives an exponentially ^{36}Cl shape which fades with depth.

1.6. Applying ^{36}Cl cosmogenic exposure age to reconstruct the exposure history of carbonate bedrock fault scarp.

Many studies around the world, in general, and around the Mediterranean area, in particular, used cosmogenic ^{36}Cl to date the exposure history of carbonate bedrock fault scarps, and then deduce possible earthquake scenarios (e.g., Benedetti et al., 2002; Mitchell et al., 2001; Mozafari et al., 2019; A Schlagenhauf et al., 2011; Tesson et al., 2016; Tesson & Benedetti, 2019; Zreda & Noller, 1998).

In order to date the exposure history of carbonate bedrock fault scarps, we first must understand how cosmic rays interact with the different parts of the fault scarp. So, we will start with dividing the fault scarp into two main parts:

1) The buried part is covered by the hanging wall (which may be rock or a colluvial wedge). This cover shields some of the secondary cosmic ray particles from reaching the buried fault scarp. The blocking of the cosmic rays increases with the fault scarp

depth. As a result, the ^{36}Cl concentration from the top of the buried fault scarp (the earth's surface) to a few meters under the earth's surface, will follow an exponentially ^{36}Cl concentration profile which fades with depth (fig. 6,7). The magnitude of the exponent is determined by the density of the hanging wall material and by its rate of erosion.

2) An exposed part. In this part all points on the scarp are exposed to the same portion of the sky (determined by the scarp angle). However, points at the upper part of the scarp (from the top of the scarp to ~3 meters below the top) are also bombarded by cosmic particles which can travel through the foot wall (fig. 6,8) (Schlagenhauf et al., 2010).

When an earthquake occurs, causing a surface rupture, the upper most section of the buried part of the scarp is instantaneously exposed. The initial ^{36}Cl concentration of the newly exhumed section has an exponential shape because it was shielded below the surface before the earthquake. However, once exposed, ^{36}Cl is produced, and accumulates along the newly exposed section at a uniform rate. As a result, the absolute values (i.e. concentrations) of ^{36}Cl increase while preserving the exponential profile shape (Fig. 8). Therefore, repeated earthquakes which exhume at discrete events deeper portions of the scarp, with sufficient quiescent intervals between events, will form a ^{36}Cl concentration vertical profile which takes

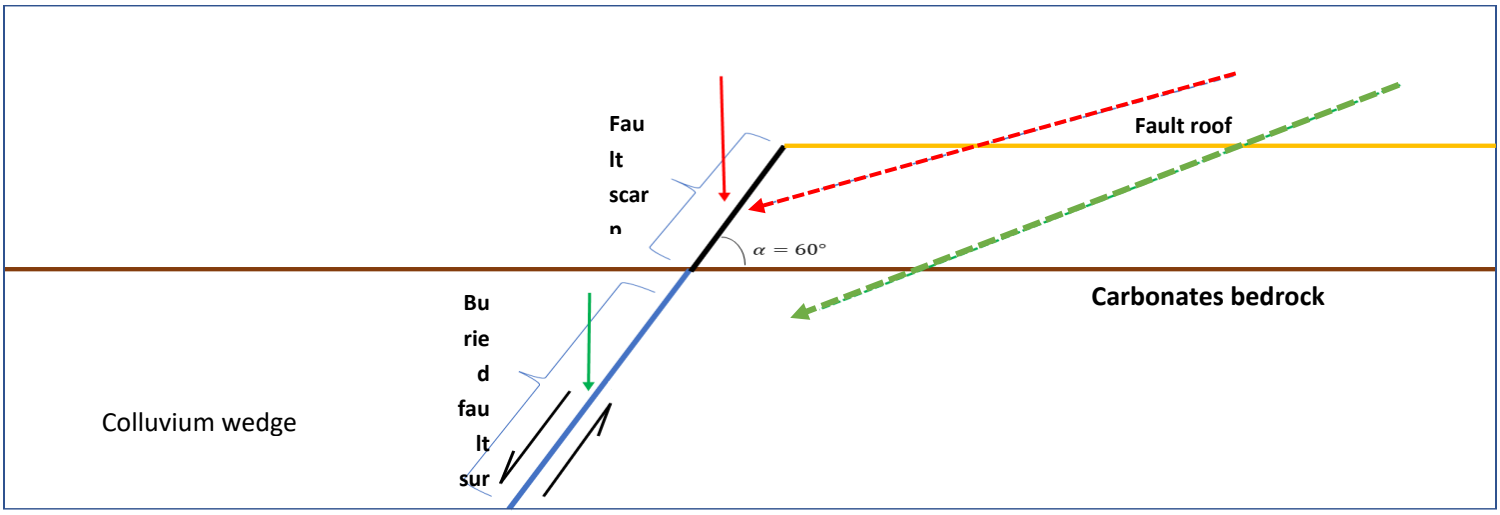

Figure. 6: Schematic representation of the geometry of a normal fault scarp. The solid red arrow indicates the cosmic particles that hit the exhumed fault plane, the solid green arrow indicates the cosmic particles that pass thought the colluvial wedge and hit the buried fault plane. The two dashed arrows indicate the cosmic particles that enter from the fault roof and pass through the bedrock and hit the fault surface: the red dashed line for the exhumed part and the green dashed line for the buried part. In most cases, the green dashed line will be attenuated before it reaches the fault plane.

a shape of a series of exponential sections separated by sharp discontinuities. The recurrence interval (i.e. the time between events) must be long enough to enable the buildup of an exponential profile within the buried part after each earthquake and shift the exponential curve of the exposed part sufficiently such that it can be distinguished from the adjacent exponential curves. If the recurrence interval is short the buried inherited concentrations will be uniform and low. The discontinuity points reflect boundaries between each major earthquake that caused surface rupturing, while the vertical separation between two successive discontinuities provides a measure of the displacements produced by the earthquakes (fig. 9) (Benedetti et al., 2002; Schlagenhauf et al., 2010).

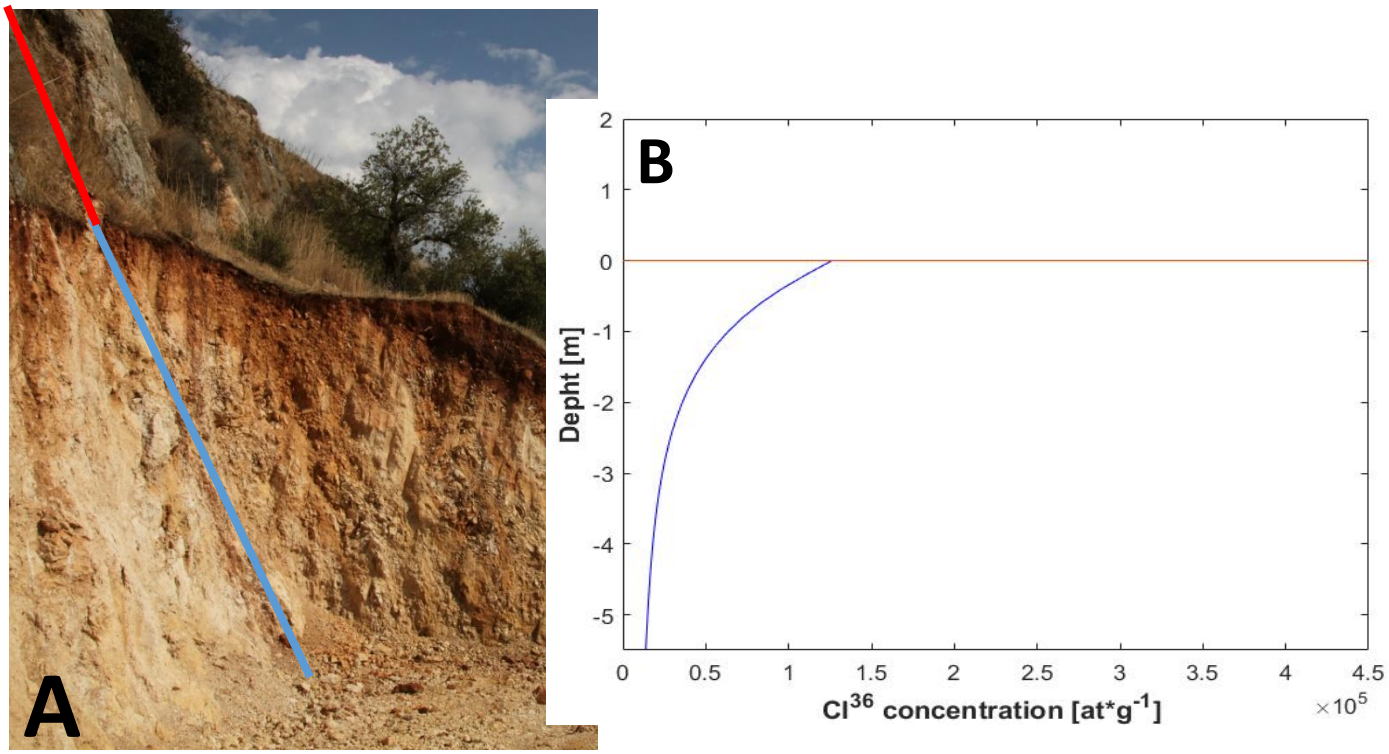

Figure. 7: (A) An excavation perpendicular to the strike of Deir Al-Assad fault. Red line outlines the exhumed part of the fault , and blue outlines the buried part. (B) a Theoretical profile of ^{36}Cl concentrations of the buried fault surface versus depth. This profile developed during 2Kyr of seismic quiescence considering production rate equal to that calculated for the Deir Al-Assad fault. The concentration profile is exponential because of the attenuation of the cosmic particle flux with depth.

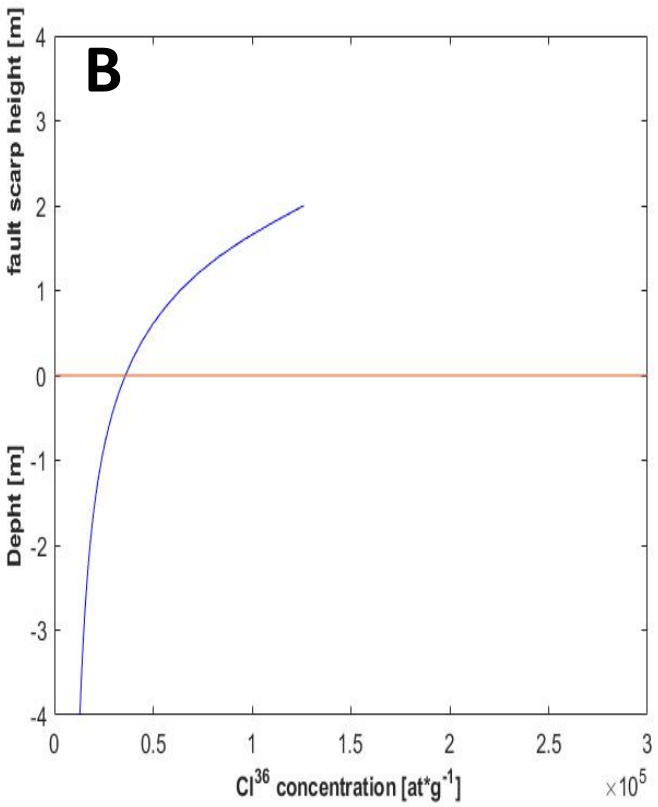

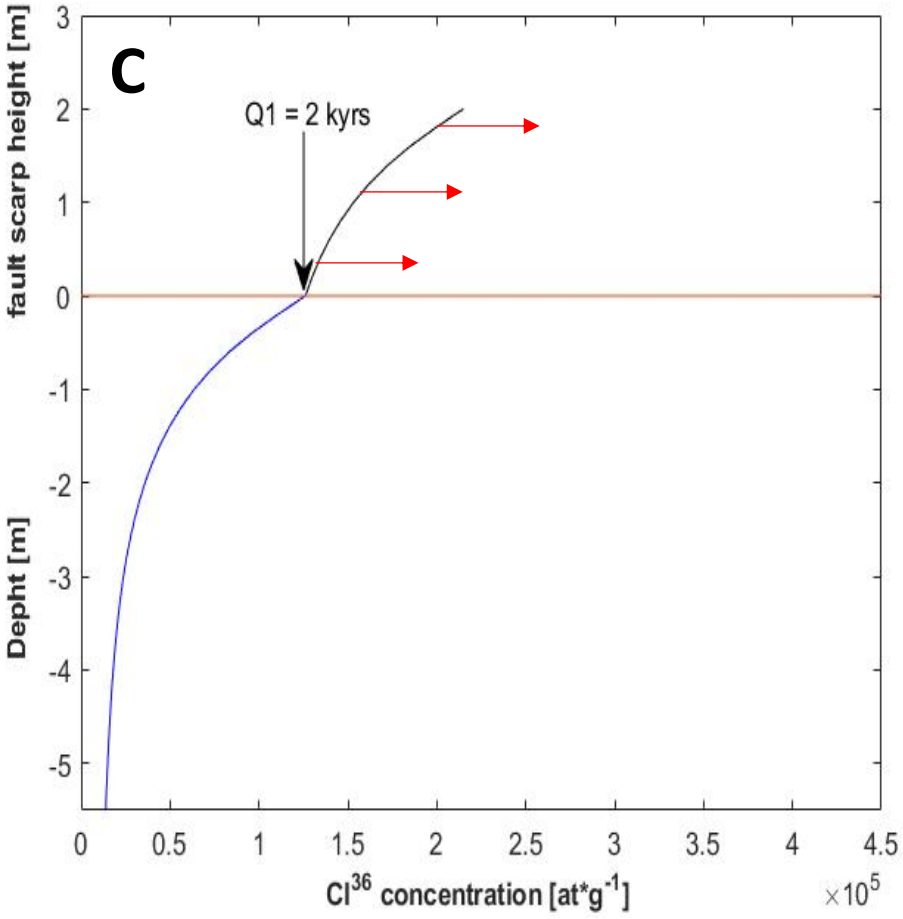

Figure 8: (A) Deir Al-Assad fault scarp.

(B) A scenario in which a section of the buried part of the fault scarp (red line in (A)) was exhumed by an earthquake. If we sample it immediately after the earthquake, we will get the same exponential ^{36}Cl concentration profile shown in fig (7).

(C) Same scenario as in (B) but now we sample the exhumed section (red line in (A)) and the buried part of the fault scarp 2Kyr after the earthquake. Because there is no colluvium above the exhumed section, it accumulates ^{36}Cl uniformly along the entire section. The red arrows outline the enrichment of the exhumed section with ^{36}Cl compared to the buried part. This difference produces a discontinuity point in

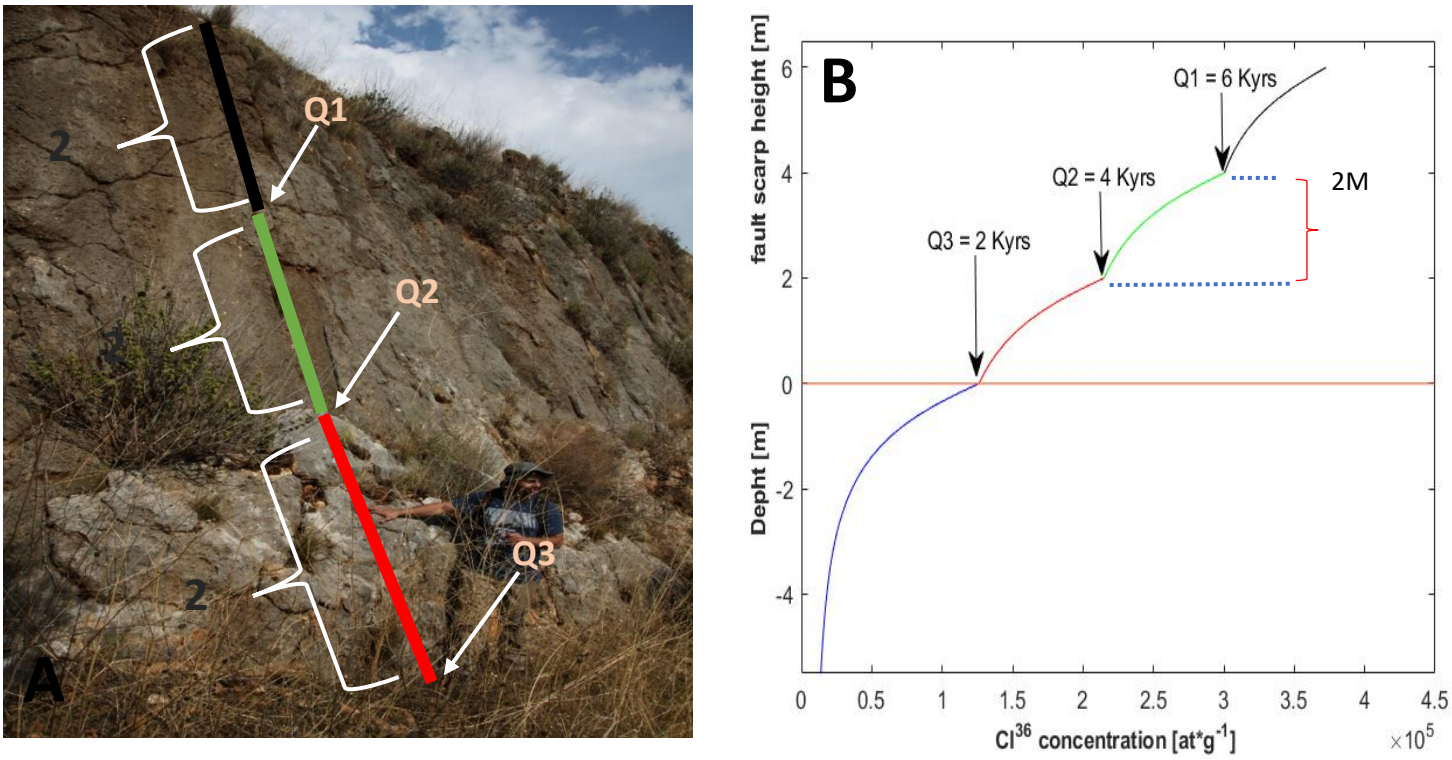

Figure 9: A scenario in which a fault scrap is exposed by a sequence of three similar, regularly spaced earthquakes, with a recurrence interval of 2 kyr, vertical slip of 2 m, and pre-exposure duration of 2 kyr. (A) Photo of the Sajur fault scarp and the hypothesized sections exhumed by each earthquake. Red, green, and black lines indicate the sections exhumed by each earthquake and correspond to the colors in (B).
(B) If we sample the fault scarp 2 kyr after the last earthquake we will find a ^{36}Cl concentration profile with a series of exponential sections separated by sharp discontinuities (marked by black arrows). Each discontinuity point indicates the occurrence of an earthquake. For example, the green exponential section is separated by two sharp discontinuity points (Q1 and Q2). Q2 indicates the earthquake that exhumed this section, and the vertical separation between Q1 and Q2 provides the displacements produced by this earthquake. This green exponential section in (B) is outlined by the green line in (A).

2. Research motivation and goals

Despite the many studies that investigated the exhumation history of fault scarps, the interaction between multiple normal fault segments and their effect on earthquake magnitude and landscape evolution is still unclear. While empirical scaling relations suggest that only long faults can produce large amount of surface slip, many paleoseismological studies, especially those conducted on fault systems that consist of closely spaced fault segments, show that large displacement occurs on relatively short faults. In addition, a detailed description of the way that fault linkage affects escarpment initiation is scarce. Here I study the exceptional Bet Kerem fault system in order to:

1. Determining whether fault linkage can explain the relatively high surface rupture amount observed by Mitchell et al (2001) at the Nahf East segment. By that, a better understanding of the effect of fault linkage on earthquake magnitudes and surface rupturing.

2. Provide a detailed description of the way fault linkage at the Bet Kerem system affects escarpment initiation.

3. Determining the seismic hazard posed by the Bet-Kerem fault system.

3. Methods

3.1 Fault traces and Lithologies

The fault traces of all major segments in the Bet-Kerem Fault System (BKFS) were identified using published maps (e.g., Bogoch & Sneh, 2008; Sagy et al., 2013; Siman-Tov et al., 2022; Sneh, 2004, 2006) , field observation, Digital Terrain Model (DTM) and aerial photos. The focus of our observations and field mapping was on the fault tips and the relay ramp zones, aiming to determine whether fault linkage exists and if so, its type (soft or hard). The determination of the exposed lithologies on both sides of each fault segment was done using published geological (e.g., Bogoch & Sneh, 2008; Siman-Tov et al., 2022; Sneh, 2004, 2006), and supported by field mapping and observations. Moreover, we mapped the spatial distribution of fault scarp of the BKFS. Each investigated fault scarp was qualitatively compared, in terms of its level of weathering (e.g depth and density of pitting) and morphology to the previously dated Nahf east fault (Mitchell et al., 2001).

3.2. Along strike topographic and stratigraphic throw profiles

Several geological cross-sections were constructed along the strike of each of the investigated fault segments. The cross-sections were constructed with equal intervals between both ends of the fault segment. For each cross-section, I determined the topographic throw and their error (the average deviation for 10 different topographic throw measurements within a 100-meter zone) using high-resolution topographical DTM (0.25 m2 pixel size), and for the Ahihud segment, a low-resolution DTM (625 m2 pixel size) (Hall, 1993). The stratigraphic throw is calculated from the vertical difference of a datum surface exposed on both sides of each fault. In general, the chosen datum surface is the top or the base of a geological formation that is exposed on both sides of the fault or is exposed on one side of the fault and can be determined on the other side. In this study area I used the top of the Menuha Formation as a datum. This datum is exposed along all the downfaulted blocks but eroded from uplifted blocks. Therefore, to determine the stratigraphic throw for each cross-section, I added the thickness of the eroded stratigraphic sequence to the uplifted. The Menuha Formation thickness ranges between 50 – 150 meters. In contrast, the thickness of the layers beneath the Menuha Formation is hardly changed. (Freund, 1959). Therefore, the stratigraphic throw error is 100 meters. Using the cross-sections data, I reconstructed the along-strike topographic and stratigraphic throw profile, in which each point represents a cross-section, and the location (x-axis) is the distance from the eastern fault tip (Fig. 10).

3.3. Along strike S-T value profiles

The S-T value profile is defined as the difference between the stratigraphic (S) and the topographic (T) throws at the same point along the fault (Fig. 11). This value is the missing stratigraphic section that was eroded from the uplifted block. Therefore, the along the strike S-T value profile are a good quantity to describe the total erosion versus distance along the strike of the fault. A analyzing and comparing the shape of the S-T value profiles with the topographic and stratigraphic throw profiles can help to determine during which faulting phase most of the erosion of the uplifted block took place. For example, fault that shows symmetric S-T value profile and asymmetric topographic and the stratigraphic throw profiles, is indicate that the erosion phase is related to the pre-hard-link phase.

3.4. Along strike fault scarp profiles

For all fault segments in the study area, having fault scarps, I plotted high-resolution topography profiles of the scarps using a DTM (0.25 m^2 pixel size) (Fig. 12). These profiles are used to determine whether the studied segments are linked together. The same profiles were also compared to the shape of topographic and stratigraphic profiles to better understand changes between long and short-term fault evolution.

3.5. From fault scarp sampling to modelling its exhumation history

3.5.1. Selected sites and field sampling

To reconstruct the seismic history of a fault, the fault must have a scarp that has been exposed by seismic events rather than erosional processes. The selected sites on each fault scarp must be uneroded or, at the most, insignificantly eroded (Mitchell et al., 2001; Schlagenhauf et al., 2010). Based on our fault scarp mapping, I selected two segments for ^{36}Cl exposure: one site is located on the Bet-Kerem segment (11 m scarp height); the second site is located on the Sajour segment (5.5 m scarp height). At each site, samples were collected at 30 cm intervals using a rock drill, along vertical transects from the already exhumed fault scarp, and 2 samples from the buried part at 30 and 60 cm below the surface. Each sample is composed of four to six cores. Core diameter is 2.54 cm, and their length ranges from 4 to 10 cm, such that the total weight of each sample is at least 150 grams (Mitchell et al., 2001). Overall, 58 samples were collected: 38 from the Bet-Kerem segment and 20 from the Sajour segment.

3.5.2. Sample preparation for chemical Cl extraction

All cores of a single sample are crushed together, and the 250–500 µm fraction is isolated. This fraction is leached, dissolved, and spiked with a Cl spike with a known $^{35}Cl/^{37}Cl$ ratio which is significantly different from the chlorine isotopic natural ratio (Stone et al., 1996). Cl is then separated following the procedures detailed in Schimmelpfennig et al., (2009), and the end product is precipitated as AgCl.

3.5.3. AMS measurements and ^{36}Cl concentration

Chlorine isotopic ratios ($^{36}Cl/^{35}Cl$, $^{36}Cl/^{37}Cl$ and $^{35}Cl/^{37}Cl$ ratios) are measured using an accelerator mass spectrometer (AMS) at ASTER, CEREGE, Aix en Provence, France.

3.5.4. Production rate determination

To determine the ^{36}Cl production rate, latitude, elevation, fault scarp dip, fault scarp rock chemical composition, and the density of the hanging wall material are required. In order to determine the chemical composition about 5 grams of each sample were dissolved, and the chemical composition was determined using ICP-MS.

3.5.5. Modelling the seismic exhumation history from the 36Cl profile

The ^{36}Cl profile of the sampled fault scarp is a result of episodic fault motions. In order to reconstruct the seismic exhumation history, a model is required. I used Cowie et al. (2017) model which is a forward Monte-Carlo model that is based on Schlagenhauf et al. (2010) numerical model. The Model input parameters are the scaling factors of the fault scarp which are a function of the geographic location and elevation and calculated using Stone (2000) equations, colluvium slope angle, colluvium density, chemical composition, faults scarp dip, rock density, and the slope angle of the escarpment above the scarp (Table. 5). Moreover, for each sample, the model gets the sample position on the fault scarp, their chemical composition, and their ^{36}Cl concentration. The model runs include 200k iterations, where each iteration represent a different seismic exhumation scenario. For each seismic exhumation scenario, the model calculates a theoretical profile of ^{36}Cl which is then compared to the measured one. The scenarios that yield the most similar profile to the measured one are considered to well-represent the exhumation history of the fault scarp.

3.5.6. Quality check of earthquake history scenarios

The modeled ^{36}Cl profile depends on a large number of parameters. As a result, a good fit between the measured and the modeled profiles can be achieved by several scenarios. Thus, the modeled profile quality is tested by three different statistical methods: 1) weighted root mean square (RMSw), 2) Chi-square test ($\chi 2$) and, 3) the Akaike Information Criterion (AICc) (Akaike, 1974; Cowie et al., 2017; Schlagenhauf et al., 2010).

3.6. Estimating the most realistic earthquake scenario.

The fault scarp exhumation history is representing the amount of surface slip and the age of the events. Each of these slip events could be generated by two different earthquake scenarios or a combination of them. Which are [1] the moderate earthquake scenario; in which a large number of moderate earthquakes occur during a relatively short period of time, each producing a small amount of surface slip, which together generate the observed large surface rupture amount. [2] The large earthquake scenario, in which a large earthquake generates long surface rupture, which can be either a long continuous fault or short segments that rupture together, resulting in a large amount of surface slip. The dated segments are ~ 5km in length, thereby, they can generate at most several centimetres of surface slip in one single event. Based on that, the synchronized surface rupture activity that is combined with a large amount of surface slip seems to indicate multi-segment rupture rather than a moderate earthquake scenario. Therefore, I first determined whether the dated fault scraps exhibit synchronized surface rupture activity. Then, for each synchronized activity was examined for the possibility that it indicated a multi-segment rupture. While for the surface rupture events that didn't show synchronized activity the moderate earthquakes scenario has been chosen to be the case.

4.Results

4.1. Along-strike topographic and stratigraphic throw profiles

Here I present the results of seven, along-strike, topographic and stratigraphic throw profiles of the BKFS. The Rama segment is the most eastern studied segment (fig. 4), where only the topographic profile is provided (table 1 and fig 10A). It has an asymmetric topographic profile, with the maximum topographic throw located near the western fault tip (where it intersects the Peki'in fault). West to Rama is the Sajur segment, both, topographic and stratigraphic profiles are asymmetric (table. 1 and fig. 10B). The maximum topographic and stratigraphic throw located near the eastern fault-tip where it intersects with the Peki'in fault. Westward, at the Nahf segment, the stratigraphic throw profile is close to an asymmetric shape than a symmetric and shows an asymmetric topographic throw profile with a peak located close to its eastern side (table 1 and fig. 10C). The most western three segments in the study area: Deir Al-Assad, Majd El-Krum, and Ahihud show symmetry in both the topographic and stratigraphic along-strike profiles (table 1 and fig. 10 D, E and F). Lastly, for the Nahf East

segment, I provide only a topographic profile, which show profile is asymmetric profile, with a peak located close to the northwest end of the fault, where it intersects with the Nahf fault (table 1 and fig. 10 G).

4.2. S-T value profiles

As mentioned earlier, the S-T value is the missing stratigraphic section that was eroded from the uplifted block, and their profile provides a quantitative description of how the thickness of the missing stratigraphic section changes along the fault. All the investigated segments, excluding the Sajur fault, show symmetric (or about symmetric) along-strike S-T profiles (table 2 and fig. 11). The Sajur segment shows an asymmetric along-strike S-T profile, with a maximum located near the eastern fault tip where it intersects with the Peki'in faults. For the Rama and the Nahf East segments I only provided along strike topographic throw profiles, therefore, I didn't provide S-T value profiles.

Segment name	Stratigraphic profile shape	Max stratigraphic throw	Topographic profile shape	Max topographic throw	Notes
Rama	-	-	Asymmetric	580 -550	The max topographic throw located close to the western fault tip
Sajur	Asymmetric	710 - 610	Asymmetric	440 -420	The max topographic and stratigraphic throw are located close to the eastern fault tip
Nahf	Close to symmetric	510 - 410	Asymmetric	340 -320	The max topographic throw located close to the eastern fault tip
Deir Al-Asad	symmetric	420 -320	Symmetric	240 -220	

Majd al-Krum	symmetric	370 - 350	Symmetric	310 - 290	
Ahihud	symmetric	180 – 150	Symmetric	130 – 110	
Nahf East	-	-	Asymmetric	110 – 90	The max topographic throw is located close to the northwestern fault tip (where it intersects with the Nahf fault)

Table. 1: A summary of the along-strike topographic and stratigraphic profiles of the investigated faults (fig. 10). For each fault the maximum stratigraphic and topographic throws are given along with the shape of the along-strike profiles, where for symmetric profile the maximum throw is located at the fault center while for an asymmetric profile the maximum is located away from the fault center.

Fault name	S-T value profile shape	Max S-T value	Notes
Sajur	Asymmetric	320 - 200	The maximum S-T value located close to the eastern fault tip
Nahf	Symmetric	260 – 140	
Deir Al-Asad	symmetric	200 - 80	
Majd al-Krum	Symmetric	90 – 40	
Ahihud	Symmetric	70-20	
Nahf East	-	-	

Table. 2: A summary of the along-strike S-T values of the investigated faults (see also fig. 11). For each fault the maximum S-T value and its profile shape (symmetric or asymmetric) are given.

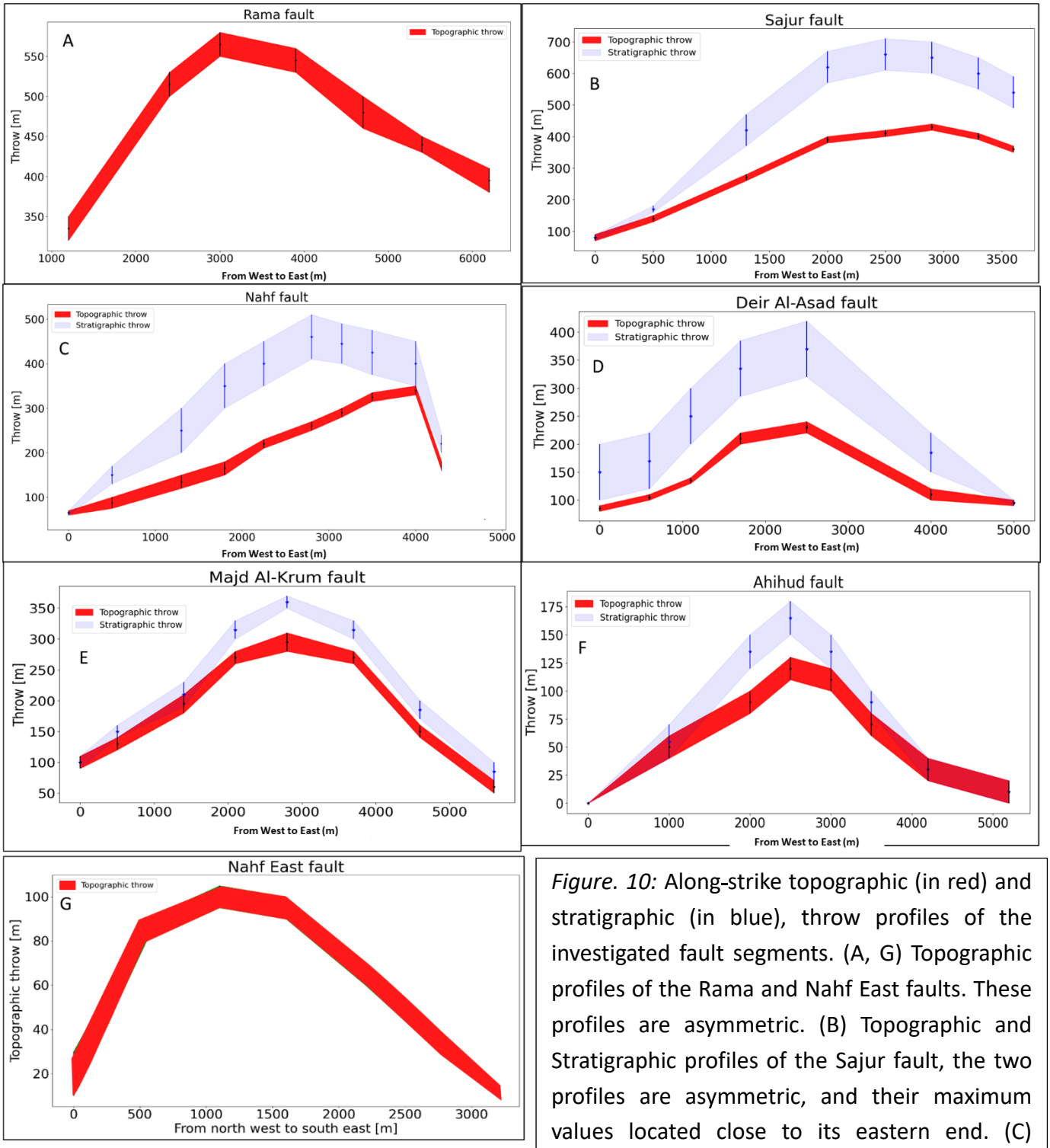

Figure. 10: Along-strike topographic (in red) and stratigraphic (in blue), throw profiles of the investigated fault segments. (A, G) Topographic profiles of the Rama and Nahf East faults. These profiles are asymmetric. (B) Topographic and Stratigraphic profiles of the Sajur fault, the two profiles are asymmetric, and their maximum values located close to its eastern end. (C) Topographic and Stratigraphic profiles of the Nahf fault. The topographic profile is asymmetric with a maximum value located close to the eastern tip. The stratigraphic profile is symmetric. (D) Dier Al-Asad, (E) Majd Al-Krum, and (F) Ahihud, for all both the Topographic and Stratigraphic profiles are symmetric.

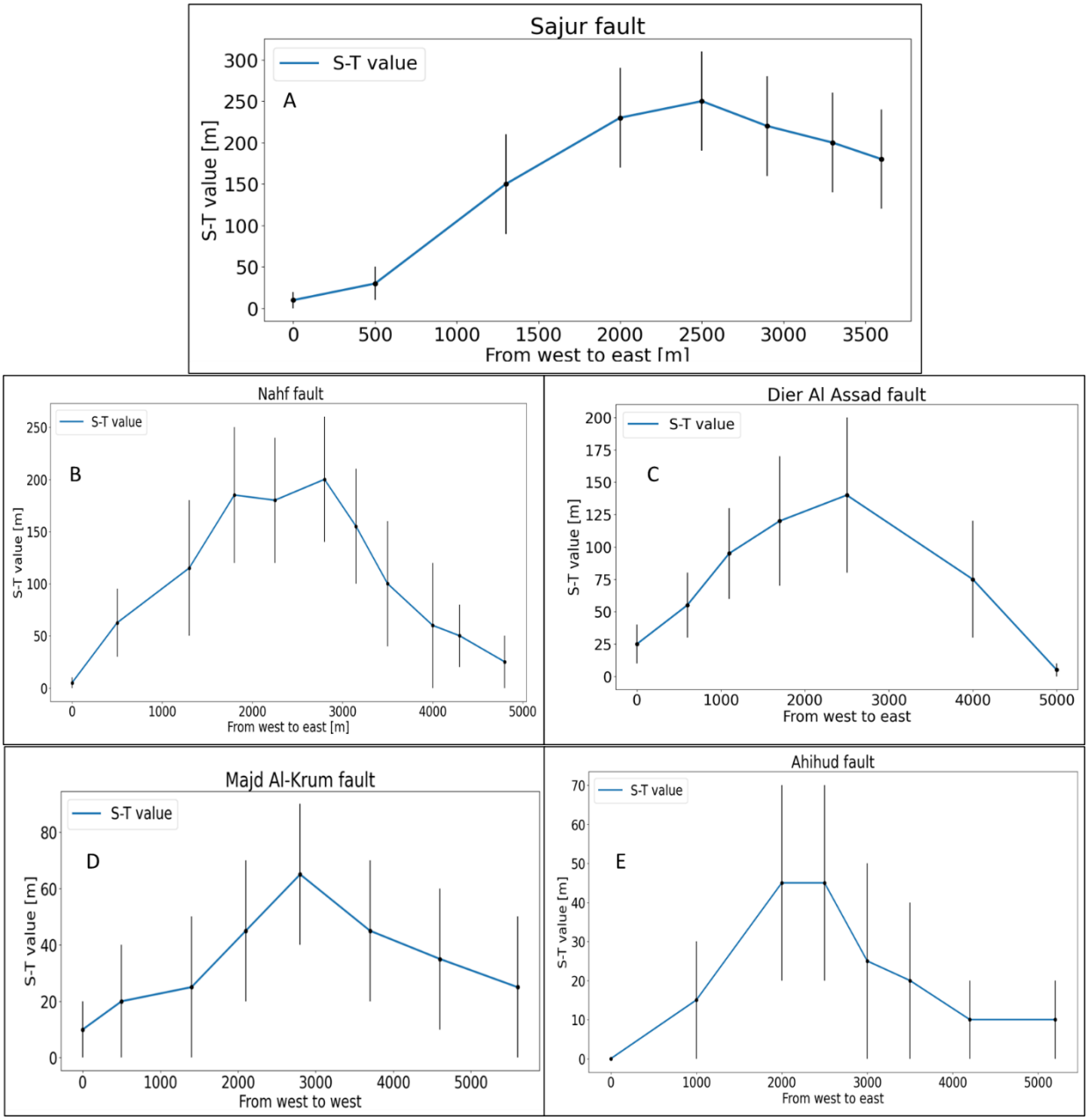

Figure. 11: Along-strike S-T profiles of the investigated faults. (A) The Sajur fault shows asymmetric profile while its maximum value located close to the eastern fault tip. (B) Nahf (C) Dier Al-Asad, (D) Majd Al-Krum, and (E) Ahihud faults, show symmetric profiles.

4.3. Along-strike fault scarp profiles

In addition to the topographic and stratigraphic throw profiles, for four out of the seven studied faults (Sajur, Nahf, Nahf East, and Deir Al-Assad) I constructed along-strike fault scarp profiles using the DTM (fig. 12). Each profile display how the scarp height is distributed along the segment. The profiles of the Sajur and Nahf East faults show asymmetric along-strike fault scarp profiles, with max scarp height of 5.7 m and 9.5 m respectively. The Dier Al-Assad fault scarp show a symmetric profile (max fault scarp height 11.5 m). The along-strike scarp profiles of the three faults are correlated with their along-strike topographic throw profiles (figs. 10 and 12). However, the Nahf fault scarp profile includes two asymmetric shapes separated by a saddle which is located at the intersection with the Nahf East fault. This shape is inconsistent with the topographic throw profile (fig. 10C).

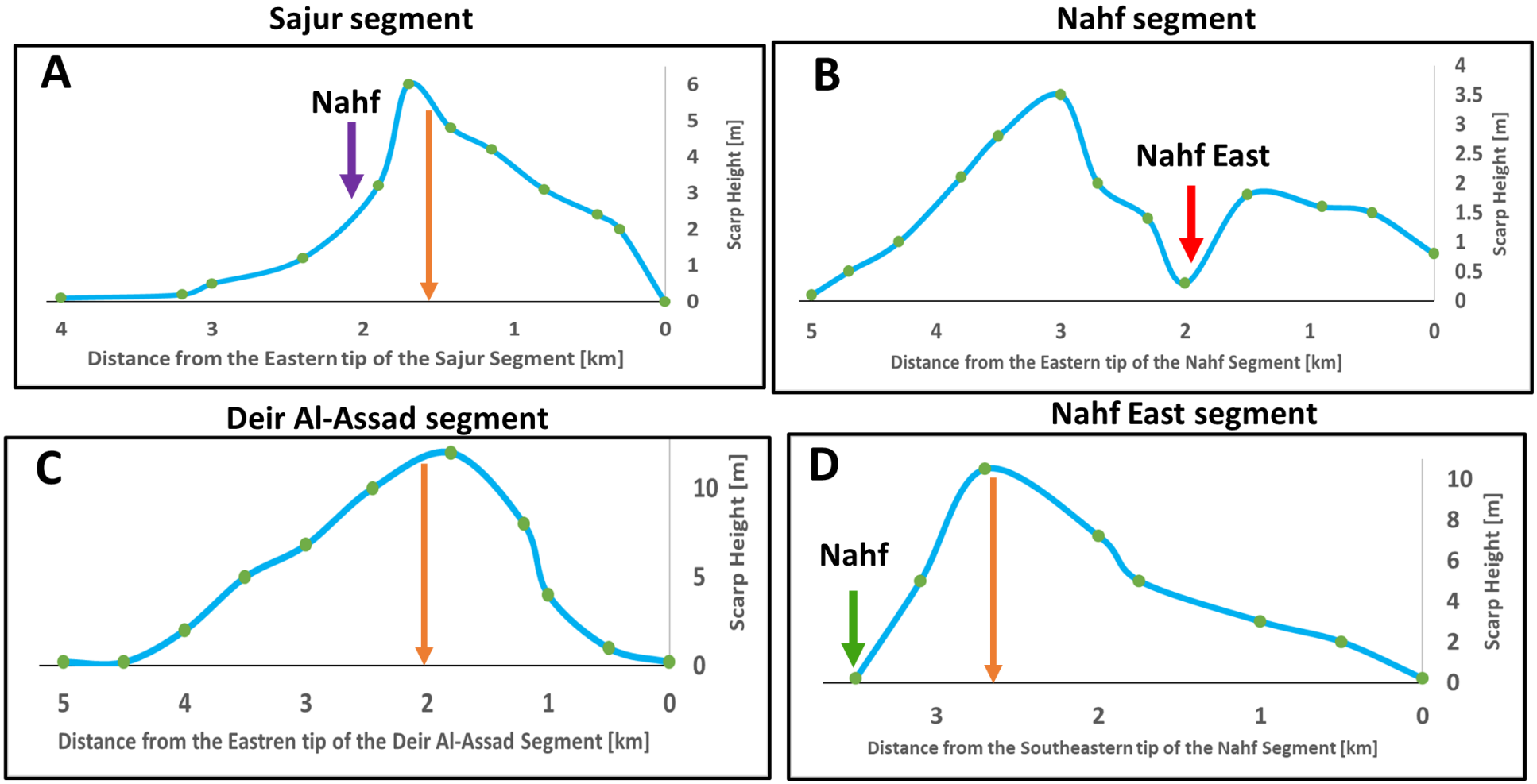

Figure 12. Along the strike fault scarp height. (a) for Sajut segment, (b) for Nahf segment, (c) Deir Al-Assad segment, and (d) Nahf East segment. The orange arrow outlines the samples site at the investigated segments, the purple arrow outlines the location of the intersection of the Nahf segment with Sajur, the red arrow the location of the intersection between the Nahf segment with Nahf East segment, and the green arrow the intersection of Nahf East segment with Nahf.

4.4. Cosmogenic Cl^{36} and chemistry results

For each sample the $^{36}Cl/^{35}Cl$, $^{36}Cl/^{37}Cl$ were measured using accelerator mass spectrometer (AMS) at ASTER, CEREGE, Aix en Provence, France. From these ratios, the ^{36}Cl and total Cl were calculated. Major and trace element concentrations were measured using ICP-MS. Concentrations were used to determine production rates which, in turn, were applied in the model to determine the exhumation history of the fault scraps. Table 3 shows the ^{36}Cl of all Sajur fault samples, and Table 4for Deir Al-Assad samples. For samples major and trace element concentrations see supplementary table S2 for Deir Al-Assad and S1 for Sajur.

Sampel name	Height on fault scarp (cm)	Cl (ppm)	^{36}Cl (at. g^{-1} rock)	^{36}Cl uncertainty (at. g^{-1} rock)
sj -(-60)	-60	8.050125	92531.296	4626.564798
sj-(-30)	-30	9.021745	98040.1678	4902.008391
sj-0	0	12.02744	109058.389	5812.506758
sj-30	30	13.1687	131392.337	6569.61685
sj-60	60	14.71523	122622.191	6131.109541
sj-90	90	12.23713	149101.568	8276.407127
sj-120	120	26.06346	183485.002	9544.932286
sj-150	150	9.831984	213078.369	10653.91846
sj-180	180	15.73896	208824.493	10441.22464
sj-215	215	9.617962	183455.786	9172.789279
sj-240	240	9.513618	206252.796	10312.63979
sj-270	270	9.508085	227026.32	11351.316
sj-300	300	9.590571	228441.926	11422.09632
sj-330	330	7.603766	242259.669	12112.98343
sj-360	360	11.58116	267704.278	13385.2139

sj-390	390	11.14517	249891.435	12494.57176
sj-420	420	10.06403	300706.736	15035.33679
sj-450	450	7.226143	325550.318	16277.51591
sj-510	510	8.636378	372925.788	18646.28939
sj-540	540	10.32452	409997.842	20499.89209

Table. 3: ^{36}Cl (atoms in 1 gram rock)**,** and Cl concentrations in ppm of the Sajur fault samples.

Sampel name	Height on fault scarp (cm)	Cl (ppm)	^{36}Cl (at. g^{-1} rock)	^{36}Cl uncertainty (at. g^{-1} rock)
btf-1080	1080	75.43139	630734.7	27247.91
btf-1050	1050	48.70844	464083.8	21426.01
btf-1020	1020	37.74313	494665.6	22326.82
btf-990	990	39.85166	466997.8	20709.9
btf-960	960	46.3974	436856	19453.47
btf-930	930	56.23924	458031.7	19652.9
btf-900	900	22.28139	431126.2	18797.59
btf-870	870	27.2326	400777.2	17431.41
btf-840	840	26.6053	382955	17112.68
btf-810	810	36.23346	362181.8	15651.96
btf-780	780	27.22896	376615.2	16631.6
btf-750	750	32.55209	353611	18918.19
btf-720	720	15.00559	264184.2	13272.17
btf-690	690	11.95499	246787.6	16965.17
btf-660	660	42.60591	278898.7	13247.69
btf-630	630	38.22819	255903.1	13264.41
btf-600	600	19.39383	237349.9	10657.01
btf-570	570	5.327995	192478.4	8603.784

btf-540	540	9.90718	169217.6	10447.25
btf-510	510	32.69157	175597.6	8829.887
btf-480	480	28.34804	161081.2	9185.511
btf-450	450	13.03646	136970.3	7495.661
btf-420	420	12.02876	138927.1	7122.014
btf-390	390	5.57501	151942.9	7458.993
btf-360	360	3.924937	175066.6	9435.03
btf-330	330	22.94828	133416.9	7087.84
btf-300	300	20.61242	121639.8	7720.805
btf-270	270	4.360314	140011	7581.965
btf-240	240	6.007766	129280	7661.76
btf-210	210	2.475725	119946.9	7544.507
btf-180	180	5.511943	102549.8	5813.179
btf-150	150	4.881501	114306.6	6505.026
btf-120	120	10.98991	93206.71	5731.652
btf-90	90	18.58982	87788.76	5206.448
btf-60	60	47.6601	95271.37	6323.159
btf-30	30	29.27972	94528.89	5958.505
btf-0	0	32.33713	91503.03	5636.977
btf-(-30)	-30	34.62127	109617.1	6265.041
btf-(-60)	-60	9.86015	87228.2	9021.172

Table. 4: ^{36}Cl (atoms in 1 gram rock)**,** and Cl concentrations in ppm of the Deir Al-Assad fault samples.

4.5. Faults parameters

Besides the chemical composition, other parameters are needed for the model in order to determine the fault scrap exhumation history. These include geographic location and elevation of the fault scarp, colluvium slope angle, colluvium density, faults scarp dip, scarp rock density, and the slope angle of the escarpment above the scarpTable 5 shows these parameters for the Sajur, Nahf East and Deir Al-Assad segments.

Fault name	Latitude	Longitude	Elevation [m] a.s.l	Colluvium dip (deg)	Colluvium density (gr/cm^3)	Scarp dip (deg)	Scarp rock density (gr/cm^3)	upper scarp dip (deg)
Sajur	32.948	35.3366	560	20	1.5	68	2.7	30
Nahf East	32.983	35.3200	290	15	1.7	51	2.7	25
Deir Al-Assad	32.936	35.289	315	15	1.5	70	2.7	30

Table. 5: Model input parameters of the studied fault scarps.

4.5. ^{36}Cl Model results

4.5.1. Sajur segment

Model results of the Sajur segment indicate three distinct periods of surface rupturing. The first period during the early Holocene (12 ka – 11 ka), with over 1.5 meters of displacement, a second period with displacement of ~2.5 m, which occurred during the middle Holocene (7.5 ± 0.5 ka), and the third period during the late Holocene (4.2 ± 0.5) ka with displacement of ~1.5 m. In addition, the model results indicate on a pre-exposure duration of $\mathbf{15}^{+\mathbf{1.0}}_{-\mathbf{1.5}}\ \boldsymbol{ka}$. This period approximately represents the interseismic time before the oldest identified event. By that, another, oldest event is provided with an age of 28 - 25 ka. For this last event I can only suggest the timing without the amount of surface displacement (Fig. 13).

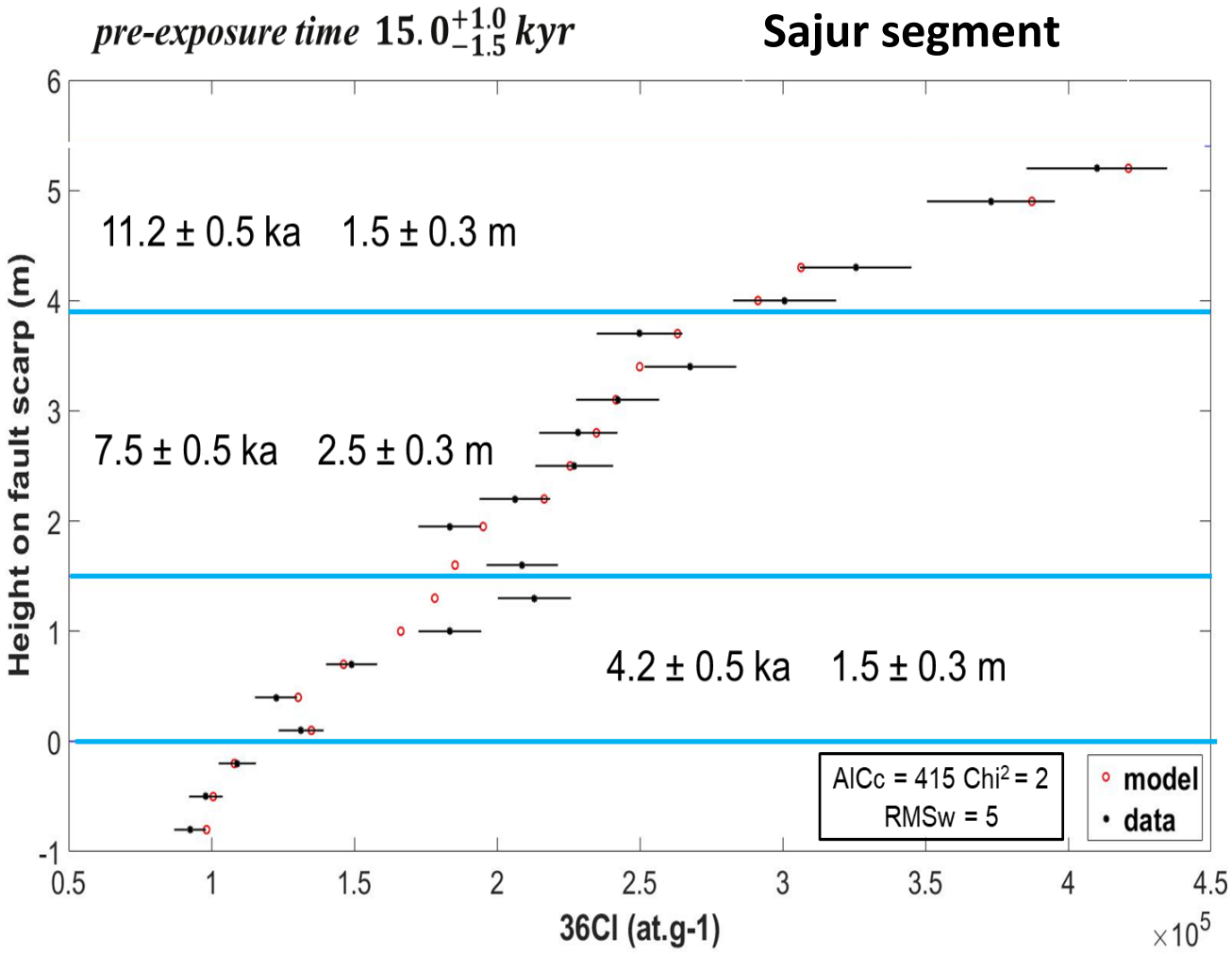

Figure. 13: The best fit exhumation history of the Sajur fault scarp suggests 3 slip periods, and a pre-exposure duration of 28 - 25 ka. ^{36}Cl data (black dots), modeled ^{36}Cl (red circles) versus scarp height. Blue lines indicate seismic events, their age and slip above the line (These results are based on figures s1 and s2, both are in the supplementary).

Model results of the Deir Al-Assad segmnet indicate six distinct periods of surface rupturing. The two first events occurred during the Late Pleistocene (29 ± 1 ka) and (24.5 ± 0.5 ka), respectively. Each of which produced ~1.5 meters of surface rupturing. During the Holocene three distinct periods of surface rupturing occurred (11.5 ± 0.5 ka), (7.5 ± 0.5 ka), and (4.4 ± 0.5 ka). Each of which produced ~2.5 meters of surface rupturing. In addition, another older event with age of 36 – 32 ka is provided by the pre-exposure duration (Fig. 14).

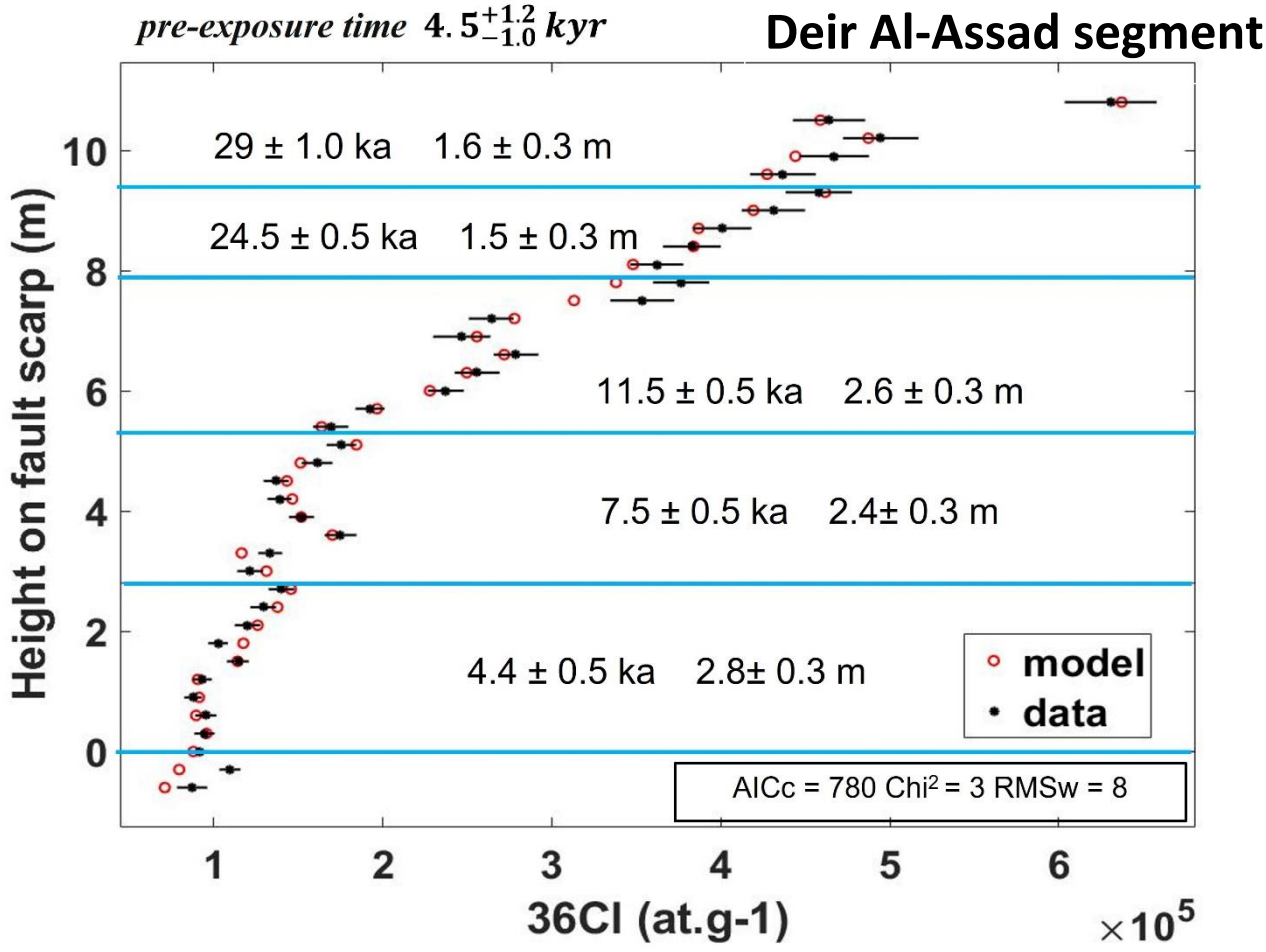

Figure. 14: The best fit exhumation history to the Deir Al-Assad fault scarp includes 5 slip periods, by considering the pre-exposure duration it provides another oldest event with age (36 - 32 ka). ^{36}Cl data (black dots), modeled ^{36}Cl (red circles) versus scarp height. Blue lines indicate seismic events, their age and slip above the line (These results are based on figures s3 and s4, both are in the supplementary).

4.5.3. Nahf East segment

Differently from the two other faults for the Nahf East segment I used Mitchell et al. (2001) data and Cowie et al. (2017) model to reconstruct the exhumation history of the Nahf east fault scarp. Model results of the fault indicate three distinct periods of surface rupturing. The first period during the early Holocene (11.8 ± 0.5 ka), with over 1.2 meters of displacement, a second period with displacement of ~ 6.5 m, which occurred during the middle Holocene (8.0 ± 0.5 kyr), and the third period during the late Holocene (4.3 ± 0.5 kyr) with displacement of ~ 2 m. In addition, by using the pre-exposure duration, another oldest event can be determined with age (26.5 – 30.0 ka) (Fig .15).

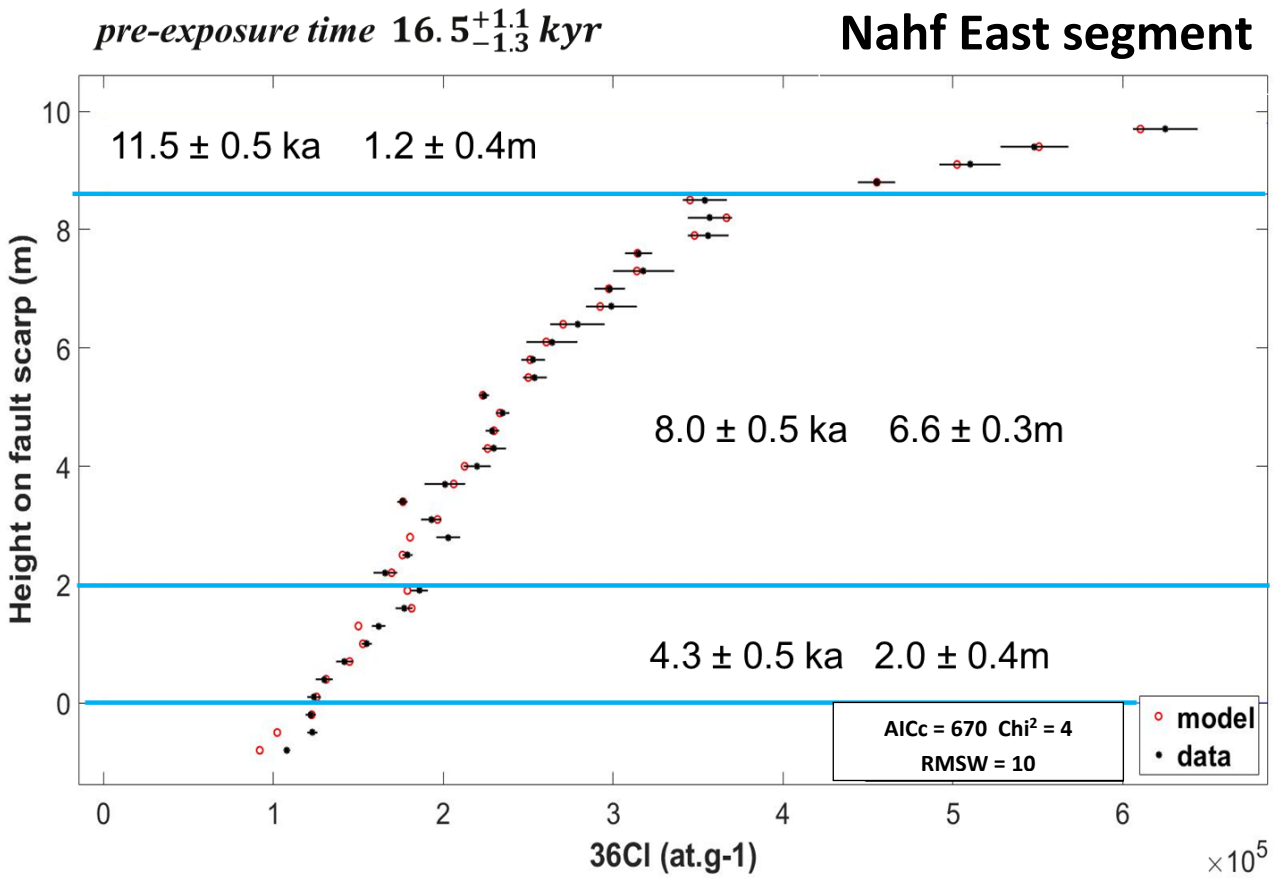

Figure. 15: The best fit exhumation history to the Nahef East fault scarp includes 3 slip periods. And, by using the pre-exposure duration, another oldest event can be determined with age (26.5 – 30.0 ka) ^{36}Cl data (black dots), modeled ^{36}Cl (red circles) versus scarp height. Blue lines indicate seismic events, their age and slip above the line (These results are based on figures s5 and s6, both are in the supplementary).

.

5. Discussion

5.1 The linked Bet Kerem fault system

The Bet Kerem fault system (BKFS) includes several fault segments positioned en-echelon, their traces observed at the base of the Zurim Escarpment (fig. 4). As the fault segments overlap, they form four relay ramps (fig 4) suggesting that the BKFS is a linked system. In order to determine whether the linkage between the segments is hard or soft, I focus on the relay ramp zones and on the along-strike profiles of each segment. The Sajur ramp, which is located between the Sajur and Nahf fault segments is a breached ramp. Therefore, the Sajur and Nahf faults are physically connected and are in fact hard-linked faults. Consequently, the Nahf segment topographic profile is asymmetric with the maximum throw close to the segment's eastern tip, where it is linked to the Sajur segment (fig. 1 and 10). The along-strike topographic profile of the Sajur segment and the Rama segments are also asymmetric, with maximum throws close to their intersection with the Peqi'in fault. Thus, the Sajur and the Rama segments are also hard linked (figs. 1, 4 and 10). The other ramps, which are located west the Sajur ramp, are not breached and only display rock bending. This suggests that the Nahf, Deir Al-Assad, Majd Al-Krum, and Ahihud faults are all soft-linked faults. This is consistent with their symmetric topographic profiles (figs. 4 and 10).

The scaling relationship $D = \gamma L$ also indicates that the BKFS is a linked system. Here I calculate value ϒ for each fault segment within the Bet Kerem fault system, by dividing the max stratigraphic throw by segment length. ϒ values decrease gradually from east to west, with $\gamma = 0.135 - 0.125$ for the Sajur segment to 0.04 at Ahihud segment (Figure 16C). As for the Rama segment, in the absence of a stratigraphic throw profile, I am unable to calculate its ϒ value, however, it shows the maximum topographic throw in the system (fig. 16B and 16E), which may indicate that it also has the highest ϒ value. The Ahihud segment is the only segment that shows a ϒ value that is close to 0.03, which is the average worldwide value of isolated fault segments (Schlische et al., 1996) (Cowie & Roberts, 2001; McLeod et al., 2000; Nicol et al., 2010; Papanikolaou & Roberts, 2007; Roberts & Michetti, 2004). Therefore, it can be said that the BKFS is a linked fault system that extends as far westward as the Ahihud fault, with a center located close at the Rama fault. In this discussion I concentrate only on the segments west of Rama. East of the Rama segment, landslides and structural complexity make it difficult to construct topographic and stratigraphic profiles.

5.2 Nahf fault and the S-T value significance

Apart from the Nahf segment, in all other studied segments there is a good agreement between the topographic throw profile and the S-T value profile. The Nahf segment is a hard linked fault on its eastern end, and as expected, the along strike topographic and stratigraphic profiles are asymmetric. In contrast, the S-T profile, which is an outcome of erosion of the uplifted block, shows a symmetric profile (figs. 10 and 11). That is, the S-T is a result of the pre-hard-linked phase, and implies that the Nahf segment faulting history is comprised of two phases. In the first phase, while this segment was not physically linked to the neighboring segments, the slip rate was lower than the denudation rate so only stratigraphic throw accumulated along the segment, resulting in the formation of the symmetric S-T value profile. In the second phase, the segment slip rate must have increased to be higher than denudation in order to build the Nahf escarpment. The asymmetric triangle shape topographic throw profile of the Nahf segment, and the symmetric S-T value profile (figs. 10 and 11), suggesting that the second phase occurred close in time to the hard linkage. Moreover, it indicates that the increase in slip rate and the start of building the Nahf escarpment caused the denudation rate at the uplifted block to decrease dramatically, which causes the preservation of the symmetric S-T value profile. This observation agrees with Matmon et al., (2000b) observations on the Zurim escarpment and the other escarpments in the galilee, in which the increase in the faults slip rate and the initiation of the escarpments caused the denudation rate at the uplifted block to decrease dramatically. Hence, the question that arises is: what did cause the slip rate increase at the Nahf segment? The fault slip rates hardly change between the transition from soft to hard linkage between the segments, and only increase due to the link of the linked segments with a new fault segment, in which segments located at the center of the linked array will have the maximum increase in slip rate, while segments at the array tips will have the minimum increase in slip rate (Cowie & Roberts, 2001). Or the slip rate can change due to changes in the tectonic stress regime. Therefore, it implies that one of these two reasons is responsible for the slip increase in the Nahf segment: 1) The Nahf segment linked from its western tip to the Dier Al-Assad segment close in time to the transition from soft link to hard link at its eastern tip. 2) A Change in the tectonic stress regime caused the slip rate to increase at the Nahf segment. These changes occur close in time to the transition from soft link to hard link at the eastern tip of the Nahf segment. Based on the fact that the Bet Kerem fault system is a linked fault system. It seems to be that fault linkage is more likely

the reason for the increase in slip rate than tectonics. Moreover, In the next, we will see that there are correlations between segment linkage and the escarpment initiation.

5.3 The preservation of Senonian sediment in the relay ramps

At each of the downfaulted blocks (west to Peqi'in fault), the Senonian Menuha Formation is exposed, in contrast, at the uplifted blocks the Menuha Formation is only exposed at the relay ramps zones, and it eroded elsewhere (fig. 4). The relay ramp zone, which is today a part of the uplifted block, was before the fault interaction part of the downfaulted block (Cowie & Roberts, 2001; Peacock & Sanderson, 1994). That is, the increasing of the fault slip rates and the uplifting of the ramp zones didn't cause the erosion of the Menuha Formation, on the contrary, helped its preservation. Therefore, it implies that each of the fault segments history consists of faulting two phases as the Nahf segment. In which, the first phase the slip rate was lower than erosion therefore the Menuha Formation eroded from the uplifted blocks and preserved at the downfaulted blocks. While in the second phase the slip rate increased resulting in reducing the denudation rate at the uplifted blocks, which helped the preservation of the snapshot of the exposed stratigraphic sequences as it is before the start of the escarpment and preservation of the Menuha Formation on the uplifted relay ramps. Furthermore, it indicates all the fault segments (west to the Peki'in fault), were formed simultaneously when the Manhua formation was exposed everywhere in the study area. Otherwise, old faults will preserve a younger stratigraphic sequence than the Manhua formation at the downfaulted blocks and relay ramps and vice versa.

5.4 The spatial and the temporal development of BKFS

Since all the fault segments formed simultaneously, and the initiation age of the Zuriem escarpment gets younger westward form the system center (Rama and Sajur segments) (Matmon et al., 2000b, 2008). I suggest that the segments located close to the center of the system, Rama and Sajur, first increased their slip rate and initiation escarpments, and with time the increase in slip rates moved westward, and by that initiation of new escarpments westward. The S-T value profile, which is the thickness of the eroded stratigraphy sequences from the uplifted blocks, and mainly the outcome of the first faulting phase (before the escarpment initiation), shows a maximum value at the Sajur segment and then gradually decreases westward (fig. 16D). It indicates that at the first phase the slip rate of the Rama and Sajur was the highest and gradually decreased westward. Due to that, these two fault

segments have the highest lengthening rate, and by that, they have been able to start the linkage earlier than the western segments. This hypothesis is supported by observation at the S-T value profile of the Sajur segment, which is asymmetric as its topographic and stratigraphic profiles, and shows a maximum value close to its eastern termination (fig. 11A and 10B). This observation indicates that the Sajur segment was hard linked at its eastern end with the Rama segment before escarpment initiation (at first phase). On the western side of the Sajur segment, the hard link between Nahf and Sajur only affects the topographic and the stratigraphic throw profiles and indicates that the initiation of the escarpment occurred closely in time with hard link. Toward the west the segments are only soft linked. Therefore, it appears that the age of the fault's linkage increases eastward just like the escarpment initiation age, which indicates that fault linkage is responsible for the gradual westward increase in fault slip rates and not a result of a tectonic process. Because if it was a tectonic process, I would expect increases in the slip rates along all the fault segments and not a gradual and locally increasing.

Based on all of that, I provide the spatial and the temporal development of BKFS:

All the segments form simultaneously, the slip rate along the Sajur and Rama segments had to be higher (although lower than the denudation rate) than along the more western segments. This implies that the lengthening of the Sajur and Rama segments was the fastest and that the lengthening rate decreased westward (fig. 17A), and allowed the formation of a relatively early hard link between Rama and Sajur (during the first faulting phase) and the development of the asymmetric S-T value profile along the Sajur segment (fig. 17B). With time, the Rama and Sajur segments started to interact with Nahf segment, and a soft link developed, forming the Sajur ramp. This last link was followed by the increase of slip rate, such that relief started forming along the Rama and Sajur segments, and the buildup of the Zurim escarpment begun. At that time, the slip rate along the Nahf segment, which is located at the tip of the linked array, did not exceed the denudation rate (fig. 17C). Later, the Sajur ramp was breached, and a hard link between Sajur and Nahf formed, close to the time of the breaching an escarpment was initiated above the Nahf segment. The reason for the slip increase along the Nahf segment is probably the interaction with the Dier Al-Assad segment, which is manifested by the Nahf ramp (fig. 17D). Next, A soft link formed between the Dier Al-Assad segment and Majd Al-Krum segment and an escarpment initiated above the Dier Al-

Assad segment and an escarpment initiated above the Deir Al-Assad segment and so on until start forming an escarpment above the Ahihud segment (fig. 17E). In summary, the segments linkage migrated westward causing the escarpment initiation age to get younger westward.

.

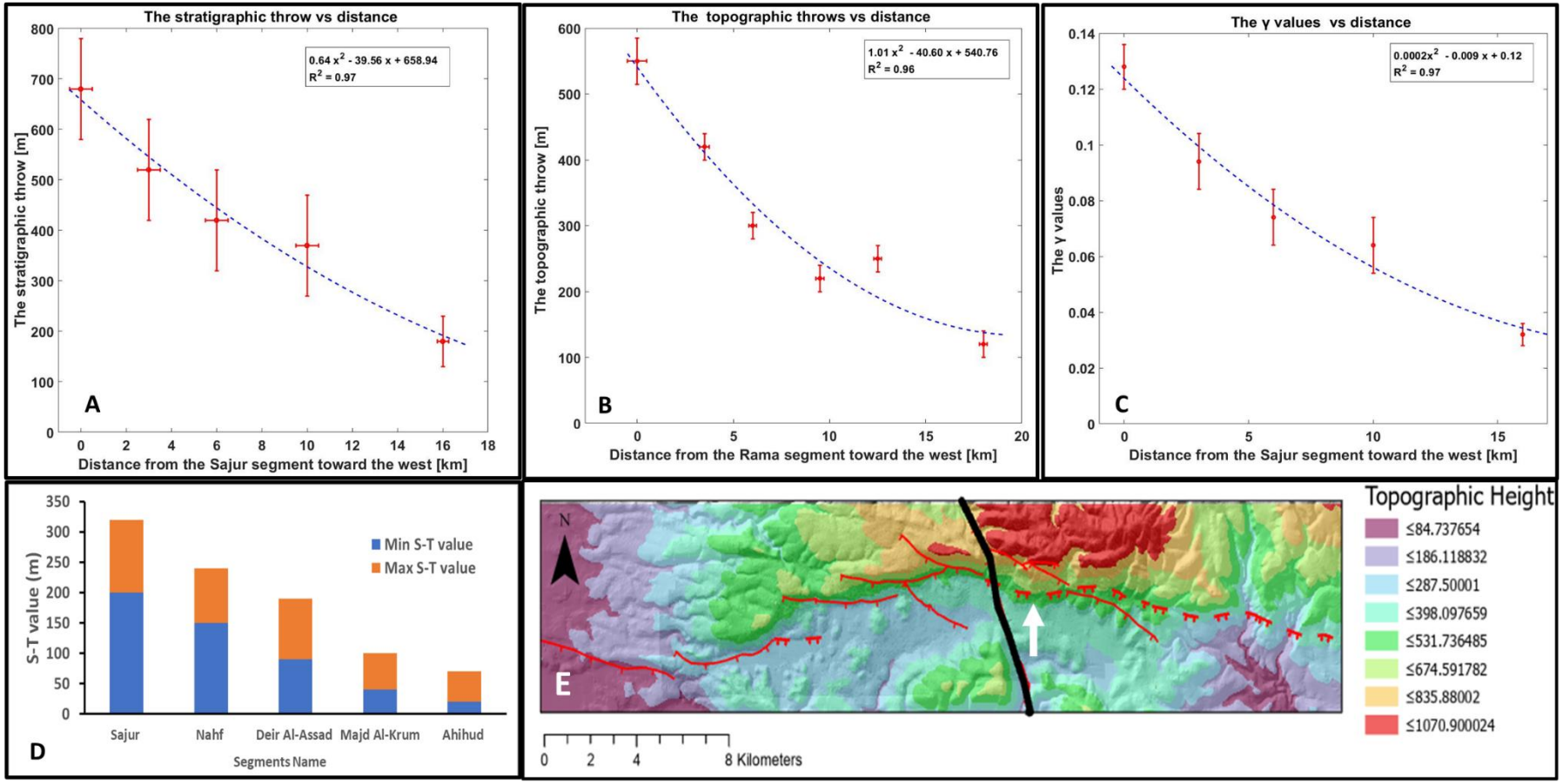

Figure. 16: The stratigraphic (A) and topographic (B) throw, and the γ value (c) as function of distance from the Sajur or Rama segment. As can be seen all values decrease westward in second-order polynomial regression, in agreement with the observation of Papanikolaou & Roberts, (2007) and Roberts & Michetti, (2004) on normal fault system in central Italy. (D) The maximum S-T value at each segment. The S-t value decreases westward. (E) Shaded relief map of the Bet Kerem valley and the Zurim Escarpment. Color-coded on the map are the topographic heights. The Bet Kerem fault system outlined by red lines, and Peqi'in fault by black line. The Rama segment (outlined by a white arrow) seems to be located in the center of BKFS since it has the highest topographic throw in the system.

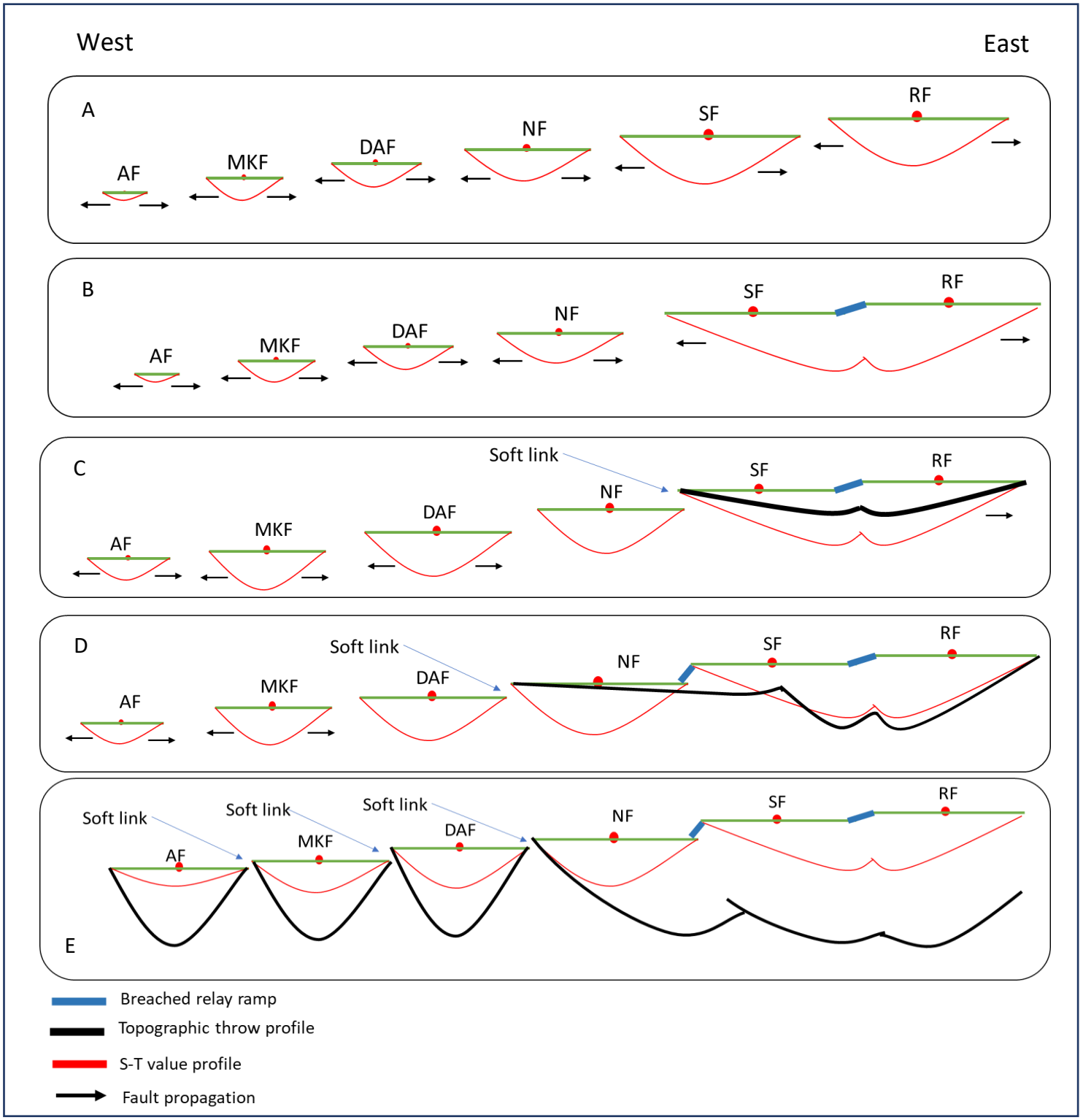

Figure. 17: The spatio-temporal evolution of the Bet-Kerem fault system following the rate-gradient scenario. (A) Normal faults were formed. Rama and Sajur, have a high slip rate, which decreased gradually westward. The maximum S-T value (the red line) also decreased gradually westward. (B) Rama and Sajur became hard linked faults and as a result asymmetric S-T value profiles were developed. (C) Soft-linkage developed between the Nahf fault and the already hard linked Rama and Sajur segments. This caused the initiation of an escarpment above Rama and Sajur, followed by the development of asymmetric topographic throw profiles (black line indicates the topographic throw profile). (D) Nahf and Sajur were hard linked. Nahf started to interact with Deir Al-Asad and a relay ramp zone formed between them. As result an escarpment developed above the Nahf fault. (E) All six segments are liked to form one continuous normal fault system.

5.5 ^{36}Cl results interpretation and discussion

5.5.1 Limitation of the ^{36}Cl method

Before we discuss the results, it is important to emphasis that due to the limitation of the ^{36}Cl approach, seismic events that generated < 25 cm of surface rupture, and with a recurrence interval of less than a few hundred years, cannot be detected. Therefore, the number of events indicated for each fault is a minimum number. Moreover, it implies that some so-called "event" may in fact be several earthquakes that occurred within a few hundreds of years or one single event that generated a large amount of surface slip (Schlagenhauf et al., 2010).

5.5.2 Surface rupturing history

I have identified 11 scarp exhumation events, at the Nahf East, Deir Al-Assad, and Sajur segments (table 6). The along strike scarp profiles of these segments (fig 12), are similar in shape to the along strike topographic throw profiles (fig. 10). This implies that the exhumation of the Sajur, Nahf East, and Deir Al-Assad scarps are caused by seismic events rather than an erosion (Iezzi et al., 2019; Isabelle Manighetti et al., 2005; Puliti et al., 2020). Therefore, the 11 scarp exhumation events represent surface rupturing events. The nine most recent events are identified along all there dated segments and indicate that they were active simultaneously during three distinct periods during the very latest Pleistocene and Holocene (12.0-11.0 kyr, 8.5 -7.0 kyr, 4.5 – 4.0 kyr) (fig .20 & table .6). Additionally, two older events or periods (29 ± 1 ka and 24.5 ± 0.5 ka) are identified only along the Deir Al-Assad segment. However, when considering the pre-exposure duration, which approximately represents the interseismic time before the oldest determined event, the Sajur and the Nahf East Faults indicate that the two faults were active simultaneously to the two older periods, just as during the Holocene. I hypothesize the reason that I can't detect these two periods at the Sajur, and the Nahf East Faults is because they generated surface rupture amount lower than the detection limit of the ^{36}Cl approach.

5.5.3 Earthquakes behavior

Empirical models that relate max surface rupture to rupture length, suggest that only 10 – 30 cm of surface offset should have occurred along the bet Kerem fault segments which are only ~5 km long (Wells and Coppersmith, 1994; fig. 18), and only 40 cm (Wesnousky, 2008).

However, ^{36}Cl Model results suggest three surface rupturing events of 1.2 m, 6.5 m and 2 m (table. 6) at the Nahf East segment. Considering the length of the segment, and a maximum surface offset of 30 cm during each earthquake, a minimum of 4 to 7 moderate earthquakes (Mw ~ 5) must have occurred in the first and last events, respectively, within a 1 kyr window. And for the second event, more than 20 moderate earthquakes (Mw ~ 5) are required to produce the observed offset. Similar results are given for the other two dated segments. This scenario, therefore, suggest swarms of moderate earthquakes that are recorded by the ^{36}Cl exposure dating method as a single event.

On the other hand, Well-documented seismic records show that only rarely is the surface ruptured along faults that are 4 – 6 km long. That is, if that is the case, the required number of earthquakes is greater than estimated before. Moreover, they show that surface rupturing events commonly produce as a result of large earthquakes that their occurrence requires a long fault segment or rupture of many short segments that together provide the required length (Bello et al., 2021; Bernard & Zollo, 1989; Iezzi et al., 2019; Isabelle Manighetti et al., 2005; Mozafari et al., 2019; Nicol et al., 2005; Soliva et al., 2008; Villani et al., 2018; Wells & Coppersmith, 1994). They also show that symmetric triangle shape surface rupturing is normally caused by a single fault rupture, while multi-segment rupture earthquakes cause asymmetric triangle shape surface rupturing profiles along the faults. Moreover, that the along-strike surface rupture distribution behaves as the along-strike scarp height distribution (Iezzi et al., 2019; Manighetti et al., 2005). i.e., if the carbonated fault scarp shows an asymmetric triangle shape profile the along-strike surface rupture profile will also show an asymmetric triangle shape profile. Therefore, the along-strike fault scarp can be used as an indication of the behavior of the past earthquakes.

Since the Bet Kerem fault system is a linked fault system, it behaves as one single fault. The rupture front that nucleates at one fault segment can propagate and rupture the adjacent fault segments, i.e., cause a multi-segment rupture earthquake. This scenario is consistent with the results of the ^{36}Cl model that indicate synchronized activity and the surface rupture amount. Moreover, the shape of the scrap profiles of the dated faults shows an asymmetrical triangle shape (fig. 12). Accordingly, it is seeming that the large earthquake scenario is earthquake behavior at the Bet Kerem fault system rather than the moderate earthquake scenario.

Fault name	**Nahf**	**Deir Al-Assad**	**Sajur**
Period 1	4.3 ± 0.5 ka 2 m	4.4 ± 0.5 ka 2.8 m	4.2 ± 0.5 ka 1.5m
Period 2	8.0 ± 0.5 ka 6.5m	7.5 ± 0.5 ka 2.4 m	7.5 ± 0.5 ka 2.5m
Period 3	11.8 ± 0.5 ka 1.2m	11.5 ± 0.5 ka 2.6 m	11.2 ± 0.5 ka 1.5 m
Period 4	----	24.5 ± 0.5 ka 1. 5 m	
Period 5	----	29 ± 1 ka 1. 6 m	
Pre exposure duration	$15.0^{+1.0}_{-1.5}\,ka$	$4.4^{+1.2}_{-1.0}\,ka$	$16.5^{+1.1}_{-1.3}\,ka$

Table. 6: Event ages and surface rupture amount at the three faults.

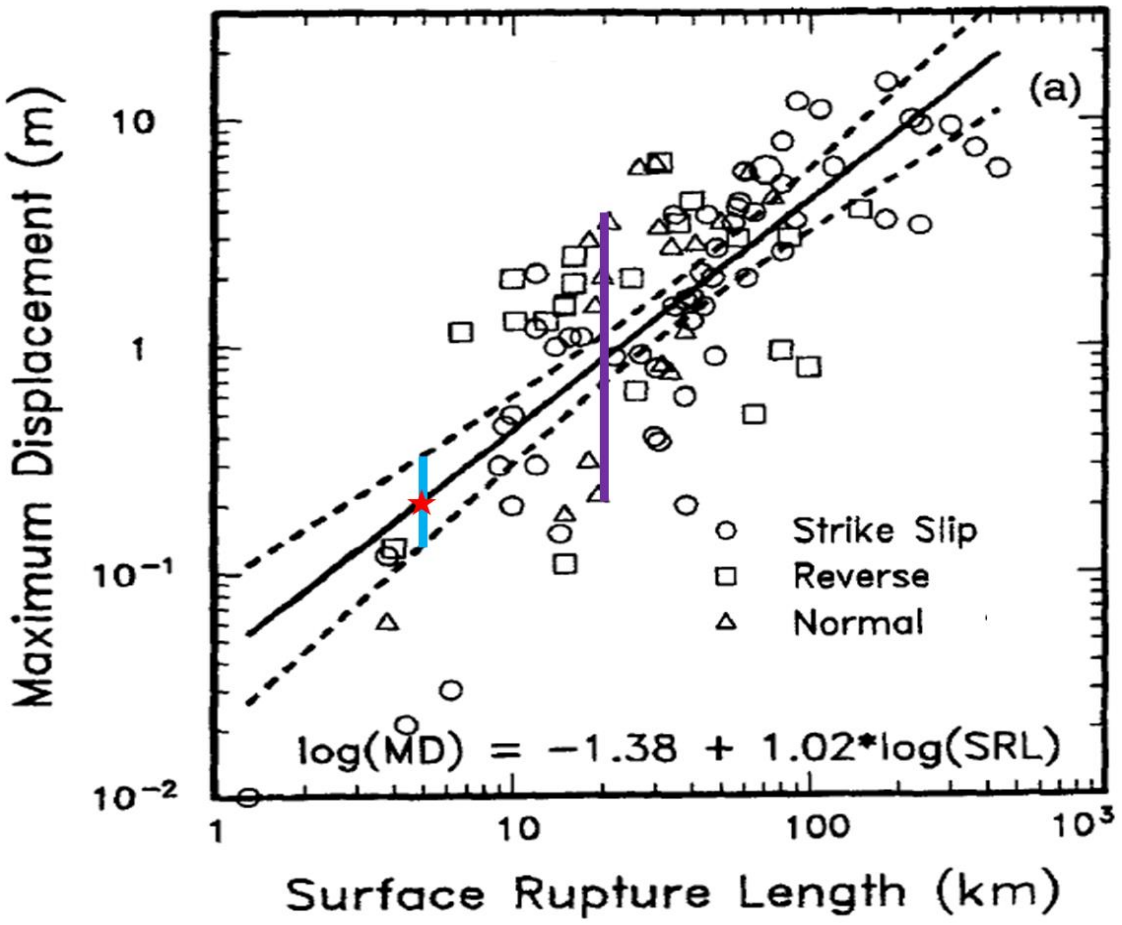

Figure. 18: The relation between surface rupture length (Km) and maximum surface slip (Wells & Coppersmith, 1994). The blue line indicates a fault length of ~ 5km, which is the length of the Bet Kerem dated segments. According to relation, the dated segments can generate only 10 – 30 cm of surface slip. The purple line indicates a fault length of ~ 20km, which includes all of the dated segments. At such a length, normal faults can generate 20 – 400 cm of surface slip.

5.5.4 Nahf fault

Based on my preferred scenario that multi-segment earthquakes are the common type of earthquakes along the BKFS, and that the BKFS behaves as one single fault, it is necessary that the Nahf segment, which was not dated, operated during the same activity periods as the three dated segments. This is based on the fact that: 1) The Nahf fault displays a fault scarp with observed slickensides at its base (fig. 19). 2) The propagation of rupture between the Dier El Assad, the Sajur, and Nahf east segments can only occur through the Nahef segment (fig. 4) (Bhat et al., 2007; Wesnousky, 2008). 3) The along-strike scarp profile shows two asymmetric triangle shapes that are separated by the Nahf East segment (fig. 12). Accordingly, the Nahf segment behaves seismically as two separate segments that have both been

ruptured by multi-segment earthquakes. Which may be the same events that ruptured the adjacent dated segments.

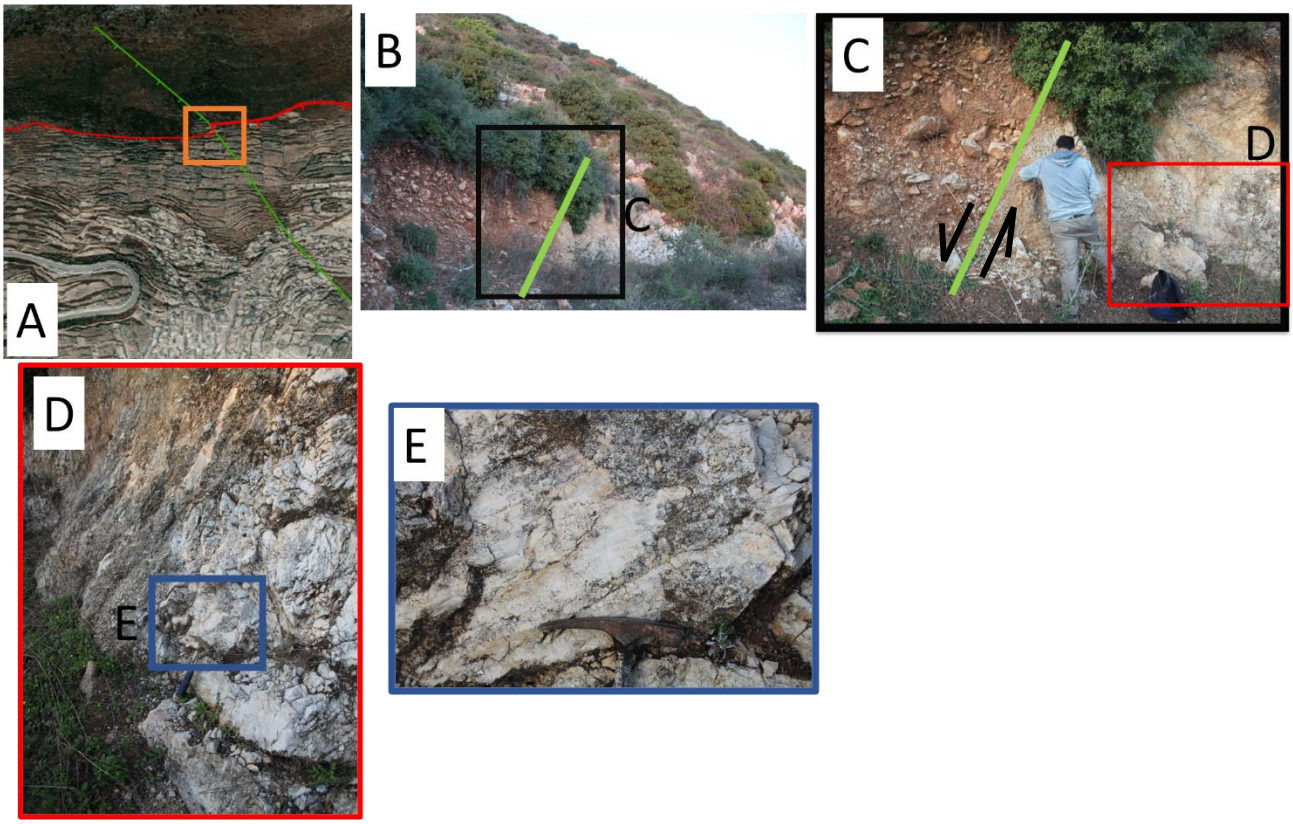

Figure. 19: The intersection between Nahf East Fault and Nahf Fault. (A) map view of the intersection: Nahf East Fault (green line) and Nahf Fault (red line). (B) Nahf fault scarp at the junction with Nahf East (green line), scarp height ~ 4m. (C) Zoom into the junction (black box in B). As can be seen the Nahf East fault offsets the Nahf fault, As result, the Nahf scarp is composed of a colluvial wedge where it is the down faulted block of Nahf East, and fault breccia in the up faulted block. (D) A closer look at Nahf fault scarp (breccia part) (red box in C). Sub horizontal slickenside are observed on the fault scarp (E)

5.5.5 Earthquake magnitude and recurrence interval

Due to the ^{36}Cl dating approach limitation, I can't determine the number of earthquakes that occurs at each activity period, nor the surface slip that generates by each earthquake, and by that the magnitude of the earthquakes. However, since the three dated segments were sampled where the faults show the maximum fault scarps height (Fig. 12), the sampling sites are located where the maximum surface slip at each of the activity periods occurred (Iezzi et al., 2019; Puliti et al., 2020). This maximum amount of surface slip with the length of the

surface rupture that was generated at each activity period can be used to estimate the maximum amount of surface slip during each earthquake, the number of earthquakes occurring at each period, and their magnitude. At the Bet Kerem fault system, Sajur, Nahf East, Deir Al-Assad, and Nahf are the only fault segments that display fault scarps that were exhumed seismically. Therefore, I assume that each earthquake that occurred during each of the activity period caused the rupture of the four segments, generating ~20 km of surface rupture. According to Wells and Coppersmith, (1994) and Wesnousky, (2008), a fault of such length can potentially cause maximum surface rupture of 1 m or 1.8 m, respectively.

Considering the total amount of offset during each period (table. 6) I estimate that 2-3 clustered earthquakes occurred during the 4 – 5 ka period, at least 4 clustered earthquakes occurred during the 7.0 – 8.5 ka period, 2-3 clustered earthquakes occurred during the 11 – 12 ka period, and at least 2 clustered earthquakes occurred during the 24 and 29 Ka periods. Within each activity period, earthquakes were clustered close enough (100's of years at the most) such that they cannot be distinguished using the ^{36}Cl exposure age dating. The recurrence interval of these earthquake clusters during the Holocene and late Pleistocene ranges from 3.5 to 5 ka years. In contrast, there is a ~ 13 kyr period of inactivity window on the Sajur, Nahef east and Deir Al-Assad segments prior to the Holocene activities (Fig 20 and 21). These results, therefore, point to three superimposed recurrence interval wavelengths on the Bet Kerem fault system:

1. A few 100's of years interval which separates between discrete earthquakes within a cluster.
2. A 3.5-5 ka interval between clusters, in which strain accumulated and released along the faults (fig. 20 and 21).
3. A 13-ka interval of total quiescence, in which strain only accumulated along the faults, and separated between earthquake clustering periods (fig. 20 and 21).

This phenomenon of the long quiescence period that the faults only accumulate strain, followed by a period during which the faults release all the accumulated strain (fig. 21) was observed by other paleoseismology studies (e.g., Friedrich et al., 2003; Marco et al., 1996; Rockwell et al., 2000; Schlagenhauf et al., 2011), and referred as the earthquake supercycle (Salditch et al., 2020). Thus, earthquakes within the Bet Kerem fault system follow the supercycle pattern.

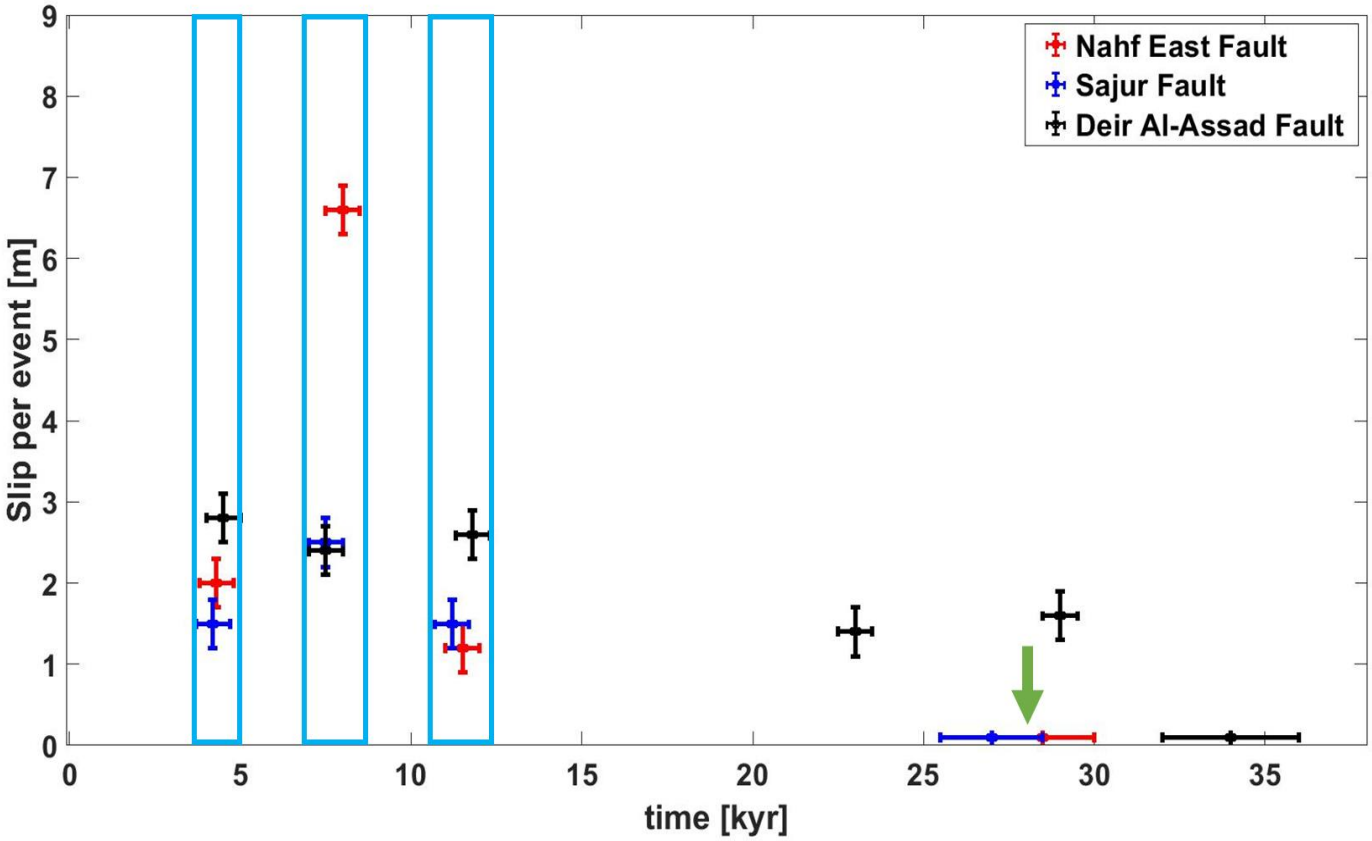

Figure. 20: Displacements per event versus time for the three dated segments. As can be seen there are three distinguished periods of synchronized surface rupturing activity (blue boxes). The pre-exposure duration of the Sajur and Nahf East faults (marked by the green arrow) indicates activity at the time of the early events along the Deir Al -Assad fault.

5.5.6 Slip versus time

Fault slip rates can be calculated as the total slip that is produced in a time frame divided by the time frame (Benedetti et al., 2013; Nicol et al., 2005; Scholz, 2019). For example, for the Nahf East fault, an offset of 9.7 m was produced in 22.5 kyr (the time frame starts from the pre-exposure duration added to the age of the oldest event and ends with a cluster at 4.3 kyr). As can be seen in table 7, in the last 30 kyr the Nahf East fault has the highest values, while the Sajur fault shows the lowest values.

Fault name	slip rate [mm/year]	Uplift rate [mm/year]
Sajur	0.23	0.22
Nahf East	0.44	0.35
Deir Al-Assad	0.38	0.34

Table. 7: Fault slip rates and uplift rates in mm/year for the last 30 kyr.

The estimated slip rate (table 7) can't be assumed to be constant since the earlier Pliocene. For one, if it was, the Zurim Escarpment should have been twice as high. Moreover, the long-term slip rate (since the earlier Pliocene) of the Zurim Escarpment and the other Galilee faults is 0.09 - 0.11 (Heimann et al., 1996; Matmon et al., 2000b, 2003; Sandler et al., 2004). Accordingly, the estimated slip rate for the last 30 kyr along the dated segments is two to four times higher. I can explain these relatively high slip rates:

[1] The estimated slip rates may overestimated. The overestimation can be a result of the high resolution for fast deformation. Especially, if the fault's activity patterns include short periods of intense activity alternating with long periods of tectonic quiescence as in the case of the dated faults (Matmon et al., 2010).

[2] Strain localization: In which strain is temporally localized on a few of the Galilee fault systems.

[3] Fault interaction: as a result of fault interaction, slip rate increases in proportion to the linked fault array length. As I showed previously, the Bet Kerem fault system is a linked fault system. Moreover, the length of the linked fault system increased over time. Consequently, the slip rate on the faults increased with time. The long-term slip rate, which is the average slip rate, is, therefore, lower than the estimated slip rate based on the fault scarps which represent the seismic activity of only the last several tens of thousands of years.

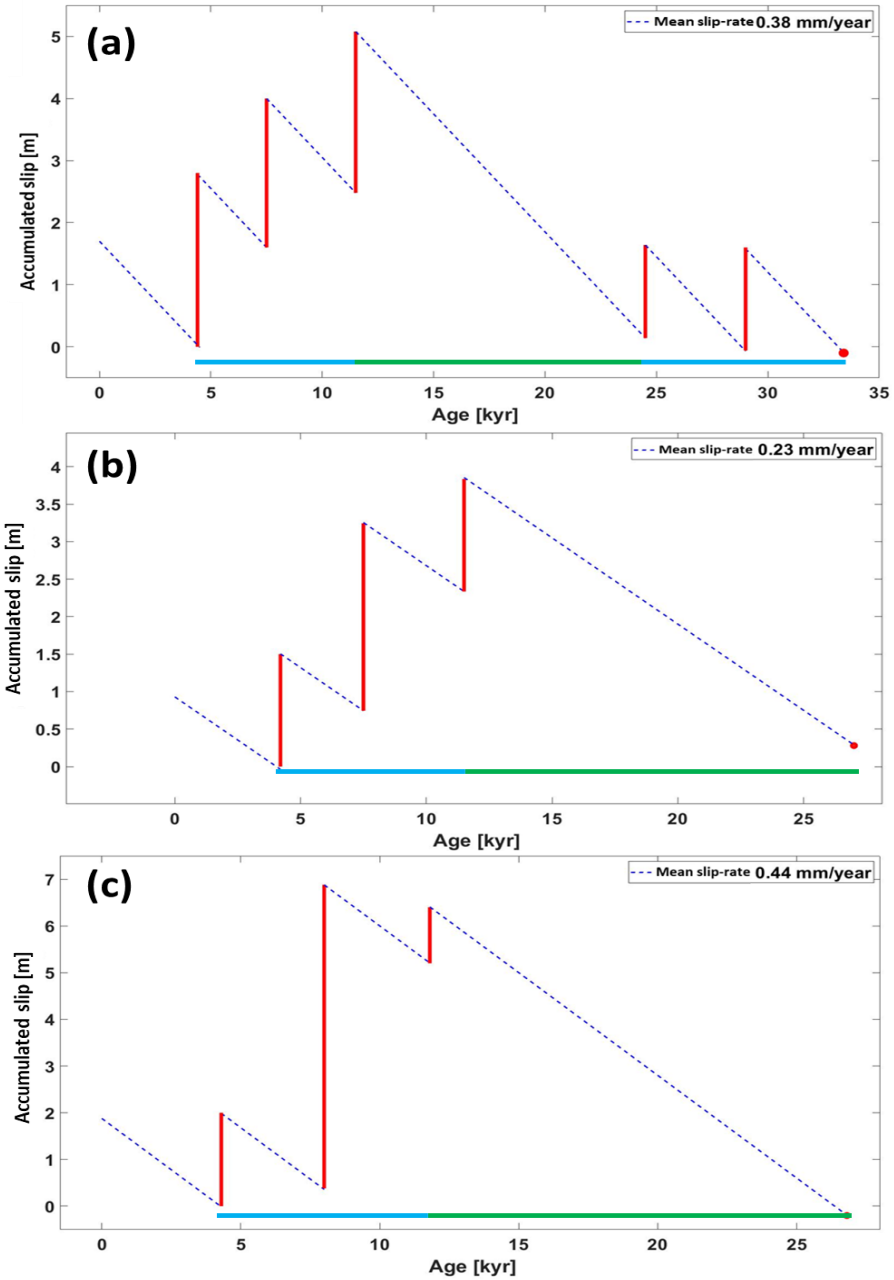

Figure 6: A schematic illustration of strain accumulation (blue dashed line) and release (red) over time. (a) Deir Al-Assad segment, (b) Nahf East segment, and (c) Sajur segment. As can be noticed there are two distinguished periods: strain accumulation period (in green), and strain accumulation and releasing period (in blue).

5.5.7 Relations with Historical Events at the Bet Kerem Valley

Two significant shaking events that occurred in the Bet-Kerem valley surroundings can been seen in the archeological record. The ages of these events are consistent with the ages of surface rupture, revealed by ^{36}Cl. The first event occurred during the late Pleistocene (12.5 – 11.5 kyr), in which large boulders that were detached from the ceiling of the HaYonim Cave (fig. 22) are included in the archeological sequence. Cave debris and speleothems collapse have been observed in the Peki'in cave. This collapse was caused by a strong shaking event that could be a result of a seismic event and constrained by the U-Th dating method to 7.5 and 6.5 kyr (fig. 22) (M. Bar-Matthews, personal communication, 2022). Furthermore, a castle near Kibbutz Kabri, ~ 16 km northwest to the Bet Kerem fault system, has been damaged by strong shaking. This shaking has been interpreted as seismic event with age of 3.8 - 3.7 kyr (fig. 22) (Lazar et al., 2020). The age of the shaking event fits well with the age of the youngest recovered surface rupturing event. However, this strong shaking at the Kabri castle can be generated also by earthquakes along the Dead Sea Transform rather than the Bet Kerem Fault System, and it may be not seismic at all. These are also valid for the other two shaking events near the Bet Kerem fault system. But the temporal correlation between seismic events and collapse and the damage events raises always the possibility that these earthquakes are the reason for the damage rather than It is just a coincidence.

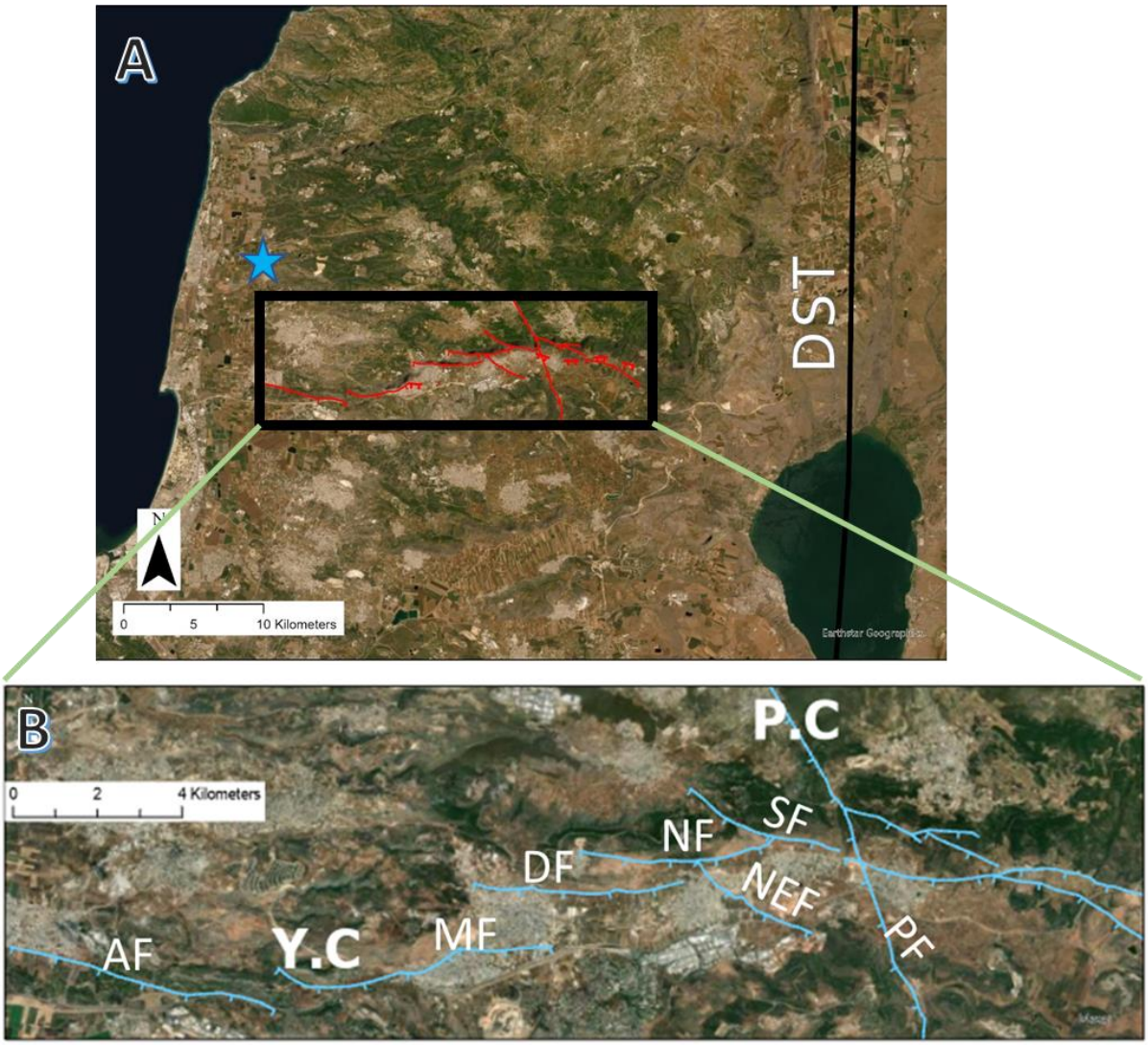

Figure. 22: (A) The location of the Kabri castle (blue star) relative to Bet-Kerem fault system red. DST = Dead Sea Transform. (B) The location of the HaYonim Cave (Y.C) and Peki'in cave (P.C) relative to Bet-Kerem fault system in blue. Faults names: RF = Rama fault, SF= Sajur fault, NF = Nahf fault, DF = Deir Al-Assad fault, MF = Majd Al-Krum fault, and AF = Ahihud fault), intersecting with the Nahef east fault (in black).

5.5.8 Relations with Historical Events along the Dead Sea Transform

A cluster of earthquakes was recorded along the Dead Sea Transform and its branching Camel Fault at 4 - 5 kyr ago. This time frame is consistent with the age of the last earthquake cluster along the Bet Kerem fault system (fig. 24) (Braun et al., 2009; Gluck, 2001; Katz et al., 2009; Matmon et al., 2006; Rinat et al., 2014). Moreover, there is one more seismic event that was recorded along the Carmel fault with an age of 10.4±0.7 kyr (fig. 24) (Braun et al., 2009). This age is consistent with the age of the cluster that produced the surface rupture at 11-12 kyr. Further observations come from the eastern shore of the Sea of Galilee (fig. 24): in addition

to the 4-5 kyr event, there are 4 additional events, the youngest of them occurred at 9.2 ±1.9 kyr and which can be consistent with the second surface rupturing event or with the third. The other three events were dated between 30 - 40 kyr (Katz et al., 2009). This period of high seismic activity can be consistent with the oldest dated surface rupturing event at Deir Al-Assad fault segment. Combined, all these observations suggest that earthquakes along the Dead Sea Transform and its branches may cause trigger seismic activity along the Bet Kerem fault system and versa vice (Scholz, 2010, 2019).

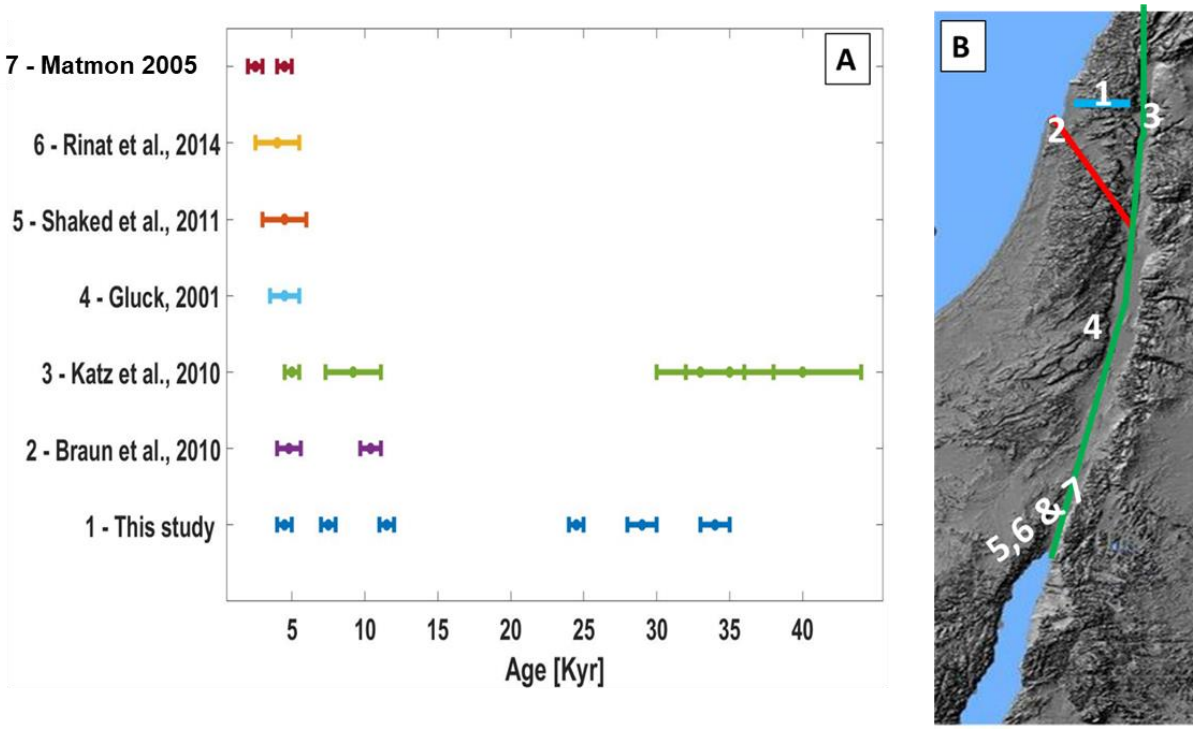

Figure. 23: (A) Evidence of seismic events from paleoseismic records along the Dead Sea Transform and the Camel fault. Blue points outline the seismic activity along the Bet-Kerem fault system. As can be seen, some of the events at the Bet-Kerem fault system are synchronized with events along the Dead Sea Transform and the Camel fault. (B) Digital shielded relief (Hall, 1993) with locations of sites mentioned in (A). The green line indicates the Dead Sea Transform, the red line indicates the Carmel fault, and the blue line indicates the Bet-Kerem fault system.

6. Conclusion

Conclusion

Faults linkage and landscape

The history of the segments of the Bet Kerem fault system consists of two phases. During the first phase the slip rate was slower than the erosion rate, therefore topographic expression didn't form, and only stratigraphic throw accumulated along each segment. In the second phase, the slip rate increased. Stratigraphic offset continued to accumulate accompanied by the development of topography. The reason for slip rate increase is related to fault linkage. This conclusion is based on the spatial and temporal correlations between segment linkage and the escarpment initiation. Therefore, the fault linkage process played a significant role in landscape evolution at Galilee along the Zurim Escarpment.

Faults linkage and Earthquakes

The Bet Kerem fault system is a linked fault system. Because to that, a rupture front caused by an earthquake on one fault segment can propagate to adjacent segments and rupture them. This propagation results in large earthquakes and the occurrence of large surface slips, which are consistent with the synchronized activity of the segments and the surface rupture amount obtained by the ^{36}Cl model results. The Bet Kerem Faults system case indicates that multi-segment rupture earthquakes should be considered in paleoseismological studies that show occurrences of large surface slips along relatively short fault segments.

Earthquakes at the Bet Kerem fault system

Five surface rupturing period are observed on the dated faults. Based on the surface rupture amount and the synchronized activity at each of the activity periods as well as the scarp profile shape of the dated faults, I interpret that each activity period consists of a cluster of at least two large earthquakes (Mw > 6), and each of the earthquakes has generated ~ 20 km of surface rupturing.

Earthquakes within the Bet Kerem fault follow the earthquake supercycle pattern and show three recurrence interval cycles:

1. A <1000 interval which separates between discrete earthquakes, within the activity period.
2. A 3.5-5 ka interval between clusters, within the cluster activity period.
3. A 13-ka of total quiescence between the activity period.

Implications on seismic hazard assessment

Our results contribute to earthquake hazard assessment in the Galilee region, northern Israel. I show that the large surface rupture observed at the Bet Kerem fault system is produced by large earthquakes that ruptured multi-fault segments. This is enabled because the segments are connected (either at the surface or at sub surface). Therefore, I suggest considering the surface/sub surface connection between segments. Multi- segment resurface rupture has implications in estimating the earthquake's magnitude, surface rupture length, and the max surface slip that can be generated. All of these parameters play a main role in seismic hazard assessment (McCalpin, 2009).

The last earthquake cluster at the Bet Kerem fault system occurred ~ 4.5 kyr ago, which is within the range of the calculated Holocene to late Pleistocene recurrence interval between earthquake clusters. On one hand, it seems that a cluster should occur in the near future. On the other hand, in the most recent cluster, the faults released all the accumulated strain (Figure 21). Therefore, the faults entered the long quiescence period (which is ~13 ka long), which means that the next cluster will occur after ~ 8 kyr. As long as we can't determine whether the supercycle behavior (~13 ka long of total quiescence between the activity period) is typical or an anomaly my best guess is that the next cluster will occur within the next 8 kyr.

7.References

Akaike, H. (1974). A New Look at the Statistical Model Identification. *IEEE Transactions on Automatic Control*, *19*(6). https://doi.org/10.1109/TAC.1974.1100705

Ambraseys, N. (2015). Earthquakes in the mediterranean and middle east: A multidisciplinary study of seismicity up to 1900. In *Earthquakes in the Mediterranean and Middle East: A Multidisciplinary Study of Seismicity Up to 1900*. Cambridge University Press. https://doi.org/10.1017/CBO9781139195430

Bachmann, M., & Hirsch, F. (2006). Lower Cretaceous carbonate platform of the eastern Levant (Galilee and the Golan Heights): stratigraphy and second-order sea-level change. *Cretaceous Research*, *27*(4), 487–512.

Bartholomew, R. M., Boyd, A. W., Brown, F., Hawkings, R. C., Lounsbury, M., & Merritt, W. F. (1955). THE HALF-LIFE OF Cl36. *Https://Doi.Org/10.1139/P55-007*, *33*(2), 43–48. https://doi.org/10.1139/P55-007

Bello, S., Scott, C. P., Ferrarini, F., Brozzetti, F., Scott, T., Cirillo, D., de Nardis, R., Arrowsmith, J. R., & Lavecchia, G. (2021). High-resolution surface faulting from the 1983 Idaho Lost River Fault Mw 6.9 earthquake and previous events. *Scientific Data*, *8*(1). https://doi.org/10.1038/s41597-021-00838-6

Benedetti, L., Finkel, R., Papanastassiou, D., King, G., Armijo, R., Ryerson, F., Farber, D., & Flerit, F. (2002). Post-glacial slip history of the Sparta fault (Greece) determined by 36Cl cosmogenic dating: Evidence for non-periodic earthquakes. *Geophysical Research Letters*, *29*(8), 87–1. https://doi.org/10.1029/2001gl014510

Benedetti, L., Manighetti, I., Gaudemer, Y., Finkel, R., Malavieille, J., Pou, K., Arnold, M., Aumaître, G., Bourlès, D., & Keddadouche, K. (2013). Earthquake synchrony and clustering on Fucino faults (Central Italy) as revealed from in situ 36Cl exposure dating. *Journal of Geophysical Research: Solid Earth*, *118*(9). https://doi.org/10.1002/jgrb.50299

Bernard, P., & Zollo, A. (1989). The Irpinia (Italy) 1980 earthquake: Detailed analysis of a complex normal faulting. *Journal of Geophysical Research: Solid Earth*, *94*(B2), 1631–1647. https://doi.org/10.1029/JB094IB02P01631

Bhat, H. S., Olives, M., Dmowska, R., & Rice, J. R. (2007). Role of fault branches in earthquake rupture dynamics. *Journal of Geophysical Research: Solid Earth*, *112*(11). https://doi.org/10.1029/2007JB005027

Bierman, P. R. (1994). Using in situ produced cosmogenic isotopes to estimate rates of landscape evolution: a review from the geomorphic perspective. *Journal of Geophysical Research*, *99*(B7). https://doi.org/10.1029/94JB00459

Bogoch, R., & Sneh, A. (2008). *The 1:50,000 geological map of Arbel sheet*.

Braun, Y., Kagan, E., Bar-Matthews, M., Ayalon, A., & Agnon, A. (2009). Dating speleoseismites near the Dead Sea Transform and the Carmel fault: Clues to coupling of a plate boundary and its branch. *Israel Journal of Earth Sciences*, *58*(3–4). https://doi.org/10.1560/IJES.58.3-4.257

Cowie, P. (1998). A healing–reloading feedback control on the growth rate of seismogenic faults. *Journal of Structural Geology*, *20*(8), 1075–1087. https://doi.org/10.1016/S0191-8141(98)00034-0

Cowie, P., Attal, M., Tucker, G. E., Whittaker, A. C., Naylor, M., Ganas, A., & Roberts, G. P. (2006). Investigating the surface process response to fault interaction and linkage using a numerical modelling approach. *Basin Research*, *18*(3), 231–266. https://doi.org/10.1111/J.1365-2117.2006.00298.X

Cowie, P., Gupta, S., & Dawers, N. H. (2000). Implications of fault array evolution for synrift depocentre development: Insights from a numerical fault growth model. *Basin Research*, *12*(3–4). https://doi.org/10.1111/j.1365-2117.2000.00126.x

Cowie, P., Phillips, R., Roberts, G., McCaffrey, K., Zijerveld, L., Gregory, L., Faure Walker, J., Wedmore, L., Dunai, T., Binnie, S., Freeman, S., Wilcken, K., Shanks, R., Huismans, R., Papanikolaou, I., Michetti, A., & Wilkinson, M. (2017). Orogen-scale uplift in the central Italian Apennines drives episodic behaviour of earthquake faults. *Scientific Reports*, *7*. https://doi.org/10.1038/srep44858

Cowie, P., & Roberts, G. P. (2001). Constraining slip rates and spacings for active normal faults. *Journal of Structural Geology*, *23*(12), 1901–1915. https://doi.org/10.1016/S0191-8141(01)00036-0

Cowie, P., & Scholz, C. H. (1992a). Growth of faults by accumulation of seismic slip. *Journal of Geophysical Research: Solid Earth*, *97*(B7), 11085–11095. https://doi.org/10.1029/92JB00586

Cowie, P., & Scholz, C. H. (1992b). Physical explanation for the displacement-length relationship of faults using a post-yield fracture mechanics model. *Journal of Structural Geology*, *14*(10), 1133–1148. https://doi.org/10.1016/0191-8141(92)90065-5

Freund, R. (1959). On the stratigraphy and tectonics of the upper cretaceous in western Galilee. *Bull. Res. Counc. of Israel*, *G8*, 43–50.

Freund, R. (1970). The geometry of faulting in the Galilee. *Israel Journal of Earth Sciences*, *19*(3–4), 117.

Friedrich, A. M., Wernicke, B. P., Niemi, N. A., Bennett, R. A., & Davis, J. L. (2003). Comparison of geodetic and geologic data from the Wasatch region, Utah, and implications for the spectral character of Earth deformation at periods of 10 to 10 million years. *Journal of Geophysical Research: Solid Earth*, *108*(B4). https://doi.org/10.1029/2001JB000682

Gluck, D. (2001). *The landscape evolution of the southwestern Dead Sea basin and the paleoseismic record of the southwestern marginal fault of the Dead Seabasin and the Carmel fault during the late Pleistocene and the Holocene*. https://www.gov.il/en/departments/publications/reports/gluck-report-2002

Golani, U. (1961). On the Cenomanian-Turonian lithostratigraphy of central Galilee. *Bulletin of the Research Council of Israel*, *10G*(1–2), 120–146.

Gosse, J. C., & Phillips, F. M. (2001). Terrestrial in situ cosmogenic nuclides: Theory and application. *Quaternary Science Reviews*, *20*(14), 1475–1560. https://doi.org/10.1016/S0277-3791(00)00171-2

Guidobon, M., & Stucchi, E. (1993). The contribution of historical records of earthquakes to the evaluation of seismic hazard. *Annals of Geophysics*, *36*(3–4). https://doi.org/10.4401/ag-4264

Heimann, A., Steinitz, G., Mor, D., & Shaliv, G. (1996). The Cover Basalt Formation, its age and its regional and tectonic setting: Implications from K-Ar and 40Ar/39Ar geochronology. *Israel Journal of Earth Sciences*, *45*(2).

Iezzi, F., Roberts, G., Walker, J. F., & Papanikolaou, I. (2019). Occurrence of partial and total coseismic ruptures of segmented normal fault systems: Insights from the Central Apennines, Italy. *Journal of Structural Geology*, *126*, 83–99. https://doi.org/10.1016/J.JSG.2019.05.003

Katz, O., Amit, R., Yagoda-Biran, G., Hatzor, Y. H., Porat, N., & Medvedev, B. (2009). Quaternary earthquakes and landslides in the Sea of Galilee area, the Dead Sea Transform: Paleoseismic analysis and implication

to the current hazard. *Israel Journal of Earth Sciences*, *58*(3–4). https://doi.org/10.1560/IJES.58.3-4.275

Lal, D. (1991). Cosmic ray labeling of erosion surfaces: in situ nuclide production rates and erosion models. *Earth and Planetary Science Letters*, *104*(2–4), 424–439. https://doi.org/10.1016/0012-821X(91)90220-C

Lazar, M., Cline, E. H., Nickelsberg, R., Shahack-Gross, R., & Yasur-Landau, A. (2020). Earthquake damage as a catalyst to abandonment of a Middle Bronze Age settlement: Tel Kabri, Israel. *PLoS ONE*, *15*(9 September). https://doi.org/10.1371/journal.pone.0239079

Manighetti, I., King, G. C. P., Gaudemer, Y., Scholz, C. H., & Doubre, C. (2001). Slip accumulation and lateral propagation of active normal faults in Afar. *Journal of Geophysical Research: Solid Earth*, *106*(B7), 13667–13696. https://doi.org/10.1029/2000JB900471

Manighetti, Isabelle, Campillo, M., Sammis, C., Mai, P. M., & King, G. (2005). Evidence for self-similar, triangular slip distributions on earthquakes: Implications for earthquake and fault mechanics. In *Journal of Geophysical Research: Solid Earth* (Vol. 110, Issue 5). https://doi.org/10.1029/2004JB003174

Marco, S. (2008). Recognition of earthquake-related damage in archaeological sites: Examples from the Dead Sea fault zone. *Tectonophysics*, *453*(1–4), 148–156. https://doi.org/10.1016/j.tecto.2007.04.011

Marco, S., Stein, M., Agnon, A., & Ron, H. (1996). Long-term earthquake clustering: A 50,000-year paleoseismic record in the Dead Sea Graben. *Journal of Geophysical Research B: Solid Earth*, *101*(3), 6179–6191. https://doi.org/10.1029/95jb01587

Matmon, A., Enzel, Y., Zilberman, E., & Heimann, A. (1999). Late Pliocene and Pleistocene reversal of drainage systems in northern Israel: tectonic implications. *Geomorphology*, *28*(1–2), 43–59. https://doi.org/10.1016/S0169-555X(98)00097-X

Matmon, A., Katz, O., Siman-Tov, S., Agnon, A., & Sha'ar, R. (2008). Geomorphology and Tectonics along the Zurim escarpment. *Field Trips Guide, Israel Geological Society Annual Meeting*.

Matmon, A., Shaked, Y., Porat, N., Enzel, Y., Finkel, R., Lifton, N., Boaretto, E., & Agnon, A. (2006). Corrigendum to "Landscape development in an hyperarid sandstone environment along the margins of the Dead Sea fault: Implications from dated rock falls" [Earth Planet. Sci. Lett. 240 (2005) 803-817] (DOI:10.1016/j.epsl.2005.06.059). In *Earth and Planetary Science Letters* (Vol. 245, Issues 1–2). https://doi.org/10.1016/j.epsl.2006.03.013

Matmon, A., Wdowinski, S., & Hall, J. K. (2003). Morphological and structural relations in the Galilee extensional domain, northern Israel. *Tectonophysics*, *371*(1–4), 223–241.

Matmon, A., Zilberman, E., & Enzel, Y. (2000a). Development of the Bet ha'Emeq structure and the tectonic activity of normal faults in the Galilee. *Israel Journal of Earth Sciences*, *49*(3). https://doi.org/10.1560/K5GH-3TAC-GGKY-C0Q8

Matmon, A., Zilberman, E., & Enzel, Y. (2000b). Determination of escarpment age using morphologic analysis: An example from the Galilee, northern Israel. In *GSA Bulletin* (Vol. 112, Issue 12). GeoScienceWorld. https://doi.org/10.1130/0016-7606(2000)112<1864:DOEAUM>2.0.CO;2

McLeod, A. E., Dawers, N. H., & Underhill, J. R. (2000). The propagation and linkage of normal faults: Insights from the Strathspey-Brent-Stafjord fault array, Northern North Sea. *Basin Research*, *12*(3–4), 263–284. https://doi.org/10.1111/J.1365-2117.2000.00124.X

Medina-Cascales, I., García-Tortosa, F. J., Martin-Rojas, I., Pérez-Peña, J. V., & Alfaro, P. (2021). Tectonic geomorphology of an active slow-moving, intrabasinal fault: The Galera Fault (Guadix-Baza Basin, central Betic Cordillera, southern Spain). *Geomorphology*, *393*. https://doi.org/10.1016/j.geomorph.2021.107941

Migowski, C., Agnon, A., Bookman, R., Negendank, J. F. W., & Stein, M. (2004). Recurrence pattern of Holocene earthquakes along the Dead Sea transform revealed by varve-counting and radiocarbon dating of lacustrine sediments. *Earth and Planetary Science Letters*, *222*(1), 301–314. https://doi.org/10.1016/J.EPSL.2004.02.015

Mitchell, S. G., Matmon, A., Bierman, P. R., Enzel, Y., Caffee, M., & Rizzo, D. (2001). Displacement history of a limestone normal fault scarp, northern Israel, from cosmogenic 36Cl. *Journal of Geophysical Research: Solid Earth*, *106*(B3), 4247–4264. https://doi.org/10.1029/2000jb900373

Mozafari, N., Glar Özkaymak, Ç. ˇ, Tikhomirov, D., Ivy-Ochs, S., Alfimov, V., Sözbilir, H., Schlüchter, C., Akçar, N., & Martinez-Frias, J. (2021). Seismic Activity of the Manisa Fault Zone in Western Turkey Constrained by Cosmogenic 36Cl Dating. *Geosciences 2021, Vol. 11, Page 451*, *11*(11), 451. https://doi.org/10.3390/GEOSCIENCES11110451

Mozafari, N., Tikhomirov, D., Sumer, Ö., Özkaymak, Ç., Uzel, B., Yeşilyurt, S., Ivy-Ochs, S., Vockenhuber, C., Sözbilir, H., & Akçar, N. (2019). Dating of active normal fault scarps in the Büyük Menderes Graben (western Anatolia) and its implications for seismic history. *Quaternary Science Reviews*, *220*, 111–123. https://doi.org/10.1016/j.quascirev.2019.07.002

Nicol, A., Walsh, J. J., Manzocchi, T., & Morewood, N. (2005). Displacement rates and average earthquake recurrence intervals on normal faults. *Journal of Structural Geology*, *27*(3). https://doi.org/10.1016/j.jsg.2004.10.009

Nicol, A., Walsh, J. J., Villamor, P., Seebeck, H., & Berryman, K. R. (2010). Normal fault interactions, paleoearthquakes and growth in an active rift. *Journal of Structural Geology*, *32*(8), 1101–1113. https://doi.org/10.1016/J.JSG.2010.06.018

Nicol, A., Watterson, J., Walsh, J. J., & Childs, C. (1996). The shapes, major axis orientations and displacement patterns of fault surfaces. *Journal of Structural Geology*, *18*(2–3), 235–248. https://doi.org/10.1016/S0191-8141(96)80047-2

Papanikolaou, I. D., & Roberts, G. P. (2007). Geometry, kinematics and deformation rates along the active normal fault system in the southern Apennines: Implications for fault growth. *Journal of Structural Geology*, *29*(1), 166–188. https://doi.org/10.1016/J.JSG.2006.07.009

Peacock, D. C. P., & Sanderson, D. J. (1991). Displacements, segment linkage and relay ramps in normal fault zones. *Journal of Structural Geology*, *13*(6), 721–733. https://doi.org/10.1016/0191-8141(91)90033-F

Peacock, D. C. P., & Sanderson, D. J. (1994). Geometry and Development of Relay Ramps in Normal Fault Systems. *AAPG Bulletin*, *78*(2), 147–165. https://doi.org/10.1306/BDFF9046-1718-11D7-8645000102C1865D

Puliti, I., Pizzi, A., Benedetti, L., Di Domenica, A., & Fleury, J. (2020). Comparing Slip Distribution of an Active Fault System at Various Timescales: Insights for the Evolution of the Mt. Vettore-Mt. Bove Fault System

in Central Apennines. *Tectonics*, *39*(9), e2020TC006200. https://doi.org/10.1029/2020TC006200

Reches, Z., & Hoexter, D. F. (1981). Holocene seismic and tectonic activity in the Dead Sea area. *Tectonophysics*, *80*(1–4), 235–254. https://doi.org/10.1016/0040-1951(81)90151-7

Rinat, Y., Matmon, A., Arnold, M., Aumaître, G., Bourlès, D., Keddadouche, K., Porat, N., Morin, E., & Finkel, R. C. (2014). Holocene rockfalls in the southern Negev Desert, Israel and their relation to Dead Sea fault earthquakes. *Quaternary Research (United States)*, *81*(2). https://doi.org/10.1016/j.yqres.2013.12.008

Roberts, G. P., & Michetti, A. M. (2004). Spatial and temporal variations in growth rates along active normal fault systems: an example from The Lazio–Abruzzo Apennines, central Italy. *Journal of Structural Geology*, *26*(2), 339–376. https://doi.org/10.1016/S0191-8141(03)00103-2

Rockwell, T. K., & Ben-Zion, Y. (2007). High localization of primary slip zones in large earthquakes from paleoseismic trenches: Observations and implications for earthquake physics. *Journal of Geophysical Research*, *112*(B10), B10304. https://doi.org/10.1029/2006JB004764

Rockwell, T. K., Lindvall, S., Herzberg, M., Murbach, D., Dawson, T., & Berger, G. (2000). Paleoseismology of the Johnson Valley, Kickapoo, and Homestead Valley faults: Clustering of earthquakes in the Eastern California shear zone. *Bulletin of the Seismological Society of America*, *90*(5), 1200–1236. https://doi.org/10.1785/0119990023

Ron, H., & Eyal, Y. (1985). Intraplate deformation by block rotation and mesostructures along the Dead Sea Transform, northern Israel. *Tectonics*, *4*(1), 85–105. https://doi.org/10.1029/TC004i001p00085

Rotevatn, A., Jackson, C. A. L., Tvedt, A. B. M., Bell, R. E., & Blækkan, I. (2019). How do normal faults grow? *Journal of Structural Geology*, *125*, 174–184. https://doi.org/10.1016/J.JSG.2018.08.005

Sagy, A., Sneh, A., Rosensaft, M., & Bartov, Y. (2013). *Map of "Active" and "Potentially Active" Faults that Rupture the Surface in Israel. Updates 2013 for Israel Standard 413: Definitions, comments and clarifications, GSI/02/2013 (In Hebrew).*

Salditch, L., Stein, S., Neely, J., Spencer, B. D., Brooks, E. M., Agnon, A., & Liu, M. (2020). Earthquake supercycles and Long-Term Fault Memory. In *Tectonophysics* (Vol. 774, p. 228289). Elsevier B.V. https://doi.org/10.1016/j.tecto.2019.228289

Sandler, A., Harlavan, Y., & Shaliv, G. (2004). The stratigraphy of Neogene conglomerates in the Yizre'el Valley. *Israel Journal of Earth Sciences*, *53*(2). https://doi.org/10.1560/A1UH-UEW1-XGA9-6CX3

Schimmelpfennig, I., Benedetti, L., Finkel, R., Pik, R., Blard, P. H., Bourlès, D., Burnard, P., & Williams, A. (2009). Sources of in-situ 36Cl in basaltic rocks. Implications for calibration of production rates. *Quaternary Geochronology*, *4*(6), 441–461. https://doi.org/10.1016/j.quageo.2009.06.003

Schlagenhauf, A., Gaudemer, Y., Benedetti, L., Manighetti, I., Palumbo, L., Schimmelpfennig, I., Finkel, R., & Pou, K. (2010). Using in situ Chlorine-36 cosmonuclide to recover past earthquake histories on limestone normal fault scarps: a reappraisal of methodology and interpretations. *Geophysical Journal International*, *182*(1), no-no. https://doi.org/10.1111/j.1365-246X.2010.04622.x

Schlagenhauf, A., Manighetti, I., Benedetti, L., Gaudemer, Y., Finkel, R., Malavieille, J., & Pou, K. (2011). Earthquake supercycles in Central Italy, inferred from 36Cl exposure dating. *Earth and Planetary Science Letters*, *307*(3–4), 487–500. https://doi.org/10.1016/j.epsl.2011.05.022

Schlische, R. W., Young, S. S., Ackermann, R. V., & Gupta, A. (1996). Geometry and scaling relations of a population of very small rift-related normal faults. *Geology*, *24*(8). https://doi.org/10.1130/0091-7613(1996)024<0683:GASROA>2.3.CO;2

Scholz, C. H. (2010). Large earthquake triggering, clustering, and the synchronization of faults. *Bulletin of the Seismological Society of America*, *100*(3), 901–909. https://doi.org/10.1785/0120090309

Scholz, C. H. (2019). The Mechanics of Earthquakes and Faulting. In *The Mechanics of Earthquakes and Faulting* (3rd ed.). Cambridge University Press. https://doi.org/10.1017/9781316681473

Siman-Tov, S., Swaed, I., Dawood, R., & Rosensaft, M. (2019). *High resolution mapping of geological hazards – Zurim Escarpment (in hebrew) , Geological Survey of Israel, Report TR-GSI/03/2019.* https://www.gov.il/he/departments/publications/reports/siman-tov-et-al-report-2019

Sneh, A. (2004). *The 1:50,000 geological map of Nahariyya sheet*.

Sneh, A. (2006). *The 1:50,000 geological map of Shefaram sheet*.

Sneh, A., Bartov, Y., Weissbrod, T., & Rosensaft, M. (1998). *Geological Map of Israel, 1:200,000. Isr. Geol. Surv. (4 sheets)*. https://www.gov.il/he/departments/general/israel-map-1-200k

Soliva, R., Benedicto, A., Schultz, R. A., Maerten, L., & Micarelli, L. (2008). Displacement and interaction of normal fault segments branched at depth: Implications for fault growth and potential earthquake rupture size. *Journal of Structural Geology*, *30*(10). https://doi.org/10.1016/j.jsg.2008.07.005

Stone, J., Allan, G. L., Fifield, L. K., Evans, J. M., & Chivas, A. R. (1994). Limestone erosion measurements with cosmogenic chlorine-36 in calcite - preliminary results from Australia. *Nuclear Inst. and Methods in Physics Research, B*, *92*(1–4), 311–316. https://doi.org/10.1016/0168-583X(94)96025-9

Stone, J. O., Allan, G. L., Fifield, L. K., & Cresswell, R. G. (1996). Cosmogenic chlorine-36 from calcium spallation. *Geochimica et Cosmochimica Acta*, *60*(4), 679–692. https://doi.org/10.1016/0016-7037(95)00429-7

Stone, J. O. H., Evans, J. M., Fifield, L. K., Allan, G. L., & Cresswell, R. G. (1998). Cosmogenic chlorine-36 production in calcite by muons. *Geochimica et Cosmochimica Acta*, *62*(3), 433–454. https://doi.org/10.1016/S0016-7037(97)00369-4

Stone, John O. (2000). Air pressure and cosmogenic isotope production. *Journal of Geophysical Research: Solid Earth*, *105*(B10). https://doi.org/10.1029/2000jb900181

Strak, V., Dominguez, S., Petit, C., Meyer, B., & Loget, N. (2011). Interaction between normal fault slip and erosion on relief evolution: Insights from experimental modelling. In *Tectonophysics* (Vol. 513, Issues 1–4). https://doi.org/10.1016/j.tecto.2011.10.005

Taylor, S. K., Bull, J. M., Lamarche, G., & Barnes, P. M. (2004). Normal fault growth and linkage in the Whakatane Graben, New Zealand, during the last 1.3 Myr. *Journal of Geophysical Research: Solid Earth*, *109*(B2). https://doi.org/10.1029/2003JB002412

Tesson, J., & Benedetti, L. (2019). Seismic history from in situ 36 Cl cosmogenic nuclide data on limestone fault scarps using Bayesian reversible jump Markov chain Monte Carlo. *Quaternary Geochronology*, *52*, 1–20. https://doi.org/10.1016/j.quageo.2019.02.004

Tesson, J., Pace, B., Benedetti, L., Visini, F., Delli Rocioli, M., Arnold, M., Aumaître, G., Bourlès, D. L., & Keddadouche, K. (2016). Seismic slip history of the Pizzalto fault (central Apennines, Italy) using in situ-

produced ^{36} Cl cosmic ray exposure dating and rare earth element concentrations. *Journal of Geophysical Research: Solid Earth*, *121*(3), 1983–2003. https://doi.org/10.1002/2015JB012565

Usami, K., Ikehara, K., Kanamatsu, T., & McHugh, C. M. (2018). Supercycle in great earthquake recurrence along the Japan Trench over the last 4000 years. *Geoscience Letters 2018 5:1*, *5*(1), 1–12. https://doi.org/10.1186/S40562-018-0110-2

Villani, F., Pucci, S., Civico, R., Martini, P. M. De, Cinti, F. R., & Pantosti, D. (2018). Surface Faulting of the 30 October 2016 Mw 6.5 Central Italy Earthquake: Detailed Analysis of a Complex Coseismic Rupture. *Tectonics*, *37*(10), 3378–3410. https://doi.org/10.1029/2018TC005175

Walsh, J., Childs, C., Imber, J., Manzocchi, T., Watterson, J., & Nell, P. A. R. (2003). Strain localisation and population changes during fault system growth within the Inner Moray Firth, northern North Sea. *Journal of Structural Geology*, *25*(2), 307–315. https://doi.org/10.1016/S0191-8141(02)00028-7

Wells, D. L., & Coppersmith, K. J. (1994). New Empirical Relationships among Magnitude , Rupture Length , Rupture Width , Rupture Area , and Surface Displacement. *Bulletin Of The Seismological Society Of America*, *84*(4), 974–1002.

Wesnousky, S. G. (2008). Displacement and geometrical characteristics of earthquake surface ruptures: Issues and implications for seismic-hazard analysis and the process of earthquake rupture. *Bulletin of the Seismological Society of America*, *98*(4). https://doi.org/10.1785/0120070111

Zohar, M., Salamon, A., & Rubin, R. (2017). Earthquake damage history in Israel and its close surrounding - evaluation of spatial and temporal patterns. *Tectonophysics*, *696–697*, 1–13. https://doi.org/10.1016/j.tecto.2016.12.015

Zreda, M., & Noller, J. S. (1998). Ages of prehistoric earthquakes revealed by cosmogenic chlorine-36 in a bedrock fault scarp at Hebgen Lake. *Science*, *282*(5391), 1097–1099. https://doi.org/10.1126/science.282.5391.1097

7.Supplementary

Contents of this Supplementary

1. Figures S1 to S9: Figures related to the ^{36}Cl modeling procedure.

2. Tables S1 to S2: Data rock files for all the samples, with whole rock chemistry for each sample.

3. Table S3: ^{36}Cl modeling parameters for modeling code.

Deir Al-Assad fault	Z (position on the scarp)	As	Ba	Be	Bi	Cd	Ce	Co	Cr	Cs	Cu	Dy	Er	Eu	Ga	Gd	Ge	Hf	Ho	In	La	Lu	Mo
sample name	cm	ppm	ppm	ppm	ppm	ppm	ppm	ppm	ppm	ppm	ppm	ppm	ppm	ppm	ppm	ppm	ppm	ppm	ppm	ppm	ppm	ppm	ppm
btf-1080	1140	0	1.975	0	0	0.047	0	0	0.552	0	0	0	0.01	0	0	0	0	0	0	0	0.019	0	0
btf-1050	1110	0	1.52	0	0	0.177	0.046	1.18	1.836	0	0.278	0	0.008	0.008	0	0.015	0	0	0	0	0.069	0	0
btf-1020	1080	0	2.584	0	0	0.115	0.066	0.716	3.094	0	1.457	0	0.018	0.008	0	0.025	0	0	0	0	0.099	0	0
btf-990	1050	0	2.03	0	0	0.158	0.063	0.621	2.504	0	1.588	0	0	0	0	0.021	0	0	0	0	0.084	0	0
btf-960	1020	0	0.405	0	0	0.135	0.029	0.8	1.802	0	1.243	0	0	0	0	0.01	0	0	0	0	0.077	0	0
btf-930	990	0	1.277	0	0	0.204	0.051	0.603	2.084	0	0.46	0	0	0	0	0.02	0	0	0	0	0.082	0	0
btf-900	960	0	2.474	0	0	0.064	0.08	0.215	2.14	0	1.313	0	0	0	0	0.016	0	0	0	0	0.135	0	0
btf-870	930	0	2.146	0	0	0.368	0.06	0.417	2.564	0	0.626	0	0	0.01	0	0	0	0	0	0	0.109	0	0
btf-840	900	0	1.449	0	0	0.036	0.098	0.24	3.875	0	3.751	0	0	0	0	0.018	0	0	0	0	0.107	0	0
btf-810	870	0	2.972	0	0	0.098	0.033	0.131	2.426	0	12.86	0	0	0	0	0.022	0	0	0	0	0.055	0	0
btf-780	840	0	1.998	0	0	0.142	0.064	0.446	1.778	0	2.919	0	0	0	0	0	0	0	0	0	0.092	0	0
btf-750	810	0	2.174	0	0	0.118	0.1	0.543	2.11	0	0.942	0	0	0	0	0.027	0	0	0	0	0.127	0	0
btf-720	780	0	2.112	0	0	0.098	0.139	0.453	2.892	0	1.018	0	0	0.014	0	0.014	0	0	0	0	0.181	0	0
btf-690	750	0	2.176	0	0	0.072	0.063	0.153	2.554	0	0.917	0	0	0	0	0.018	0	0	0	0	0.099	0	0
btf-660	720	0	3.647	0	0	0.199	0.163	0.312	1.582	0	0.631	0	0	0.007	0	0.035	0	0	0	0	0.163	0	0
btf-630	690	0	1.934	0	0	0.227	0.064	0.445	2.469	0	1.334	0	0	0	0	0.027	0	0	0	0	0.109	0	0
btf-600	660	0	4.116	0	0	0.166	0.12	0.831	2.012	0	1.938	0	0	0.009	0	0.018	0	0	0	0	0.203	0	0
btf-570	630	0	2.242	0	0	0.098	0.213	0.463	2.508	0	1.735	0	0	0	0	0.053	0	0	0	0	0.276	0	0
btf-540	600	0	2.395	0	0	0.104	0.187	1.052	3.634	0	2.447	0	0	0.01	0	0.062	0	0	0	0	0.208	0	0
btf-510	570	0	1.355	0	0	0.134	0.089	0.929	1.33	0	0.528	0	0	0.006	0	0.013	0	0	0	0	0.127	0	0
btf-480	540	0	0.973	0	0	0.06	0.181	0.439	1.945	0	0.895	0	0	0.009	0	0.017	0	0	0	0	0.146	0	0
btf-450	510	0	1.696	0	0	0.341	0.218	0.512	2.794	0	3.571	0	0	0.009	0	0.047	0	0	0	0	0.208	0	0
btf-420	480	0	1.708	0	0	0.11	0.195	0.592	2.858	0	1.556	0	0	0	0	0.051	0	0	0	0	0.144	0	0
btf-390	450	0	3.792	0	0	0.154	0.125	0.444	1.669	0	1.206	0	0	0.01	0	0.01	0	0	0	0	0.116	0	0
btf-360	420	0	4.696	0	0	0.15	0.252	0.252	2.12	0	2.086	0	0	0.014	0	0.055	0	0	0	0	0.239	0	0
btf-330	390	0	1.202	0	0	0.122	0.094	0.31	1.39	0	2.696	0	0	0	0	0.038	0	0	0	0	0.122	0	0
btf-300	360	0	4.359	0	0	0.12	0.256	0.547	1.974	0	1.145	0	0	0.009	0	0.043	0	0	0	0	0.256	0	0
btf-270	330	0	2.835	0	0	0.114	0.193	0.613	1.33	0	1.75	0	0	0	0	0.035	0	0	0	0	0.245	0	0
btf-240	300	0	3.046	0	0	0.102	0.113	0.521	1.574	0	2.548	0	0	0.011	0	0.011	0	0	0	0	0.159	0	0
btf-210	270	0	3.09	0	0	0.099	0.069	0.893	0.587	0	1.709	0	0	0.008	0	0.015	0	0	0	0	0.092	0	0
btf-180	240	0	2.996	0	0	0.191	0.124	1.212	1.317	0	1.822	0	0	0	0	0.019	0	0	0	0	0.181	0	0
btf-150	210	0	4.099	0	0	0.204	0.261	1.078	3.106	0	2.148	0	0	0.007	0	0.035	0	0	0	0	0.261	0	0
btf-120	180	0	2.574	0	0	0.145	0.125	0.858	1.369	0	1.957	0	0	0	0	0.01	0	0	0	0	0.154	0	0
btf-90	150	0	1.689	0	0	0.12	0.11	1.249	1.409	0	1.769	0	0	0	0	0.03	0	0	0	0	0.16	0	0
btf-60	120	0	0.954	0	0	0.145	0.091	1.081	1.609	0	1.79	0	0	0	0	0.018	0	0	0	0	0.1	0	0
btf-30	90	0	1.487	0	0	0.124	0.075	0.843	1.251	0	1.02	0	0	0.005	0	0.016	0	0	0	0	0.113	0	0
btf-0	60	0	1.984	0	0	0.169	0.062	1.138	1.3	0	1.761	0	0	0.008	0	0.008	0	0	0	0	0.1	0	0
btf-(-30)	30	0	0.855	0	0	0.214	0.083	0.891	1.497	0	13.84	0	0	0	0	0.024	0	0	0	0	0.083	0	0
btf-(-60)	0	0	1.393	0	0	0.054	0.185	0.109	2.874	0	4.811	0	0	0.022	0	0.011	0	0	0	0	0.109	0	0

Table S1: The major and trace element concentrations of the Deir Al-Assad fault.

Deir Al-Assad fault	Nb	Nd	Ni	Pb	Pr	Rb	Sb	Sm	Sn	Sr	Ta	Tb	Th	Tm	U	V	W	Y	Yb	Zn	Zr	SiO2 (Si)	Al2O3 (Al)	Fe2O3 (Fe)	MnO (Mn)
sample name	ppm	ppm	ppm	ppm	ppm	ppm	ppm	ppm	ppm	ppm	ppm	ppm	ppm	ppm	ppm	ppm	ppm	ppm	ppm	ppm	ppm	%	%	%	%
btf-1080	0	0.0187	5.6716	0	0	0	0	0.0094	0	87.404	0	0	0	0	0	2.1526	0	0.0281	0	3.7811	0	0	0.006013134	0.005959277	0.002790846
btf-1050	0	0.0231	12.383	0	0	0	0	0	0	83.45	0	0	0.1775	0	0	3.4256	0	0.0694	0	10.069	0	0	0.004781038	0.003430828	0.002380227
btf-1020	0	0.0658	12.788	0	0	0	0	0.0247	0	85.887	0	0	0.2057	0	0	3.2094	0	0.0987	0	12.064	0	0	0.00876494	0.003889731	0.001513814
btf-990	0	0.0421	13.497	0	0	0	0	0	0	67.346	0	0	0.2104	0	0	2.9665	0	0.1683	0	11.698	0	0	0.016109494	0.006151685	0.001481257
btf-960	0	0.0578	12.12	0	0	0	0	0	0	62.64	0	0	0.2216	0	0	3.5164	0	0.0963	0	10.231	0	0	0.016846697	0.007107488	0.002304534
btf-930	0	0.0204	12.849	0	0	0	0	0	0	68.074	0	0	0.1328	0	0	4.637	0	0.1532	0	9.3251	0	0	0.015544123	0.007447936	0.001275143
btf-900	0	0.0477	10.524	0	0	0	0	0.0239	0	65.212	0	0	0.1989	0	0	3.0466	0	0.1432	0	10.142	0	0	0.00769545	0.002483622	0.00113925
btf-870	0	0.0199	15.61	0	0	0	0	0.0298	0	62.968	0	0	0.2385	0	0	4.0839	0	0.1391	0	23.102	0	0	0.011257223	0.003755261	0.000701209
btf-840	0	0.08	9.5722	0	0	0	0	0.0089	0	78.284	0	0	0.1511	0	0	5.5549	0	0.1689	0	8.159	0	0	0.01447954	0.006924582	0.001348685
btf-810	0	0.0219	11.386	0	0	0	0	0	0	56.528	0	0	0.5136	0	0	3.169	0	0.1202	0	28.936	0	0	0.009008592	0.004754923	0.000863204
btf-780	0	0.0638	12.27	0	0	0	0	0.0142	0	55.86	0	0	0.2834	0	0	2.8408	0	0.1204	0	11.81	0	0	0.01051366	0.008639346	0.00136591
btf-750	0	0.0725	12.643	0	0	0	0	0.0091	0	62.689	0	0	0.1902	0	0	3.8218	0	0.1449	0	9.4912	0	0	0.004086822	0.003190141	0.001163756
btf-720	0	0.0906	12.518	0	0	0	0	0.0209	0	64.938	0	0	0.1812	0	0	4.1122	0	0.23	0	10.796	0	0	0.010896118	0.005226588	0.000892741
btf-690	0	0.0809	15.358	0	0	0	0	0.027	0	63.301	0	0	0.1169	0	0	1.8253	0	0.1619	0	10.107	0	0	0.013619176	0.004757856	0.000978048
btf-660	0	0.0851	12.812	0	0	0	0	0.0213	0	66.07	0	0	0.227	0	0	1.4969	0	0.2341	0	14.245	0	0	0.014712674	0.006928355	0.001543481
btf-630	0	0.0454	14.606	0	0	0	0	0.0091	0	52.741	0	0	0.2633	0	0	2.342	0	0.1634	0	22.867	0	0	0.005907959	0.002871887	0.000960866
btf-600	0	0.1108	16.779	0	0	0	0	0.0185	0	59.503	0	0	0.4522	0	0	2.1505	0	0.3323	0	16.853	0	0	0.011080141	0.003595593	0.000834388
btf-570	0	0.1601	16.928	0	0	0	0	0.0267	0	70.078	0	0	0.2046	0	0	2.0726	0	0.2758	0	13.903	0	0	0.013756132	0.005352603	0.000763678
btf-540	0	0.0937	18.255	0	0	0	0	0.0208	0	70.031	0	0	0.2812	0	0	1.6453	0	0.3749	0	18.494	0	0	0.011290403	0.003931841	0.00091451
btf-510	0	0.0954	10.021	0	0	0	0	0.0191	0	76.278	0	0	0.0827	0	0	1.1643	0	0.1463	0	9.2318	0	0	0.015598475	0.00480104	0.000933857
btf-480	0	0.0861	9.4498	0	0	0	0	0.0172	0	62.525	0	0	0.1033	0	0	1.6352	0	0.2324	0	12.187	0	0	0.032858188	0.004585667	0.00148529
btf-450	0	0.1137	12.03	0	0	0	0	0	0	49.588	0	0	0.3221	0	0	2.586	0	0.18	0	27.65	0	0	0.041483473	0.00454049	0.002950479
btf-420	0	0.1099	11.298	0	0	0	0	0.0338	0	50.74	0	0	0.1184	0	0	1.945	0	0.1691	0	20.516	0	0	0.052267366	0.004495312	0.000883932
btf-390	0	0.0675	11.184	0	0	0	0	0	0	63.996	0	0	0.1544	0	0	1.6887	0	0.1833	0	18.093	0	0	0.063051258	0.004450135	0.001884439
btf-360	0	0.1091	7.8794	0	0	0	0	0.0204	0	55.796	0	0	0.2113	0	0	0.9611	0	0.334	0	12.255	0	0	0.07383515	0.004404958	0.003833874
btf-330	0	0.0564	7.2885	0	0	0	0	0.0188	0	63.249	0	0	0.2724	0	0	2.752	0	0.1691	0	17.188	0	0	0.084619043	0.00435978	0.003792545
btf-300	0	0.2051	7.7695	0	0	0	0	0.0342	0	80.481	0	0	0.2735	0	0	3.6069	0	0.3846	0	10.214	0	0	0.014	0.004314603	0.0032416
btf-270	0	0.1488	7.5075	0	0	0	0	0.0175	0	52.001	0	0	0.35	0	0	1.015	0	0.315	0	18.463	0	0	0.001	0.004269426	0.003099263
btf-240	0	0.1246	7.3826	0	0	0	0	0.034	0	55.313	0	0	0.4869	0	0	1.2569	0	0.2038	0	17.483	0	0	0.01	0.004224248	0.002911618
btf-210	0	0.0305	7.4617	0	0	0	0	0.0153	0	50.989	0	0	0.4349	0	0	0.6409	0	0.1297	0	13.207	0	0	0.005018213	0.004179071	0.002873689
btf-180	0	0.1527	10.019	0	0	0	0	0.0191	0	72.43	0	0	0.4866	0	0	2.3091	0	0.2767	0	20.839	0	0	0.003275043	0.004133894	0.001821065
btf-150	0	0.162	9.6062	0	0	0	0	0.0211	0	70.589	0	0	0.4437	0	0	1.7607	0	0.3592	0	16.064	0	0	0.001531873	0.004088716	0.003373833
btf-120	0	0.0386	7.5102	0	0	0	0	0.0193	0	49.515	0	0	0.3181	0	0	1.9957	0	0.2314	0	13.921	0	0	0.000245542	0.004043539	0.001362579
btf-90	0	0.1099	9.8937	0	0	0	0	0.03	0	67.357	0	0	0.3198	0	0	3.4578	0	0.1799	0	32.15	0	0	0.001974036	0.003998361	0.003654463
btf-60	0	0.0545	7.7972	0	0	0	0	0	0	83.333	0	0	0.3453	0	0	3.635	0	0.209	0	11.678	0	0	0.00370253	0.003953184	0.003217718
btf-30	0	0.0268	10.444	0	0	0	0	0	0	84.249	0	0	0.2524	0	0	3.5654	0	0.145	0	20.754	0	0	0.005431024	0.003908007	0.004600059
btf-0	0	0.0308	9.9811	0	0	0	0	0	0	74.582	0	0	0.3691	0	0	3.0374	0	0.1538	0	17.709	0	0	0.007159518	0.003862829	0.005527629
btf-(-30)	0	0.0475	8.8981	0	0	0	0	0	0	78.052	0	0	0.202	0	0	3.8966	0	0.1188	0	31.874	0	0	0.008888012	0.003817652	0.006455198
btf-(-60)	0	0.1089	16.633	0	0	0	0	0	0	97.622	0	0	0.3048	0	0	1.3172	0	0.1742	0	56.322	0	0	0.010616506	0.003772475	0.007382767

Table S1 (continued)

Deir Al-Assad fault	MgO (Mg)	CaO (Ca)	Na2O(Na)	K2O(K)	TiO2(Ti)	P2O5(P)	B	Li	H2Otot (H)	Stot (S)	CO2 tot (C)	O,rock	O,water	Cl	Ca ICP	Sample Thickness	[36Cl]	[36Cl] uncertainty
sample name	%	%	%	%	%	%	ppm	ppm	%	%	%			ppm	ppm	cm	at/g.rock	at/g.rock
btf-1080	10.830752	47.3273	0.02244	0.0343	0	0	0	1.0295	0	0	40.8419136	0	0	75.431389	338728.5	4	630734.6654	27247.90551
btf-1050	19.676668	36.3739	0.02051	0.0241	0	0	0	1.65109	0	0	42.9494136	0	0	48.70844	260333.3	4	464083.8495	21426.00612
btf-1020	15.436556	42.4237	0.02349	0.0242	0	0	0	0.55135	0	0	41.1397051	0	0	37.743126	303632.8	4	494665.572	22326.81641
btf-990	17.142464	38.9393	0.02545	0.0283	0	0	0	1.84092	0	0	42.9182203	0	0	39.851662	278694.2	4	466997.8036	20709.89715
btf-960	16.1929	37.1442	0.03181	0.0242	0	0	0	0.63584	0	0	45.6629363	0	0	46.397395	265846.1	4	436855.9791	19453.46879
btf-930	19.21239	39.9887	0.0245	0.0262	0	0	0	1.06222	0	0	39.7988756	0	0	56.239243	286205.1	3	458031.6573	19652.89527
btf-900	12.442083	41.3573	0.02453	0.0179	0	0	0	0	0	0	45.2006119	0	0	22.28139	296000.1	3	431126.2391	18797.59003
btf-870	12.179316	38.3497	0.06867	0.0257	0	0	0	1.02346	0	0	48.4710302	0	0	27.232597	274474	3	400777.2451	17431.41237
btf-840	14.6474	39.4846	0.05208	0.0225	0	0	0	0.89767	0	0	44.8680027	0	0	26.605301	282596.9	4	382954.951	17112.68395
btf-810	16.28257	34.6133	0.05728	0.0231	0	0	0	0.33875	0	0	48.1041773	0	0	36.233459	247732	3	362181.8178	15651.95513
btf-780	15.276147	35.9814	0.06248	0.0137	0	0	0	0	0	0	47.7424833	0	0	27.228958	257523.8	4	376615.1659	16631.60224
btf-750	18.713058	34.8678	0.06768	0.0216	0	0	0	0.29886	0	0	45.4191532	0	0	32.552089	249553.7	4	353610.9657	18918.18666
btf-720	16.779826	37.8526	0.07288	0.0156	0	0	0	0.23	0	0	44.3675953	0	0	15.00559	270916.3	6	264184.1891	13272.17465
btf-690	17.913498	38.685	0.07808	0.021	0	0	0	0.8632	0	0	42.4014567	0	0	11.954994	276874.4	7	246787.5702	16965.16939
btf-660	12.523011	37.7513	0.08328	0.021	0	0	0	0	0	0	48.7257037	0	0	42.605914	270191.3	7	278898.6518	13247.68596
btf-630	16.813671	37.1249	0.08848	0.0244	0	0	0	0.29956	0	0	45.0614247	0	0	38.228188	265708.2	4	255903.0623	13264.40605
btf-600	19.173353	38.8047	0.09368	0.0206	0	0	0	0.90449	0	0	41.0219302	0	0	19.393827	277730.9	4	237349.9381	10657.01222
btf-570	18.249872	37.8506	0.09888	0.0217	0	0	0	0	0	0	42.8995331	0	0	5.3279953	270902.1	6	192478.3795	8603.783562
btf-540	19.828723	31.6755	0.10408	0.0243	0	0	0	0.66647	0	0	47.4958183	0	0	9.9071796	226705.8	6	169217.5687	10447.25192
btf-510	17.158458	33.6944	0.10928	0.0162	0	0	0	0	0	0	48.1471365	0	0	32.691575	241155.7	7	175597.5859	8829.886649
btf-480	19.2698	28.9578	0.11448	0.019	0	0	0	0.29262	0	0	50.7723639	0	0	28.348039	207255.4	3	161081.1657	9185.511437
btf-450	19.356483	32.7709	0.11968	0.0184	0	0	0	0.87146	0	0	46.8726553	0	0	13.036455	234545.7	5	136970.3066	7495.6615
btf-420	17.455552	36.2875	0.12488	0.0182	0	0	0	0	0	0	45.2569305	0	0	12.028762	259714.9	6	138927.0995	7122.01425
btf-390	18.146639	40.45	0.13007	0.0178	0	0	0	0	0	0	40.4033311	0	0	5.5750099	289506.6	5	151942.8895	7458.992955
btf-360	3.426609	48.3607	0.13527	0.0159	0	0	0	0.20448	0	0	47.2127305	0	0	3.9249365	346124.2	6	175066.6124	9435.030066
btf-330	19.900059	30.2445	0.14047	0.0203	0	0	0	0.27238	0	0	48.8553982	0	0	22.948278	216464.5	5	133416.8898	7087.83953
btf-300	15.794146	37.0437	0.14567	0.0197	0	0	0	1.35902	0	0	46.1621974	0	0	20.612415	265126.7	7	121639.8177	7720.805293
btf-270	13.503369	44.2767	0.15087	0.0184	0	0	0	0	0	0	41.2199076	0	0	4.3603139	316894.8	3	140010.981	7581.964636
btf-240	6.0110121	45.0906	0.15607	0.025	0	0	0	0	0	0	47.8984175	0	0	6.0077658	322719.7	4	129279.9823	7661.760161
btf-210	12.587292	44.4755	0.16127	0.0167	0	0	0	0	0	0	41.937207	0	0	2.475725	318317.5	4	119946.9488	7544.506981
btf-180	7.210354	43.2375	0.16647	0.0239	0	0	0	0	0	0	48.5521105	0	0	5.5119434	309457.2	4	102549.7647	5813.179449
btf-150	5.3848378	44.1724	0.17167	0.014	0	0	0	0	0	0	49.442747	0	0	4.8815011	316148.3	4	114306.5833	6505.025625
btf-120	17.108044	35.3286	0.17687	0.02	0	0	0	1.22439	0	0	46.5633196	0	0	10.98991	252852.1	4	93206.71196	5731.651989
btf-90	15.101925	35.7754	0.18207	0.0217	0	0	0	0.6296	0	0	48.1227151	0	0	18.589815	256049.4	4	87788.76304	5206.448243
btf-60	17.609498	31.4532	0.18727	0.0211	0	0	0	0.58161	0	0	49.9372551	0	0	47.660101	225115.4	4	95271.37131	6323.159006
btf-30	15.531478	38.599	0.19247	0.0139	0	0	0	1.00949	0	0	44.8694826	0	0	29.279723	276258.8	4	94528.88842	5958.504707
btf-0	15.94943	35.5644	0.19767	0.0158	0	0	0	0.45369	0	0	47.4861899	0	0	32.337127	254539.3	4	91503.02534	5636.977342
btf-(-30)	17.113389	34.1184	0.20287	0.026	0	0	0	0.39204	0	0	47.7681635	0	0	34.621272	244190.6	4	109617.1048	6265.041361
btf-(-60)	14.840363	40.577	0.20807	0.0218	0	0	0	0	0	0	43.5825975	0	0	9.86015	290415.7	3	87228.20279	9021.171501

Table S1 (continued)

Sajur fault	Z (position with z<0 for the buried samples)	As	Ba	Be	Bi	Cd	Ce	Co	Cr	Cs	Cu	Dy	Er	Eu	Ga	Gd	Ge	Hf	Ho	In	La	Lu	Mo	Nb
sample name	cm	ppm	ppm	ppm	ppm	ppm	ppm	ppm	ppm	ppm	ppm	ppm	ppm	ppm	ppm	ppm	ppm	ppm	ppm	ppm	ppm	ppm	ppm	ppm
sj -(-60)	-60	0.27096	36.0079	0.37132	0	0.03011	0	1.02364	2.95048	0	3.57269	0.04014	0.01004	0.02007	0	0.04014	0	0	0.01004	0	0.09032	0	0	0
sj-(-30)	-30	0.1026	27.2835	0	0	0.03157	0	1.9336	0.88393	0.00789	1.19173	0.00789	0.00789	0.02368	0	0.00789	0	0	0	0	0.05525	0	0	0
sj-0	0	0.12745	25.9725	0	0	0.04552	0.0091	0.58263	1.88444	0	25.8997	0.01821	0.01821	0.0091	0	0.02731	0	0	0.0091	0	0.15476	0	0	0
sj-30	30	0.36919	22.5962	0.35972	0	0.0568	0.13253	0.41652	3.83387	0.0284	3.70134	0.0284	0.03787	0.00947	0	0.03787	0	0	0.00947	0	0.21773	0	0	0
sj-60	60	0.45436	18.8236	0	0	0.07418	0.07418	0.85309	3.79255	0.00927	7.42745	0.00927	0.00927	0.00927	0	0.02782	0	0	0.00927	0	0.13909	0	0	0
sj-90	90	0.16039	20.5892	0	0	0.09286	0.13507	0.38832	3.2416	0.02533	4.41499	0.02533	0.02533	0.00844	0	0.02533	0	0	0.00844	0	0.15195	0	0	0
sj-120	120	0.19942	15.7788	0	0	0.04155	0.07478	0.26589	3.09926	0	1.40422	0.03324	0.03324	0.02493	0	0.03324	0	0	0.00831	0	0.19111	0	0	0
sj-150	150	0.2893	23.6476	0	0	0.01866	0.028	0.18664	2.91162	0.01866	2.77164	0.05599	0.01866	0.00933	0	0.06532	0	0	0	0	0.10265	0	0	0
sj-180	180	0.07488	15.5292	0	0	0.0468	0.14041	0.79565	2.87369	0.00936	4.54923	0.03744	0.00936	0.00936	0	0.0468	0	0	0.00936	0	0.22465	0	0	0
sj-215	215	0.15835	22.9173	0	0	0.02639	0.04399	0.24633	1.82106	0	2.75359	0.04399	0.02639	0.0088	0	0.07038	0	0	0.0088	0	0.12316	0	0	0
sj-240	240	0	42.0754	0	0	0.02925	0.039	1.91119	3.37383	0.0195	3.36408	0.039	0.00975	0.0195	0	0.039	0	0	0.00975	0	0.10726	0	0	0
sj-270	270	0.2271	31.9333	0.32318	0	0.06114	0	0.43672	1.36258	0	73.9811	0.00873	0.01747	0.00873	0	0.0262	0	0	0	0	0.08734	0	0	0
sj-300	300	0.45681	27.3906	0	0	0.03583	0.0627	0.20601	3.65446	0.00896	4.99802	0.02687	0.04479	0.00896	0	0.04479	0	0	0.00896	0	0.14331	0	0	0
sj-330	330	0	27.8784	0	0	0.47295	0.06756	0.2787	3.21772	0	2.57586	0.02534	0.01689	0.01689	0	0.04223	0	0	0.00845	0	0.19425	0	0	0
sj-360	360	0.11935	24.0297	1.12391	0	0.11935	0.28844	0.29838	3.7994	0	4.69455	0.07957	0.02984	0.01989	0	0.07957	0	0	0.01989	0	0.27849	0	0	0
sj-390	390	0	26.3295	0	0	0.01783	0.00891	0.55262	1.32806	0.02674	1.88068	0.02674	0.01783	0.00891	0	0.04457	0	0	0.00891	0	0.1337	0	0	0
sj-420	420	0.64923	25.0644	0	0	0.02951	0	0.32462	2.42971	0.00984	2.14444	0.01967	0.02951	0.01967	0	0.02951	0	0	0	0	0.08853	0	0	0
sj-450	450	0.0648	22.7256	0	0	0.02777	0.08331	0.3425	2.47159	0.03703	3.01774	0.03703	0.00926	0.01851	0	0.04628	0	0	0.00926	0	0.16662	0	0	0
sj-510	510	0.24579	29.8988	0.33357	0	0.04389	0.05267	0.41258	2.69493	0	3.27429	0.00878	0.01756	0.02633	0	0.03511	0	0	0.00878	0	0.17557	0	0	0
sj-540	540	0.40416	34.0904	0	0	0.05639	0.32897	1.94561	4.25778	0	6.32558	0.0282	0.0376	0.0376	0	0.08459	0	0	0.0094	0	0.34777	0	0	0

Table S2: The major and trace element concentrations of the Sajur fault.

Sajur fault	Nd	Ni	Pb	Pr	Rb	Sb	Sm	Sn	Sr	Ta	Tb	Th	Tm	U	V	W	Y	Yb	Zn	Zr	SiO2 (Si)	Al2O3 (Al)	Fe2O3 (Fe)	MnO (Mn)
sample name	ppm	ppm	ppm	ppm	ppm	ppm	ppm	ppm	ppm	ppm	ppm	ppm	ppm	ppm	ppm	ppm	ppm	ppm	ppm	ppm	%	%	%	%
sj -(-60)	0.100356436	43.585	0.19068	0	0.05018	0	0	0	121.642	0	0.01004	0.02007	0	0.48171	1.10392	0	0.18064	0	14.2807	0	0	0.006013134	0.005959277	0.002790846
sj-(-30)	0.063137984	51.860	0.06314	0	0.07103	0	0.00789	0	119.552	0	0	0.00789	0	0.1026	0.62349	0	0.06314	0	7.60023	0.07103	0	0.004781038	0.003430828	0.002380227
sj-0	0.172967857	4.552	0.30952	0	0.10014	0	0.06373	0	125.966	0	0.0091	0	0	0.2458	1.32912	0	0.29131	0	20.1644	0	0	0.00876494	0.003889731	0.001513814
sj-30	0.179860748	4.402	0.64371	0	0.04733	0	0.04733	0	102.237	0	0.00947	0.03787	0	0.34079	1.55248	0	0.31239	0	14.919	0	0	0.016109494	0.006151685	0.001481257
sj-60	0.148363636	7.418	0.66764	0	0.15764	0	0.05564	0	104.967	0	0	0.02782	0	0.48218	2.31818	0	0.22255	0	32.9831	0.01855	0	0.016846697	0.007107488	0.002304534
sj-90	0.211041667	3.908	0.92014	0	0.05909	0	0.02533	0	94.4623	0	0	0.01688	0	0.29546	1.79808	0	0.27013	0	28.8452	0	0	0.015544123	0.007447936	0.001275143
sj-120	0.191107377	3.232	0.11633	0	0.01662	0	0.04985	0	78.354	0	0.00831	0	0	0.29912	2.01909	0	0.29082	0	9.55537	0	0	0.00769545	0.002483622	0.00113925
sj-150	0.214638532	4.377	0.14931	0	0	0	0.04666	0	91.8373	0	0.00933	0.00933	0	0.2333	1.14785	0	0.22397	0	10.7039	0	0	0.011257223	0.003755261	0.000701209
sj-180	0.187211009	5.925	0.3089	0	0	0	0.07488	0	88.3917	0	0	0	0	0.46803	1.88147	0	0.19657	0	15.6228	0	0	0.01447954	0.006924582	0.001348685
sj-215	0.149556034	4.487	0.14076	0	0.11437	0	0.03519	0	91.8626	0	0.0088	0	0	0.26392	1.7155	0	0.21994	0	12.2812	0	0	0.009008592	0.004754923	0.000863204
sj-240	0.107260577	4.661	0.41929	0	0.039	0	0.05851	0	107.641	0	0.00975	0.00975	0	0.29253	1.22862	0	0.25353	0	56.4093	0.039	0	0.01051366	0.008639346	0.00136591
sj-270	0.078610345	4.201	16.4296	0	0.01747	0	0.0262	0	111.181	0	0	0	0	0.14849	1.03067	0	0.12228	0	34.4575	0.0262	0	0.004086822	0.003190141	0.001163756
sj-300	0.206011404	4.577	0.35828	0	0	0	0.01791	0	104.179	0	0.00896	0.02687	0	0.30454	1.20024	0	0.24184	0	11.6352	0	0	0.010896118	0.005226588	0.000892741
sj-330	0.244918182	4.983	0.48139	0	0.0929	0	0.04223	0	107.35	0	0.00845	0.00845	0	0.30404	1.3935	0	0.2787	0	12.4993	0	0	0.013619176	0.004757856	0.000978048
sj-360	0.298382353	5.978	0.31827	0	0.03978	0	0.07957	0	100.923	0	0.00995	0.02984	0	0.42768	1.97927	0	0.40779	0	21.404	0.11935	0	0.014712674	0.006928355	0.001543481
sj-390	0.222828947	4.421	0.05348	0	0.08022	0	0	0	116.174	0	0.00891	0	0	0.15152	1.15871	0	0.19609	0	9.05577	0	0	0.005907959	0.002871887	0.000960866
sj-420	0.108205825	4.958	0.09837	0	0.10821	0	0.00984	0	111.295	0	0	0	0	0.28527	1.02304	0	0.24592	0	14.7849	0.00984	0	0.011080141	0.003595593	0.000834388
sj-450	0.296220183	5.101	0.15737	0	0	0	0.05554	0	104.593	0	0	0.00926	0	0.26845	0.99974	0	0.33325	0	10.4788	0	0	0.013756132	0.005352603	0.000763678
sj-510	0.166786957	4.380	0.14045	0	0	0	0.01756	0	122.948	0	0.00878	0	0	0.35991	1.14117	0	0.27213	0	12.7373	0	0	0.015598475	0.00480104	0.000933857
sj-540	0.30077037	5.254	0.38536	0	0	0	0.0376	0	127.395	0	0.0094	0.0376	0	0.48875	1.42866	0	0.28197	0	13.7039	0.14099	0	0.032858188	0.026437829	0.00148529

Table S2 (continued)

Sajur fault	MgO (Mg)	CaO (Ca)	Na2O(Na)	K2O(K)	TiO2(Ti)	P2O5(P)	B	Li	H2Otot (H)	Stot (S)	CO2 tot (C)	O,rock	O,water	Cl	Ca ICP	Sample Thickness	36Cl	36Cl uncertainty
sample name	%	%	%	%	%	%	ppm	ppm	%	%	%			ppm	ppm	cm	at/g.rock	at/g.rock
sj -(-60)	6.702995092	45.50743	0.0224418	0.001652	0	0.000205	0	0.030107	1.476217566	0.21711	43.03378149	0	0	8.050125	338793.09	6	92531.29595	4626.564798
sj-(-30)	8.26688066	41.0199	0.0205122	0	0	9.52E-05	0	0.607703	6.440335309	0	41.21958286	0	0	9.021745	306028.16	6	98040.16781	4902.008391
sj-0	11.72648758	37.10176	0.0234899	0.002917	0	4.28E-05	0	1.365536	6.187975806	0	41.92222778	0	0	12.02744	279701.72	6	109058.3888	5812.506758
sj-30	8.888311805	42.71309	0.025453	0.003994	0	0.000593	0	0.018933	1.974879068	0.126038	43.22697015	0	0	13.1687	319783.91	7	131392.337	6569.61685
sj-60	11.66692896	40.1696	0.0318135	0.004365	0	0.000329	0	1.789636	0.545609837	0.2705	44.26486107	0	0	14.71523	295948.21	7	122622.1908	6131.109541
sj-90	7.661947506	42.24937	0.0244989	0.007654	0	0.000736	0	0	5.345439289	0.146149	41.52393174	0	0	12.23713	311034.69	6	149101.5676	8276.407127
sj-120	10.86439858	40.8031	0.0245272	0.005745	0	0.000202	0	0.332361	1.17533033	0.218086	43.88573073	0	0	26.06346	301421.43	6	183485.0019	9544.932286
sj-150	6.68744618	43.41251	0.0686693	0.003871	0	0.000719	0	1.082525	5.294631693	0.12878	41.37269393	0	0	9.831984	322086.24	6	213078.3692	10653.91846
sj-180	8.869480491	41.89942	0.0274571	0.006237	0	0.00041	0	0.018721	3.452788633	0.138326	42.56782947	0	0	15.73896	307345.77	5	208824.4928	10441.22464
sj-215	7.993359548	44.02446	0.0279632	0.005193	0	0.000383	0	1.029297	1.373258902	0.266854	43.27891466	0	0	9.617962	325059.77	6	183455.7856	9172.789279
sj-240	6.6405626	46.72282	0.0269792	0.004267	0	0.000538	0	0.380288	0.641658659	0	43.91945744	0	0	9.513618	347558.66	5	206252.7958	10312.63979
sj-270	5.958605642	46.17092	0.0322212	0.006385	0	0.000348	0	1.380048	2.052712012	0	42.74167343	0	0	9.508085	342671.45	6	227026.32	11351.316
sj-300	7.436173661	44.68849	0.029289	0.014176	0	0.000576	0	0	1.476124673	0.129586	43.19164844	0	0	9.590571	334488.01	6	228441.9265	11422.09632
sj-330	9.210717324	43.31425	0.0351878	0.009929	0	0.000511	0	1.005009	0.927469041	0.414677	44.05080488	0	0	7.603766	323485.26	4	242259.6686	12112.98343
sj-360	10.29724739	40.80466	0.0346197	0.007305	0	0.000359	0	0.407789	2.457390161	0.089688	43.26767023	0	0	11.58116	303267.82	3	267704.2779	13385.2139
sj-390	10.33809427	39.865	0.0308922	0.0077	0	0.000217	0	1.060666	3.800944058	0.355226	42.57481531	0	0	11.14517	300152.34	4	249891.4352	12494.57176
sj-420	10.21242289	39.74799	0.0380261	0.005972	0	0.000202	0	0.403313	4.243672278	0.373076	42.34576659	0	0	10.06403	296237.38	3	300706.7357	15035.33679
sj-450	9.130206645	42.71497	0.0356242	0.006361	0	0.000464	0	1.490358	1.5626516	0.021139	43.49257153	0	0	7.226143	293834.19	5	325550.3182	16277.51591
sj-510	10.08770815	39.37069	0.0435855	0.006018	0	0.000112	0	0.693483	5.256809586	0.281527	41.91348008	0	0	8.636378	315100.58	4	372925.7877	18646.28939
sj-540	10.01657799	41.15467	0.0369277	0.008945	0	0.000454	0	0.761325	2.219020759	0.245886	43.23588847	0	0	10.32452	303797.59	3	409997.8417	20499.89209

Table S2 (continued)

^{36}Cl modeling parameters

Spallation on Ca: $\Psi_{36Cl\_Ca,0}$ = 48.8 ± 3.5 at. of ^{36}Cl.g. of Ca. yr^{-1} (Stone et al., 1996)

Spallation on K: 162 ± 24 at. of ^{36}Cl. g of K. yr^{-1} (Evans et al., 1997)

Spallation on Ti: 13 ± 3 at. of ^{36}Cl. g of Ti . yr^{-1} (Fink et al., 2000)

Spallation on Fe: 1.9 ± 0.2 at. of ^{36}Cl. g of Ti. yr^{-1} (Stone, 2005)

Slow negative muons stopping rate at land surface: $\Psi_{\mu,0}$ = 190 muon.g^{-1}.yr^{-1} (Heisinger et al., 2002)

Neutron attenuation length: 208 g.cm^{-2} (e.g. Gosse and Phillips, 2001)

Neutron apparent attenuation length for a horizontal unshielded surface: 160 g.cm^{-2}

Muon apparent attenuation length for a horizontal unshielded surface: 1500 g.cm^{-2}

Geomagnetic field description: constant (Stone, 2000)

Erosion and snow cover parameters set to zero.

Uncertainties on age and slip of paleoearthquakes integrate ± 1σ uncertainty from ^{36}Cl measurements.

Tabel S3: ^{36}Cl modeling parameters for modeling code (as defined by Schlagenhauf et al., 2010).

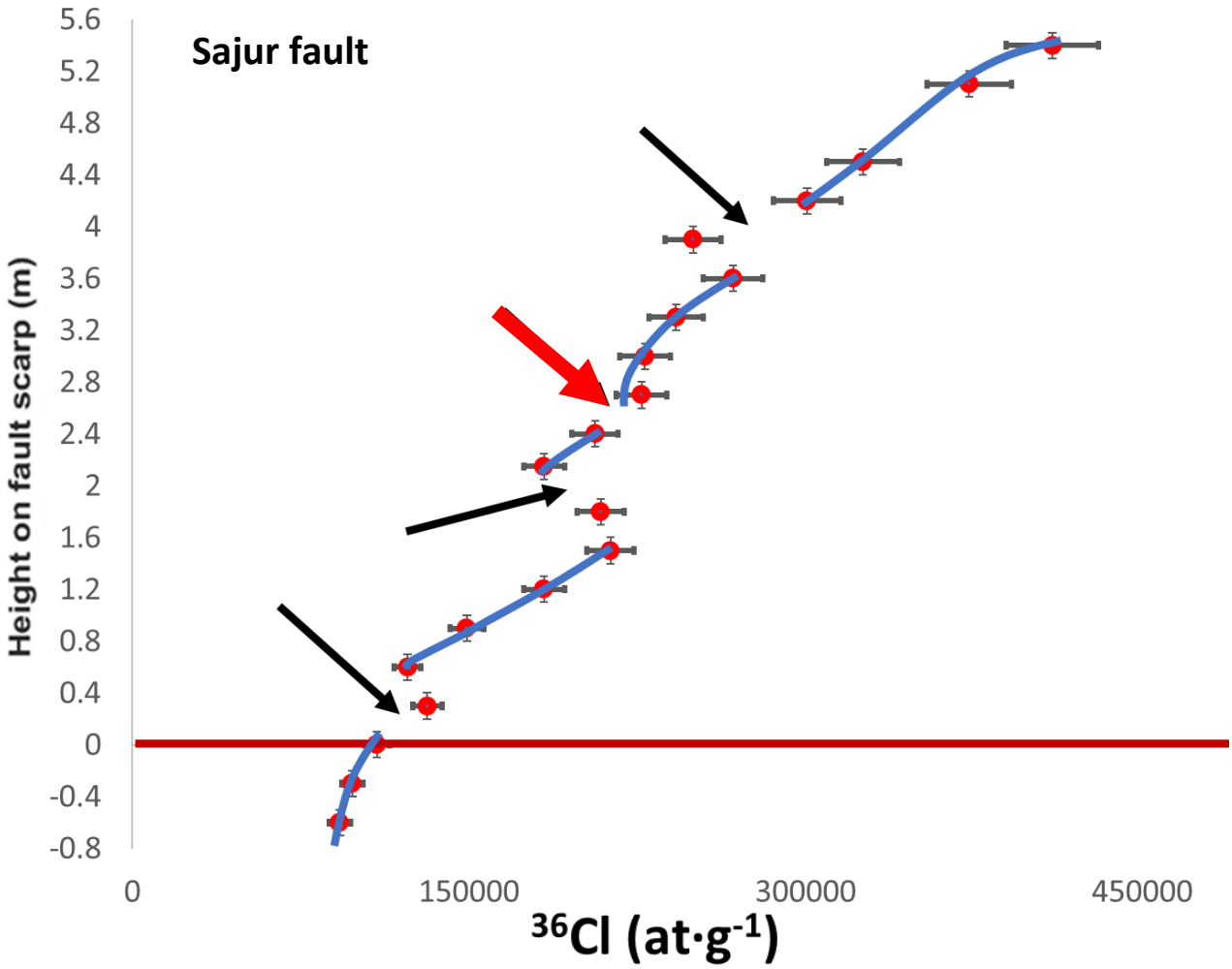

Figure S1: Discontinuity points (outlined by black and red arrows) in the ^{36}Cl profile concentration of the Sajur fault. The blue lines represent the profile shape between each discontinuity. Note that we have four discontinuity point, however, the model indicates 3 surface rupture events (see figure S2 and S3). Thus, the point outlined by the red arrow may result from the ^{36}Cl production pathways and different chemical compositions of the sample.

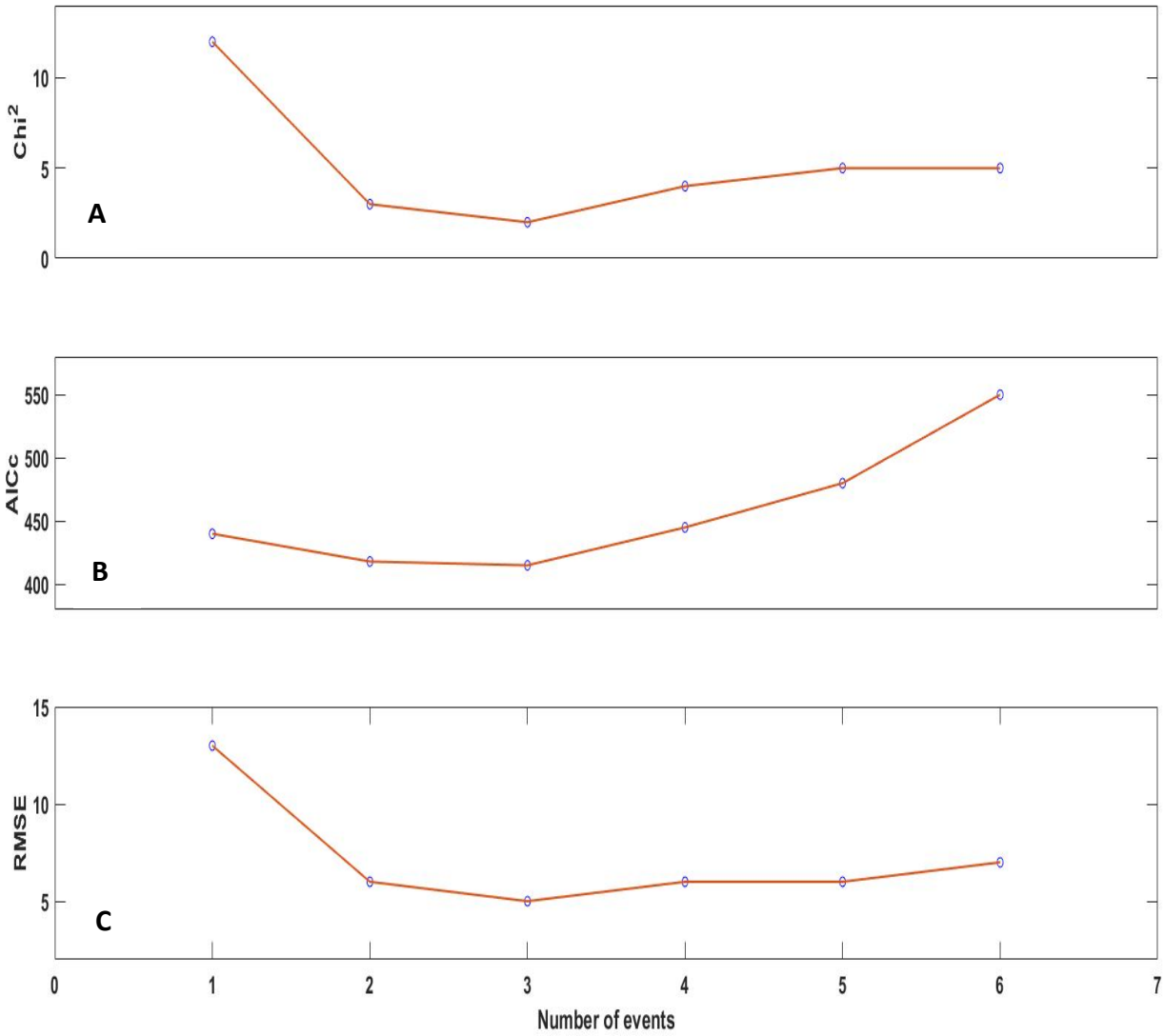

Figure S2: (A) Chi^2 (Chi-square), (B) AICc (Akaike Information Criterion), and (C) RMSE (weighted root mean square). Values obtained from fitting the Sajur fault data with the best 1–6 events scenarios. Best values are obtained for 3 earthquakes scenarios.

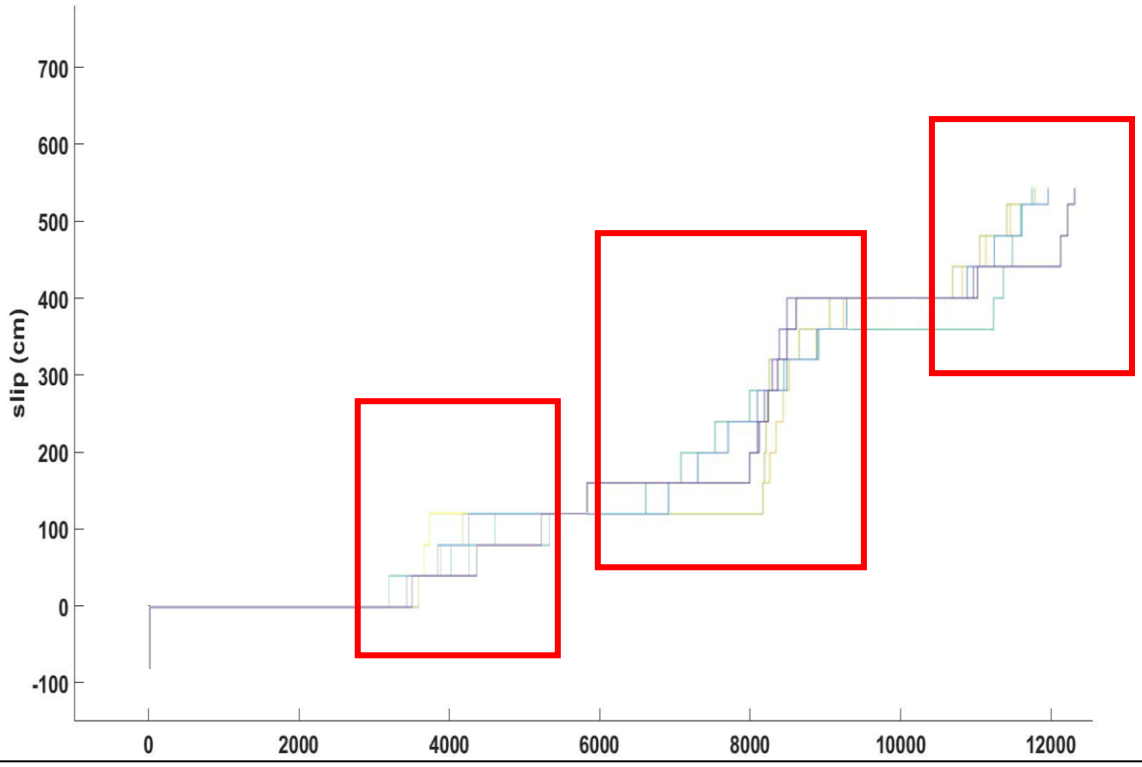

Figure S3: The Cumulative offset of the 10 best exhumation scenarios for the Sajur fault scarp. Each line represents an exhumation scenario. As can be seen, there are three distinct periods of activity (red boxes): the first period occurred during the earlier Holocene (12 ka – 11 ka), the second during the middle Holocene, and the third event occurred during the late Holocene (4 ± 1.0 ka). I used this result combined with the discontinuity points shown in figure S1 and S2 as input for the Schlagenhauf et al., (2010) model to determine the best fault scarp exhumation scenario.

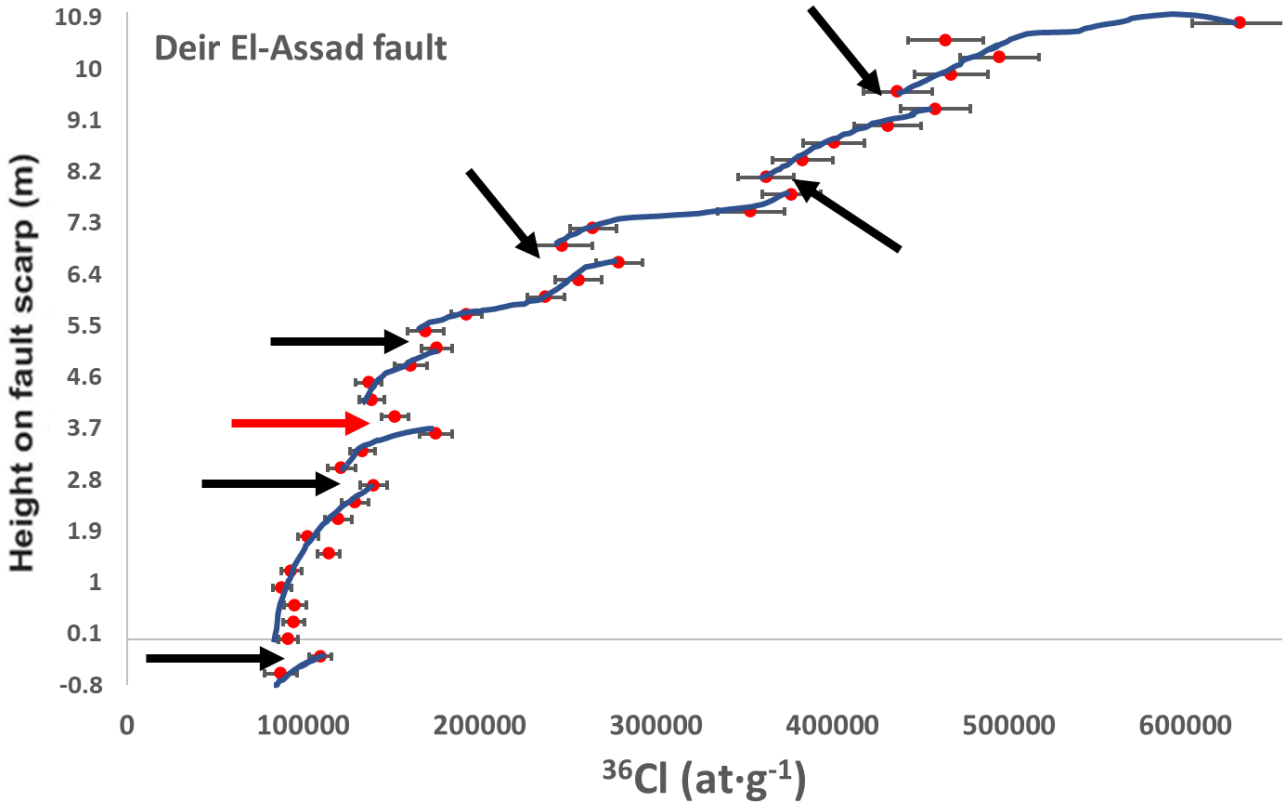

Figure S4: Discontinuity points (outlined by black and red arrows) in the ^{36}Cl profile concentration of the Deir Al-Assad fault. The blue lines represent the profile shape between each discontinuity. Note that we have seven discontinuity point, however, the model indicates 6 surface rupture events (see figure S5 and S6). Thus, the point outlined by the red arrow may result from the ^{36}Cl production pathways and different chemical compositions of the sample.

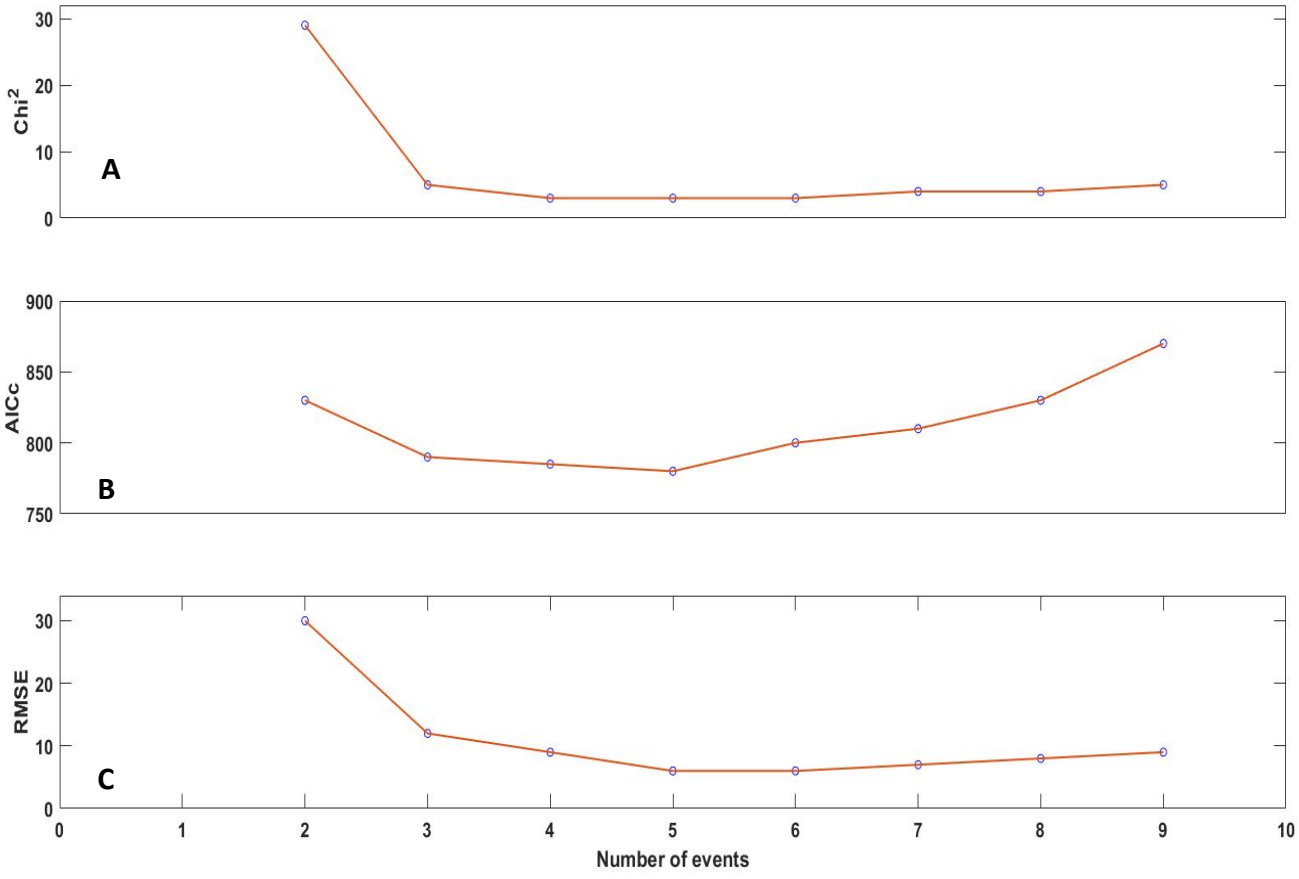

Figure S5: (A) Chi2 (Chi-square), (B) AICc (Akaike Information Criterion), and (C) RMSE (weighted root mean square). Values obtained from fitting the Deir Al-Assad fault data with the best 2–9 events scenarios. Best values are obtained for 5 earthquakes scenarios.

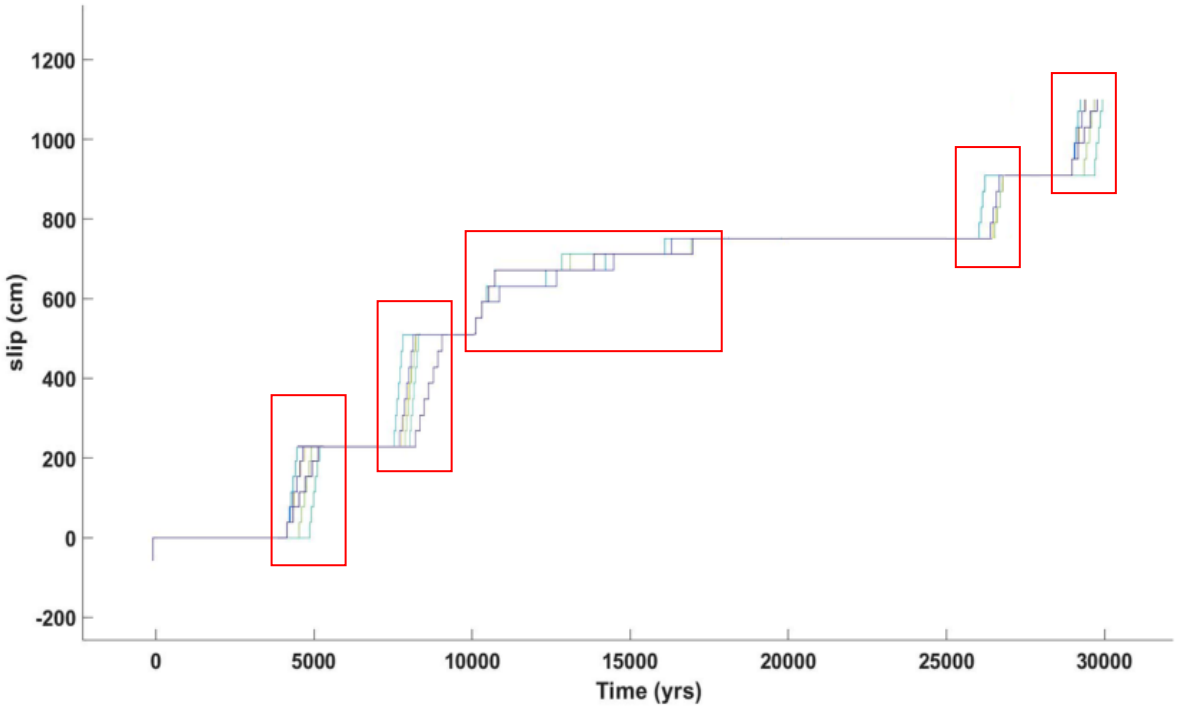

Figure S6: The Cumulative offset of the 10 best exhumation scenarios for the Deir Al-Assad fault scarp. Each line represents an exhumation scenario. As can be seen, there are five distinct periods of activity (red boxes. I used this result combined with the discontinuity points shown in figure S4 and S5 as input for the Schlagenhauf et al., (2010) model to determine the best fault scarp exhumation scenario.

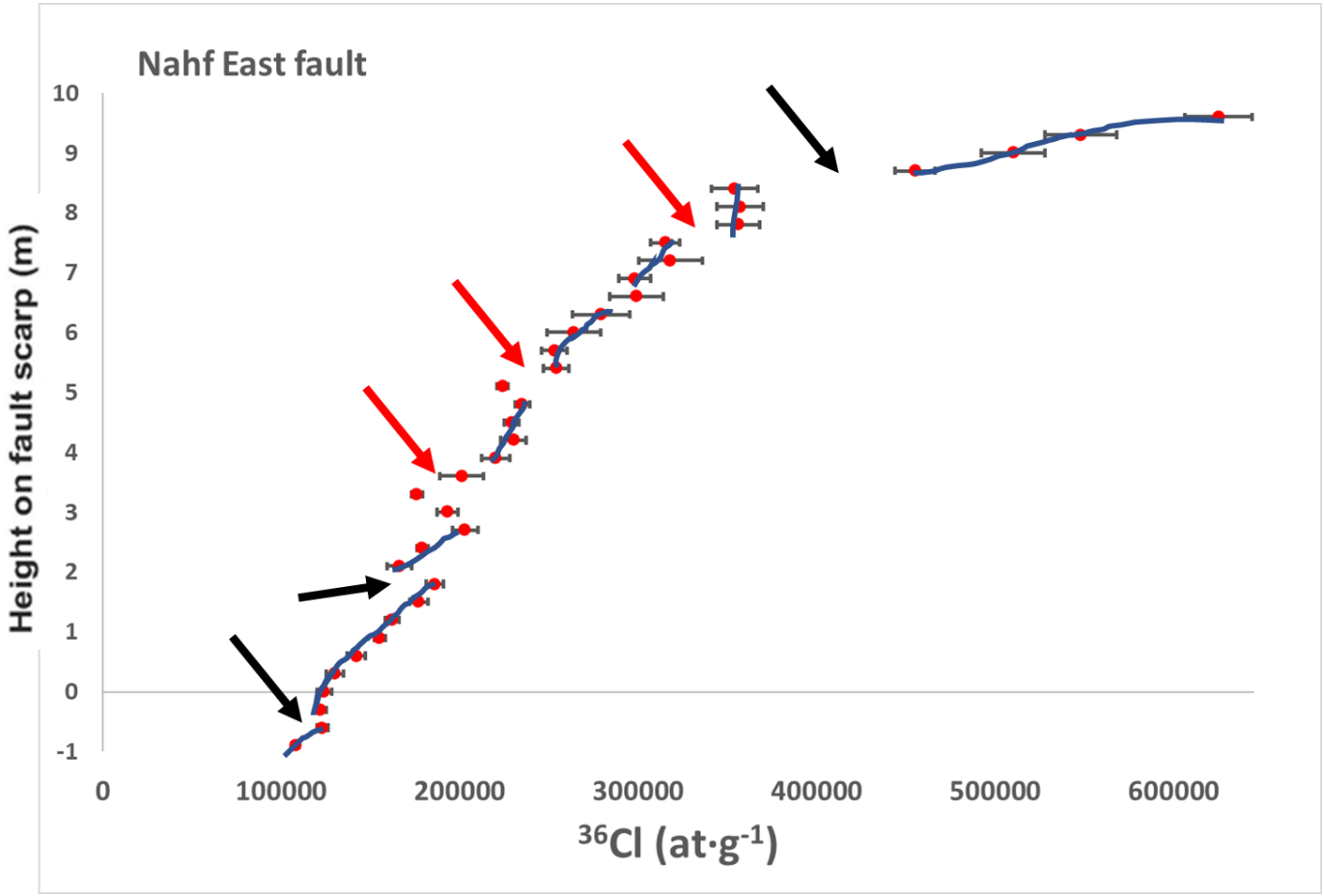

Figure S7: Discontinuity points (outlined by black and red arrows) in the ^{36}Cl profile concentration of the Nahf East fault (Mitchell et al., 2001). The blue lines represent the profile shape between each discontinuity. Note that we have six discontinuity point, however, the model indicates 3 surface rupture events (see figure S8 and S9). Thus, the point outlined by the red arrow may result from the ^{36}Cl production pathways and different chemical compositions of the sample.

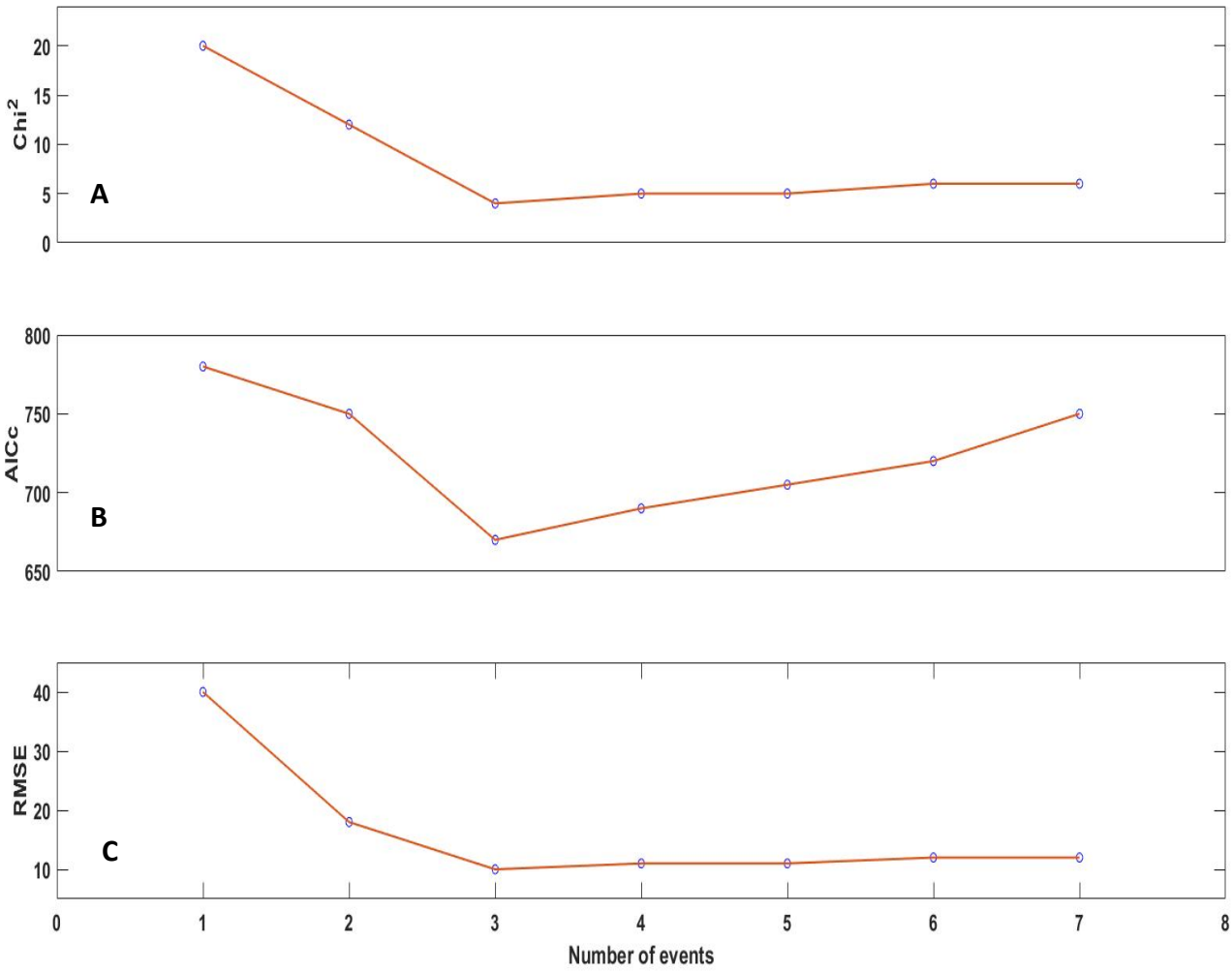

Figure S8: (A) Chi^2 (Chi-square), (B) AICc (Akaike Information Criterion), and (C) RMSE (weighted root mean square). Values obtained from fitting the Nahf East fault data with the best 1–7 events scenarios. Best values are obtained for 3 earthquakes scenarios.

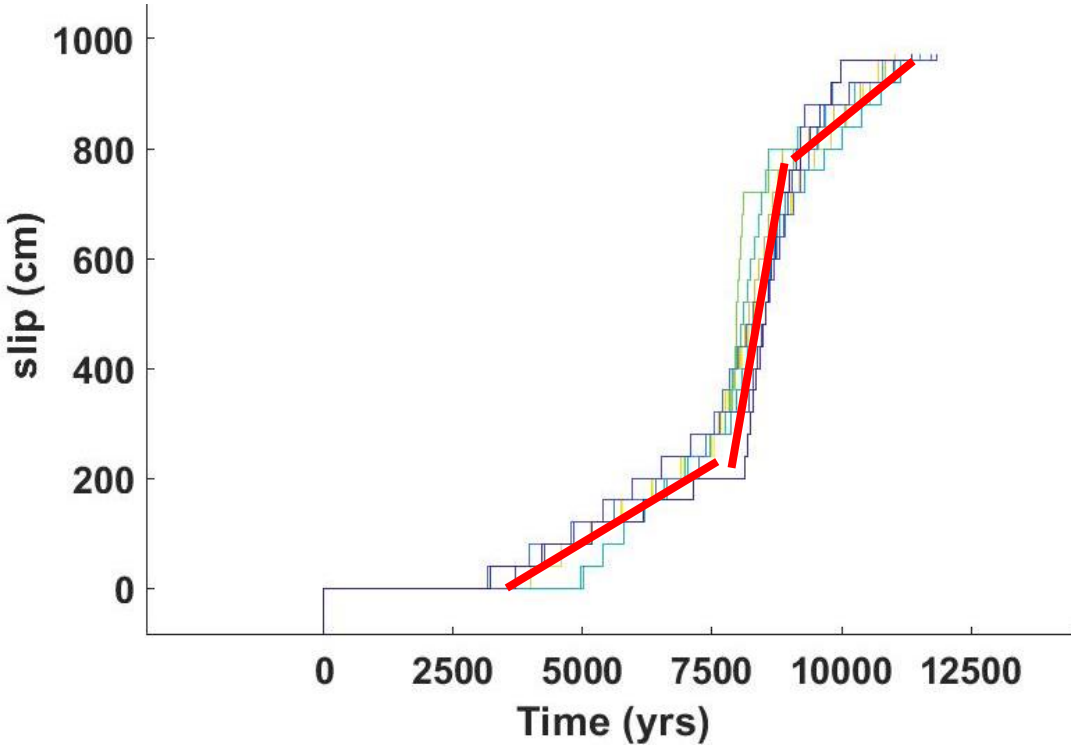

Figure S9: The Cumulative offset of the 10 best exhumation scenarios for the Nahf East fault scarp. Each line represents an exhumation scenario. As can be seen, there are three distinct periods of activity (red lines): the first period occurred during the earlier Holocene (12 ka – 9 ka), the second during the middle Holocene with over 6 meters of slip, and the third event occurred during the late Holocene (4 ± 2.0 ka). I used this result combined with the discontinuity points shown in figure S7 and S8 as input for the Schlagenhauf et al., (2010) model to determine the best fault scarp exhumation scenario.

בהן ההעתק קרע את פני השטח. התקופה העתיקה ביותר התרחשה לפני 30-28 אלף שנה לפני זמננו, והצעירה ביותר לפני 5-4 אלפים שנה, כשבכל תקופה אירעה קריעת פני שטח של לפחות 1.2 מטר. כמות הזריקה המשמעותית על ההעתקים (**>1.2 m**) שאורכם קצר באופן יחסי (קילומטרים אחדים בלבד), יחד עם הצורה האסימטרית של פרופילי צלקות ההעתקים (גובה הצלקת המקסימאלי לאורך ההעתק) והעובדה שההעתקים פעלו באותן תקופות, מציעים שצלקות ההעתק נחשפו בזמן רעידות אדמה חזקות שקרעו מספר העתקים בו זמנית. תצפיות אלו תאומות אירועי קריעת פני שטח שהתרחשו לאחרונה במערכות העתקים אחרות בעולם. כלומר, קריעת פני שטח "במערכות העתקים מקושרות" לרוב נגרמות על ידי רעידות אדמה חזקות אשר גורמות לקריעת מספר העתקים קצרים בו זמנית ולא על ידי מספר רב של רעידות אדמה בינוניות שגרמו לקריעת העתקים קצרים.

תקציר

העתקים נורמליים נוטים לעיתים להיווצר במקבצים הידועים גם בשם "מערכות העתקים". במקרים בהם ההעתקים במערכת מסודרים לאורך כיוון התארכותם (לאורך כיוון הסטרייק), עם התפתחותם הם עשויים להתחבר כך שמערכת ההעתקים עשויה להפוך להעתק אחד רציף. החיבור בין ההעתקים במערכת גורם להגברת קצב ההעתקה ולכך עשויה להיות השפעה דרמטית על התפתחות הנוף. יתר על כן, לחיבור העתקים יש ככל הנראה גם השפעה על אופיין של רעידות האדמה. מערכת ההעתקים בית כרם בצפון ישראל, הינה מערכת של העתקים מחוברים המהווה הזדמנות יוצאת דופן לבחון את השפעת התחברות ההעתקים על התפתחות הנוף ועל אופי רעידות האדמה באזור.

לצורך שחזור ההתפתחות של מערכת ההעתקים בית כרם שרטטתי עבור שישה העתקים במערכת פרופילים של כמות הזריקה הטופוגרפית, הזריקה הסטרטיגרפית ואת ההפרש ביניהן כפונקציה של המיקום לאורך ההעתק. העתק ראמה, ההעתק המזרחי ביותר שנחקר, מציג את הזריקות הטופוגרפיות והסטרטיגרפיות הגדולות ביותר במערכת, אשר הולכות וקטנות בהדרגה עבור הסגמנטים במערב המערכת. צורת הפרופילים של הזריקה לאורך ההעתקים מציעים שההעתקים הממוקמים בקרבת העתק ראמה מחוברים ישירות, חיבור המוגדר בספרות כ- "חיבור קשיח" (hard linkage), וההעתקים הממוקמים במערב המערכת מחוברים "בחיבור רך" (soft linkage). שינוי זה באופי חיבור ההעתקים מרמז על כך שמרכז המערכת בוגר ביחס לשוליו בדומה לידוע לגבי גיל התרוממות מתלול צורים שידוע כעתיק יותר כלפי מרכז מערכת ההעתקים. לאור תצפיות אלו ועל סמך הרצף הסטרטיגרפי החשוף באזור המחקר, להלן מוצעת ההיסטוריה הגיאולוגית של התפתחות מערכת ההעתקים בית כרם: בתחילה, כל הסגמנטים במערכת נוצרו בו זמנית. קצב ההעתקה וכתוצאה מכך גם קצב ההתארכות של העתקים המזרחיים במערכת היה הגבוה ביותר, כשקצבים אלו פחתו כלפי מערב. בשלב התחלתי זה, קצב ההעתקה של כל ההעתקים היה נמוך מקצב הארוזיה ולכן אף העתק לא יצר ביטוי בנוף (מדרגה טופוגרפית). כתוצאה מקצב ההתארכות הגבוה של ההעתקים המזרחים ביחס לאלו במערב המערכת, ההעתקים המזרחיים היו הראשונים להתחבר. חיבורם, גרם לקפיצה בקצב ההעתקה שלהם ולהתפתחות מתלול ראשוני לאורכם. עם הזמן החיבור בין ההעתקים נע מערבה, גרם להגברת קצב ההעתקה במערב ובכך לנדידה של התפתחות המתלול מערבה.

לרבים מבין ההעתקים במערכת בית כרם ישנן צלקות העתק אשר חשיפתן ככל הנראה נגרמה כתוצאה מתנועה על ההעתקים בעת רעידות אדמה חזקות שקרעו את פני השטח. כדי לשחזר את הגיל ועצמת רעידות האדמה שנוצרו לאורך העתקי המערכת השתמשתי בשיטת האיזוטופ הקוסמגני ^{36}Cl. באמצעות שיטה זו, שחזרתי את היסטורית החשיפה של שתי צלקות העתק, סג'ור ודיר אל-אסאד, והרצתי מחדש את מודל החשיפה של צלקת העתק נחף-מזרח, שתוארכה גם היא בעבר באמצעות שיטת האיזוטופ הקוסמגני ^{36}Cl. תוצאות המודלים של היסטורית החשיפה של צלקות ההעתקים מוכיחות ששלושת הצלקות נחשפו כתוצאה של חמש תקופות במהלך שלושים אלף השנים האחרונות

המכון הגיאולוגי
משרד האנרגיה

התפתחות בזמן ובמרחב של מערכת העתקים בית כרם

ראווי דאוד

עבודה זו הוגשה כחיבור לקבלת תואר "מוסמך" באוניברסיטה העברית בירושלים.

העבודה נעשתה בהדרכתם של:

פרופ' ארי מטמון, האוניברסיטה העברית בירושלים

ד"ר שלו סימן-טוב, המכון הגיאולוגי לישראל

דוח מס' GSI/05/2023 אפריל 2023